

**Copyright**

**by**

**Jeehyun Kim**

**2004**

**The Dissertation Committee for Jeehyun Kim Certifies that this is the  
approved version of the following dissertation:**

**Biomedical Imaging Applications of Parallel Optical  
Coherence Tomography and Adaptive Optics**

**Committee:**

---

Thomas E. Milner, Supervisor

---

H. Grady Rylander III, Supervisor

---

Massoud Motamedi

---

Digant Dave

---

Ashley J. Welch

**Biomedical Imaging Applications of Parallel Optical  
Coherence Tomography and Adaptive Optics**

by

**Jeehyun Kim, B.S., M.S.**

**Dissertation**

Presented to the Faculty of the Graduate School of

The University of Texas at Austin

in Partial Fulfillment

of the Requirements

for the Degree of

**Doctor of Philosophy**

**The University of Texas at Austin**

**December 2004**

## **Dedication**

To my beloved wife, Jeong-Yeon Kim,  
and my parents, Ki-Wan Kim, Ph.D., Yong-Book Yoon.

## Acknowledgement

There are many people who have contributed both directly and indirectly to this dissertation. Their recognition here can only be a token of the deep appreciation and the thanks that I owe.

I would like to thank Jung-Hwan Oh supporting me specially during the moment that I tried to finish my Ph.D. work. I am also grateful to all the lab mates including Eunha Kim, Sanghoon Oh, Nate Kemp, Hyun-Wook Kang, Jesung Park, Haitham Zaatari and Jihoon Kim.

I wish to thank Thomas E. Milner, Ph.D. for his insightful directions and suggestions throughout this research. Not only his expertise in engineering and science, but also his personality made me to accept him as the Sa-Boo (great master in English). In oriental society, Sa-Boo means a master who the followers like me want to become, and takes the same position as the nation and the parents. Dr. Milner is also my precious brother deeply touching my heart with Christianity.

H. Grady Rylander III, MD, Ph.D. who is the other Sa-Boo of mine, and has to take my cordial appreciation, supported and guided my dissertation research with his profound experience and knowledge in medicine and in biomedical optics.

Ki-Wan Kim, Ph.D, my father, always supported me with his useful ideas for the experimental procedure. I could never pay enough thanks for his endless love and support.

My last but deepest thanks go to my precious wife, Jeong-Yeon. She has never stopped providing rest and thoughtful advice for me to complete this dissertation. Her support has hardly been compared to anything but love.

# **Biomedical Imaging Applications of Parallel Optical Coherence Tomography and Adaptive Optics**

Publication No. \_\_\_\_\_

Jeehyun Kim, Ph.D.

The University of Texas at Austin, 2004

Supervisors: Thomas E. Milner, and H. Grady Rylander III

This dissertation presents design, implementation, and biomedical applications of parallel optical coherence tomography (OCT) and investigations to improve performance of parallel OCT by using partially spatial coherent light source and adaptive optics. A CMOS smart array detector is adapted to the parallel OCT system to improve acquisition speed and to remove any post-demodulation process. A hamster *in vivo* retina is imaged by the parallel OCT with the CMOS smart array detector. Speckle reduction in parallel OCT is demonstrated by using partially spatial coherent light source in numeric simulation and experiments. Investigation of origin of speckle is performed by imaging spatial refractive index variation with differential phase sensitive OCT. Parallel OCT with adaptive optics is designed and implemented. Improvement of lateral resolution in reflective and scattering sample is demonstrated.

## Table of Contents

List of Figures .....	xi
List of Tables .....	xix
List of Abbreviations .....	xx
List of Abbreviations .....	xx
Chapter 1 Introduction .....	1
1.1. Motivation.....	1
1.2. Dissertation Overview .....	6
Chapter 2 Real Time Retinal Imaging with Parallel OCT using CMOS Smart Array Detector.....	9
2.1. Principle of OCT .....	9
2.2. OCT Light Sources .....	11
2.3. CMOS Smart Array Detector.....	13
2.4. Experimental Setup.....	16
2.5. Sample preparation for Air Force Target.....	21
2.6. Sample preparation for <i>ex vivo</i> gold fish retina .....	21
2.7. Sample preparation for <i>in vivo</i> hamster retina .....	21
2.8. Results and Discussion .....	22
2.9. Conclusion .....	31
2.10. References.....	33

Chapter 3 OCT Speckle Reduction by a Partially Spatial Coherent Source.....	40
3.1. Abstract.....	40
3.2. Introduction.....	41
3.3. Theory and Methods .....	43
3.3.1. Numerical Simulation .....	49
3.3.2. Experimental Setup.....	50
3.4. Results.....	55
3.5. Discussion .....	61
3.6. Conclusion .....	65
3.7. References.....	67
Chapter 4 Spatial Refractive Index Measurement of Porcine Artery Using Differential Phase OCT (DP OCT) .....	72
4.1. Abstract.....	72
4.2. Introduction.....	73
4.3. DP-OCT Instrumentation and Signal Processing .....	74
4.4. Sample Preparation and Sample Arm Optics Setup .....	77
4.5. Results and Discussion .....	79
4.6. Conclusion .....	83
4.7. References.....	84
Chapter 5 Optical Coherence Tomography with Adaptive Optics .....	86



5.1. Introduction to Adaptive Optics for Human Vision .....	86
5.2. Ophthalmic Application of Time-Domain OCT:.....	90
5.3. Description of the Wavefront Correction Device .....	91
5.3.1. Structure of PAL-SLM .....	91
5.3.2. Principle of Phase Modulation of PAL-SLM .....	93
5.3.3. Write Light Optics Setup .....	94
5.3.4. Calibration of the Wavefront Correction Device (PPM) .....	95
5.4. Interferometer with Adaptive Optics .....	96
5.5. OCT with Adaptive Optics Setup .....	104
5.6. Phase-map Measurement using Parallel OCT .....	107
5.7. Wavefront Correction .....	111
5.8. Lateral Resolution Improvement in Raster Scanning OCT with Adaptive Optics .....	120
5.8.1. Experimental Setup .....	120
5.8.2. Results .....	123
5.9. Conclusion .....	132
5.10. References.....	134
Chapter 6 Future Directions and Conclusion.....	136
6.1. Summary .....	136
6.2. Future Directions .....	137

6.2.1. Parallel OCT with the CMOS Smart Array Detector .....	137
6.2.2. OCT with Adaptive Optics .....	140
6.3. Conclusion of the Dissertation.....	143
Bibliography .....	146
VITA.....	148

## List of Figures

Figure 2.1 Circuit diagram of each pixel of the CMOS smart array detector.....	14
Figure 2.2 Signal processing diagram of the CMOS smart array detector .....	14
Figure 2.3 Parallel OCT system with CMOS smart array detector. BL: broadband light source, L#: lenses, M: mirror, P: power supplier, F:function generator, A/D: analog to digital converter, BS: beam splitter.....	16
Figure 2.4 Clock diagram of CMOS smart array detector a) frame clock input (11 KHz) b) pixel clock output (5 MHz) c) demodulated analog output, S: sampling point .....	18
Figure 2.5 Real time parallel OCT acquisition program in Labview software interface .....	19
Figure 2.6 Parallel OCT analysis program in Labview .....	20
Figure 2.7 Data cube explanation: X cross-sectional image represents side view at fixed X position, and Y cross-sectional image represents top view at fixed Y position. .....	23
Figure 2.8 Air force target images of parallel OCT with the CMOS smart array detector a) <i>en face</i> view of number 3 b) Y cross section at a fixed X position. The circled area is outside of illuminating light and indicates background noise. c) X cross section at a fixed Y position .....	25

Figure 2.9 Air force target images with a wet tissue taken by parallel OCT with the CMOS smart array detector a) X cross-section view b) Y cross-section view. [Wet tissue is on right side of the target] .....	26
Figure 2.10 Gold fish retina images taken by parallel OCT with the CMOS smart array detector, a) X cross-section view, b) Y cross-section view .....	27
Figure 2.11 Gold fish retina image processed images of parallel OCT with the CMOS smart array detector (X cross-section) .....	28
Figure 2.12 Gold fish retina processed images of parallel OCT with the CMOS smart array detector (Y cross-section) .....	29
Figure 2.13 a) Cross-sectional <i>in vivo</i> hamster retinal image recorded by parallel OCT with the SMART array detector b) H&E stained hamster retinal histology image; GCL: ganglion cell layer, INL: inner nuclear layer, ONL: outer nuclear layer, OS: outer segments, R: retinal epithelium, C: choroid .....	30
Figure 3.1 Imaging Michelson interferometer with wide-field illumination .....	44
Figure 3.2 Optical setup with multimode fiber in source path of Michelson interferometer. L1 ( $f = 10$ mm), L2 ( $f = 150$ mm), and L3 ( $f = 100$ mm): lenses, BS: Beam splitter, ND: Neutral density filter .....	52
Figure 3.3 Flow diagram for incoherent demodulation. $X(t)$ : detected signal, BPF: band pass filter, Hilbert: Hilbert transform, ABS: absolute value, $A(t)$ : envelope of the detected signal .....	54

Figure 3.4 Simulated normalized fringe intensity for different spatial coherence lengths of Gaussian-Schell model source. $\sigma_g$ : coherence length of a Gaussian-Schell model source given at Eq. 3.10. Solid lines: complex fringe signal with speckle, and dotted lines: envelope of complex fringe signal without speckle. Beam spot size at target ( $\sigma_s$ ) was set at 100 $\mu\text{m}$ . ....	54
Figure 3.5 Second moment of normalized complex fringe signal vs. spatial coherence length ( $\sigma_g$ ).....	57
Figure 3.6 CCD camera images of metallic scattering surface through (a) single mode, (b) multimode source fiber. Reference path of interferometer is blocked.....	59
Figure 3.7 Cross-sectioned Parallel OCT image recoded from a scattering surface using: (a) single mode, (b) multimode source fiber. Fringe intensities are normalized and correspond to a single depth scan.....	59
Figure 3.8 Low coherence interferograms recorded from a scattering surface using: (a) single mode, (b) multimode source fiber.....	60
Figure 4.1 Schematic diagram of the DP-OCT system. LS: Broadband light source, L: lens, G: diffraction grating, M: mirror, D: photo-receiver, W: Calcite Wollaston prism, GA: galvanometer, C: Calcite prism. A splice is depicted by a rectangle between fibers and the value indicates the angle in degrees between the slow or fast axes of the two spliced PM fiber segments. ....	75
Figure 4.2 Sample path optics. C:channel, GA:Galvanometer, L:lens, G:coverglass,	

T:tissue section. Channels become decorrelated after propagation through the calcite prism pair. The phase lag between channels are determined by tissue thickness ( $\sim 5 \mu\text{m}$ ).....	78
Figure 4.3 Porcine renal artery (intima and media). a) phase retardation map. The color bar represents phase retardation in radians. b) elastin stained histology section. ....	80
Figure 4.4 Porcine renal artery (media and adventitia). a) phase retardation map. The color bar represents phase retardation in radians. b) Elastin stained histology section. ....	81
Figure 5.1 Fundus images in the fovea recorded without (a) and with (b) wavefront correction by adaptive optics. Images were recorded by Don Miller, Ph.D. at Indiana University.....	89
Figure 5.2 Structure of the PAL-SLM. PAL-SLM: parallel-aligned nematic liquid crystal spatial light modulator. The liquid crystal layer at the left side of the dielectric mirror can introduce wave aberration according to the amount of light detected from the $\alpha$ -Si:H layer. ....	92
Figure 5.3 Modulation principle (a) twisted nematic (b) parallel aligned nematic ....	93
Figure 5.4 Write light optics setup. PAL-SLM: parallel-aligned nematic liquid crystal spatial light modulator. R: reading surface of the PAL-SLM consisted of the array of liquid crystal cell. W: writing surface of the PAL-SLM consisted of the array of $\alpha$ -	

Si:H detecting cell. L6 and L7 is a pair of lenses imaging the LCD surface onto the writing surface [W]. LCD: liquid crystal display projecting the image produced by the computer. L8: collimating lens. LD: red laser diode. ....	94
Figure 5.5 Transfer function for the PPM indicating phase delay vs. incident light intensity .....	96
Figure 5.6 Separated Fourier spectra of a linear fringe pattern. Vertical axis indicates the intensity of a Fourier-transformed linear fringe pattern, $I(f_x, y)$ . Horizontal axis is the spatial frequency in the $x$ direction. $A(f_x, y)$ is DC and low frequency components of $I(f_x, y)$ , and $C(f_x, y)$ and $C^*(f_x, y)$ are side bands of $I(f_x, y)$ . $H(f_x, y)$ is a transfer function of a bandpass filter. ....	98
Figure 5.7 Michelson interferometer with PPM adaptive optic.....	99
Figure 5.8 Interferogram with linear aberration .....	99
Figure 5.9 Gray-scale phase map of a recorded interferogram of linear-tilted fringe .....	100
Figure 5.10 Phase map to compensate for Figure 5.9.....	101
Figure 5.11 Correction of linear tilt aberration using Fourier Transform Method. (a) Interferogram of linearly tilted aberration (b) compensated interferogram- the compensating phase map is applied to the left half of the field.....	102
Figure 5.12 Correction of diagonal tilt aberration using Fourier Transform Method (a) interferogram of the diagonal tilt aberration (b) compensated interferogram- the	

compensating phase map is applied to the left half of the field.....	102
Figure 5.13 Diagram of Parallel OCT system with adaptive optics. FT: optical fiber tip, L#: lenses, M#: mirrors BS: beam splitter, P: polarizer, RR: retroreflector, CA: circular aperture, PO: planar object, CCD: digital CCD camera, LD: laser diode, LCD: liquid crystal device .....	104
Figure 5.14 Phase map of cylindrical aberration showing sudden phase inversions	108
Figure 5.15 Intensity image of phase map of cylindrical aberration .....	109
Figure 5.16 Three-dimensional fringe data cube .....	110
Figure 5.17 Mapping between computer screen and the LCD of the PPM .....	111
Figure 5.18 a) Phase map of an interferogram of a reflective surface containing cylindrical aberration due to the sample optics. b) cross-sectional phase profile of the cylindrical aberration. ....	115
Figure 5.19 a) Phase map of the aberration-corrected interferogram of a reflective surface by Parallel OCT with adaptive optics. b) cross-sectional phase profile of cylindrical aberration. ....	116
Figure 5.20 a) Phase map of an interferogram of a scattering surface with cylindrical aberration. b) Cross-sectional phase profile averaged over 20 lines near the arrowed line in a). ....	117
Figure 5.21 a) Aberration corrected phase map of an interferogram of scattering surface b) cross-sectional phase profile averaged over 20 lines near the arrowed line	



in a) .....	118
Figure 5.22 Images of sample beams (a) without adaptive optics and (b) with adaptive optics .....	119
Figure 5.23 Configuration of sample stage with a metal grid.....	122
Figure 5.24 Side view of the sample stage with a metal grid covered with scattering media. Micro beads (1 $\mu\text{m}$ diameter) and milk are used as the scattering media. ....	122
Figure 5.25 OCT image of metal lines separated by 50 $\mu\text{m}$ without aberration correction. ....	124
Figure 5.26 OCT image on metal lines separated by 50 $\mu\text{m}$ with aberration correction .....	124
Figure 5.27 OCT image of metal lines through micro-bead solution without aberration correction .....	126
Figure 5.28 OCT image of metal lines through micro-bead solution with aberration correction .....	126
Figure 5.29 OCT image of metal grid through denser solution of micro-beads without aberration correction .....	128
Figure 5.30 OCT image of metal lines through denser solution of micro-beads with aberration correction .....	128
Figure 5.31 OCT image of metal lines through milk solution without AO .....	129
Figure 5.32 OCT image of metal lines through milk solution with AO .....	129

Figure 5.33 OCT image of an onion without AO .....	130
Figure 5.34 OCT image of an onion with AO .....	130
Figure 6.1 Fiber based parallel detecting OCT with CMOS smart array detector ..	140
Figure 6.2 Schematic diagram of the sample arm adaptive optics with two galvanometer scanners. Lenses are labeled L# and mirrors M#. Retinal and pupil conjugate planes are labeled r and p. FT: optical fiber tip of the sample arm. AP: Aperture, BS: beam splitter, LA: lenslet array, CCD: digital charge coupled device camera .....	142

## **List of Tables**

Table 2.1 Electrical specification of the Active Photo Detector.....	15
Table 3.1 Speckle r.m.s. variation according to spatial coherence length ( $\sigma_g$ ).....	57
Table 3.2 Noise comparison between multimode and single mode source fiber setups .....	60

## **List of Abbreviations**

A/D	Analog to Digital converter
FWHM	Full Width and Half Maximum
NA	Numerical Aperture
OCT	Optical Coherence Tomography
AO	Adaptive Optics
AO-OCT	Adaptive Optics Optical Coherence Tomography
DP-OCT	Differential Phase Optical Coherence Tomography
r.m.s.	Root Mean Square
RSOD	Rapid Scanning Optical Delay-line
PAL-SLM	Parallel-Aligned nematic Liquid crystal Spatial Light Modulator
SNR	Signal to Noise Ratio
CMOS	Complementary Metal Oxide Semiconductor
SLD	SuperLuminescent Diode

# Chapter 1 Introduction

## 1.1. Motivation

Optical Coherence Tomography (OCT) uses the short temporal coherence properties of broadband light to extract structural information from heterogeneous samples such as tissue. Two scanning methods are to generate two-/three-dimensional OCT images; single point raster scanning<sup>1-4</sup> versus parallel/wide field imaging<sup>5-8</sup>. Single pointer raster scanning systems focus a probe beam on a sample and detect back scattered light with a single element photo-detector. At least two scans (depth and lateral scans) are performed to acquire two-dimensional images. The lateral scan addresses laterally adjacent sample positions whereas the depth scan detects longitudinal depth positions of light-reflected sites in the sample. In contrast to a single point raster scanning system, parallel OCT illuminates a sample over a region and detects backscattered light with linear or two-dimensional detector array. Parallel OCT can acquire a two-dimensional image at one depth over a transverse scan. Although single point raster scanning systems can achieve video-rate acquisition, they have either limited sensitivity or a limited space-bandwidth product. For Poisson noise statistics, the variance of a random variable equals the mean, the signal to noise ratio (SNR) of a photo-detector signal should be proportional to the reciprocal square root of the number of photo-electrons<sup>9</sup>. Therefore, provided a CCD array has the same quantum efficiency as a PIN diode and there is sufficient light-power, the SNR of two-dimensional array detectors can roughly be  $\sqrt{N}$

times larger than that of a single element photo-detector where  $N$  is the number photo cells of an array detector. However, to have comparable number of photons detected per detector cell as in single point raster scanning systems, parallel OCT systems require roughly  $N$  times larger light power. Two types of parallel OCT systems have been presented: one uses synchronous illumination<sup>10</sup> and the other one uses a CMOS smart array with each pixel consisting of photo-detector and analog signal processing circuit<sup>8</sup>. In the CMOS smart array detector each pixel performs heterodyne detection in parallel thus increasing acquisition speed to video rate (30 frames/sec) and dynamic range compared to a CCD array. As scattering samples, an onion and a hair have been imaged at a sensitivity of 76 dB and at a sample beam power of 100mW using the CMOS detector<sup>6,11</sup>. The synchronous illumination technique developed by Beaurepaire et al is based on a Linik interference microscope with high-numerical-aperture objectives and has yielded potential resolutions better than 1  $\mu\text{m}$  in depth and 0.5  $\mu\text{m}$  in the transverse direction with a sensitivity of  $\sim 80$  dB at a one image per second. High-resolution OCT images of onion epithelium were obtained using an infrared LED with a centre wavelength of 840 nm, coherence length of 20  $\mu\text{m}$  and 40 mW output power.

To take advantage of a parallel detecting scheme several challenges are recognized: one is optical cross-talk between detecting pixels at samples and second is speckle noise. These two obstacles have similar origin that is spatial and temporal coherence of illuminating light. The third obstacle is acquisition and image processing speed which the CMOS smart array detector solves. In point raster scanning OCT, cross-talk is not a significant problem because a large amount of multiply scattered light is

rejected by means of confocal spatial filtering. In parallel OCT, where a substantial amount of cross-talk may occur, each detector should ideally not detect light originating from outside its conjugate volume. To avoid cross-talk, one must prevent interference occurring between adjacent pixels at the detection plane. This can be achieved by controlling the degree of spatial coherence of wide-field illumination. Such spatial coherence gating provides, for each parallel detection channel, an effect equivalent to confocal spatial filtering. Speckle is a major obstacle in measuring specific structural properties (e.g., birefringence<sup>12-14</sup>) of tissue specimens and observing structured features that approach the diffraction limit<sup>15</sup>. Although origin of speckle in OCT images is still being investigated, a common view is that the effect originates in distorted wavefronts of light returning from tissue that result in constructive and destructive features in the interferogram. Because both speckle and cross-talk are originated from spatial coherence of light, one may expect that partially spatial coherent illumination can reduce them.

My dissertation study was motivated by increasing acquisition speed with CMOS smart array detector so that a faster OCT retinal scanner might be developed. After encountering several technical limitations of the CMOS smart array detector for ophthalmic application my work was directed to investigate micro-scale refractive index variation in biological tissue by use of differential phase optical coherence tomography (DP-OCT). Knowledge of local refractive index variations in biological tissue is not only of basic importance in tissue optics but also a major factor that affects fringe signal variation and becomes an origin of speckle in point raster scanning OCT and parallel OCT. My next research topic was to develop a method to reduce speckle noise in parallel

OCT. In collaboration with Donald Miller, we recognized that multimode illumination in fundus imaging reduces speckle noise. Partially spatial coherent light yields a smaller coherence area than fully coherent light. When coherence area matches pixel size of the detector, minimum cross-talk is expected. This study examined the fundamentals of using partially spatial coherent light in OCT and correlating coherence volume and speckle reduction effect by numerical simulation. Finally experimental presentation of the speckle reduction effect has been demonstrated with use of multimode optical fiber. As the last component of my dissertation research, I adopted a parallel OCT technique into Adaptive Optics OCT (AO-OCT). In ophthalmic application of OCT, lateral resolution is limited by the optics of the anterior segment of the eye. Optical aberrations in the cornea, the iris and crystalline lens distort the point spread function on the retina. These aberrations<sup>16</sup>, in combination with the diffraction effect from the iris, limit both the spatial resolution of image patterns that can be projected on the retina and the resolution of retinal images that can be obtained with the imaging instruments. Eye-glasses and contact lenses can successfully correct low order aberrations of defocus and astigmatism, but can not correct high order aberrations, which is necessary to obtain high-resolution retinal imaging or to provide high quality vision for patients suffering from higher order aberrations. In recent years investigators in the vision sciences have applied adaptive optics to compensate for aberrations of the eye. Adaptive optics was originally developed to compensate for the atmospheric turbulence in astronomical imaging. Telescope systems that utilized adaptive optics have been successfully implemented in astronomy for decades to improve the resolution in astronomical imaging<sup>17, 18</sup>. Dreher et. al. were



first used a deformable mirror in conjunction with the human eye and successfully corrected the astigmatism in one subject's eye. Lian and Williams<sup>19</sup> showed that aberrations up to 8<sup>th</sup> order radial modes negatively impact optical quality when the eye's pupil is large. Liang, Williams and Miller<sup>19</sup> demonstrated that the optical quality of the human eye may be improved in practice by correcting most of the eye's higher order aberrations with an adaptive optics system, consisting of a wavefront sensor coupled via a feed-back loop with a 37-channel deformable mirror. All of these works have been directed to improve lateral resolution in a fundus retinal scanner. OCT in conjunction with adaptive optics needs to be developed in order to utilize coherence gating combined with improved lateral resolution. The device I utilized to correct wave-front aberrations in an OCT system was Hamamatsu high-resolution, nonpixelized, optically addressed parallel-aligned nematic liquid crystal spatial light modulator (PAL-SLM), PPM X7550 series. The other important device to implement AO-OCT is a wavefront sensor. Typically a Shack-Hartmann wavefront sensor<sup>20</sup> is used to extract a phase map from the wave aberrations. This expansive sensor consists of micro-lenslet array and CCD. The lenslet array dissects incoming light into a large number of sub-apertures, and then the CCD measures the wavefront slope across each subaperture by calculating lateral displacement of the focus spot from the zero position. Instead of using a Shack-Hartmann wavefront sensor, I used parallel OCT to produce interferograms of the wave aberrations, calculated phase maps, and correct wavefront aberration.

## 1.2. Dissertation Overview

After the introduction, Chapter 2 presents a parallel OCT system using a CMOS smart array detector. This chapter includes basic theory of optical low-coherence interferometry, descriptions of the CMOS smart array detector, experimental results of scattering surface targets including a wet tissue on an Air force target, *ex vivo* gold fish retina, and *in vivo* hamster retina. I describe the array detector's current technical limitation and give suggestions for future development.

Chapter 3 describes results of a numerical simulation and an experiment to test speckle reduction by using incident light with reduced spatial coherence. A Gaussian-Schell model for a partially spatial coherent source was used in the OCT simulation. For the experiment, partially spatial coherent source was generated by a multimode fiber in combination with a broadband light source. To illustrate speckle reduction with a partially spatial coherent source, I recorded low-coherence interferograms of a scattering surface using single mode and multimode source fibers. Interferograms recorded using a single mode source fiber are indicative of that observed using conventional OCT. Speckle noise in parallel OCT images recorded using a multimode source fiber is substantially reduced.

Chapter 4 presents a methodology to record spatial variation of refractive index of porcine renal artery using differential phase optical coherence tomography (DP-OCT). Micro spatial variations of refractive index in tissue introduce distortion in reflecting wave, which becomes an origin of speckle. DP-OCT provides a quantitative measure of thin specimen phase retardation and refractive index with phase resolution of 2 nm and

lateral resolution of 3  $\mu\text{m}$ . DP-OCT instrumentation is an all-fiber, dual channel Michelson interferometer constructed using polarization maintaining fiber. Two orthogonal polarization modes of light are spatially separated using a Wollaston prism and directed into separate photo-receivers. Because phase noise in the environment is equally present in both channels, computation of phase difference between the two signal channels is attributed exclusively to variation in the specimen's composite refractive index. Porcine renal artery is freshly harvested from a local abattoir. The lumen is cut open and sliced at 5  $\mu\text{m}$  thickness. Microscopic slide for the tissue section is processed by standard histology method with mounting media. Two-dimensional *en face* dual-channel phase images are taken over a  $150\text{ }\mu\text{m} \times 200\text{ }\mu\text{m}$  region on the microscopic slide and the images are reconstructed by plotting relative phase variation as the OCT beam is moved across the artery cross section. Spatial variation of refractive index in tissue gives not only different local reflectance but also phase variation of probing light. Chapter 3 illustrates the investigation of the fact that over spatially coherent area the randomized phase variation becomes an origin of speckle.

Chapter 5 presents an AO-OCT system using parallel OCT setup to extract a phase map of aberration wavefront. This chapter includes introduction to adaptive optics, description of the Hamamatsu high-resolution, non pixelized, optically addressed parallel-aligned nematic liquid crystal spatial light modulator (PAL-SLM), PPM X7550 series. It also describes the method to calculate a two-dimensional phase map from an interferogram recorded by the parallel OCT. Example results of a two-dimensional phase extraction from interferogram are provided with a detailed description of AO-OCT

system. This method is applied to correct an arbitrary aberration of sample optics. Lateral resolution improvement using the AO-OCT system is presented indicating aberration correction.

Chapter 6 presents a summary, future directions and conclusion of the dissertation. Parallel OCT systems can provide a number of advantages over point raster scanning systems. First, acquisition speed of a parallel OCT system can be very fast by using CMOS smart array detector. CMOS smart array detectors need to be improved to be more user friendly and to increase number of detector pixels. The most significant design issue that needs to be addressed is the limited dynamic range which is currently 8 bits. A second condition is speckle and cross-talk reduction which appear to be a fundamental limitation of parallel type approach, but can be minimized by adopting partially spatial coherent light sources. A third condition is improving lateral resolution. AO-OCT can improve lateral resolution to the diffraction limit by correcting wave aberrations produced by any imperfections of imaging optics.

## Chapter 2 Real Time Retinal Imaging with Parallel OCT using CMOS Smart Array Detector

### 2.1. Principle of OCT

OCT is a recent imaging technology that produces high-resolution cross-sectional images of biological tissues<sup>57</sup>. OCT is analogous to ultrasound, measuring the intensity of backscattered infrared light rather than sound waves. In studies carried out to date, the deepest penetration has been achieved using sources that emit at wavelengths between 1200 and 1800 nm. Time gating is employed so that the time for the light to be backscattered, or echo delay time, is used to assess the intensity of back reflection as a function of depth. Unlike ultrasound, the echo delay time cannot be measured electronically due to the high speed associated with the propagation of light. Therefore, a Michelson interferometer is used to perform low coherence interferometry.

The light intensity that impinges on the photo-receiver is

$$I_d = \langle |E_d|^2 \rangle = r_r I_r + r_s I_s + \text{Re} \left\{ \langle E_r^*(t + \tau) E_s(t) \rangle \right\} \quad (2.1)$$

where  $I_r$  and  $I_s$  are the mean(dc) intensities returning from the reference and sample arms of the interferometer, and  $r_r$  and  $r_s$  are reflectance of reference and sample, respectively. The second term in this equation, which depends on the optical time delay  $\tau$  set by the position of the reference mirror, represents the amplitude of the interference fringes that carry information about the tissue structure. The nature of the interference fringes

depends on the degree to which the temporal and spatial characteristics of  $E_s$  and  $E_r$  match.

The correlation amplitude depends on the temporal-coherence characteristics of the source, according to

$$\text{Re}\left\langle E_r^*(t+\tau)E_s'(t) \right\rangle = |G(\tau)| \cos(2\pi\nu_0\tau + \phi(\tau)) \quad (2.2)$$

where  $c$  is the speed of light,  $\nu_0 = c/\lambda_0$  is the center frequency of the source, and  $G(\tau)$  is the complex temporal-coherence function with argument  $\phi(\tau)$ . According to the Wiener-Khinchin theorem,  $G(\tau)$  is related to the power spectral density of the source,  $S(\nu)$ ,

$$G(\tau) = \int_0^\infty S(\nu) \exp(-j2\pi\tau\nu) d\nu \quad (2.3)$$

It follows from this relationship that the shape and width of the emission spectrum of the light source are important variables in OCT because of their influence on the sensitivity of the interferometer to the optical path difference. Sources with broad spectra are desirable because they produce interference patterns of short temporal (and spatial) extent.

If the source has a Gaussian spectrum with a full-width at half-maximum (FWHM) bandwidth,  $\Delta\lambda$ , and  $\lambda_0$ , then the coherence length ( $\Delta l$ ) or axial resolution is

$$\Delta l = (2\ln(2)/\pi) (\lambda_0^2 / \Delta\lambda) \quad (2.4)$$

The lateral or transverse resolution achieved with an OCT imaging system is determined by the focused spot size. The transverse resolution is

$$\Delta x = (4\lambda / \pi) (f / d) \quad (2.5)$$

where  $d$  is the spot size on the objective lens and  $f$  is its focal length.

## 2.2. OCT Light Sources

A proper selection of the light source is dependent on the characteristics of a target sample due to the light absorption and scattering of the sample. However, there are some general requirements for OCT imaging: 1) emission in the near infrared; 2) short temporal coherence length; and 3) high irradiance<sup>1</sup>. Emission in the near infrared is necessary because the light penetration depth through a biological tissue at wavelength in the blue and ultraviolet is very short; moreover, water absorption at wavelengths greater than 2500 nm limits the penetration depth. Up to now, investigators achieved the deepest penetration depth using wavelengths between 1200 and 1800 nm<sup>22</sup>, but the coherence length of the source is proportional to  $\lambda^2$ . The second requirement, short temporal coherence length, is based on the relationship between the temporal coherence function of the light source and the axial point spread function. Usually, light sources with wider spectral bandwidth, the better the resolution can be achieved. The third requirement, high irradiance, is based on the weak backreflection of a biological tissue especially when the scan depth is getting deeper. As the light power is increased, the system can get more backscattered light so that better images can be produced.

The most commonly used sources are edge-emitting light-emitting diodes (ELED) and superluminescent diodes (SLD). They have high irradiance and relatively low cost which make them useful in OCT imaging. ELED's center wavelengths are 1300 or 1550 nm and the spectral bandwidth is between 50 to 100 nm. Emission power is usually 20 to

300  $\mu$ W. A superluminescent diode has a range of 800 to 1300 nm center wavelength, 20 to 70 of spectral bandwidth, and one to ten mW of emission power.

Mode-locked Ti:Al<sub>2</sub>O<sub>3</sub> laser is adequate in acquiring OCT images for fast, high-resolution because it has not only very width bandwidth, 50-145 nm, that enables to achieve high resolution, but also very high power, 400 mW. However, its big size and need of another pump laser for itself are disadvantages in clinical applications.



### 2.3. CMOS Smart Array Detector

Despite improvements in scanning speed and resolution, most conventional OCT systems use a single detector. Therefore, to acquire a two-dimensional cross section image, two beam scanners are required; longitudinal and depth scanning. Several attempts to remove these moving scanners have been tried. Zeylikovich *et al.* applied a grating and CCD camera to acquire a two-dimensional image without any moving scanner<sup>23</sup>. Dresel *et al.* used a piezoelectric transducer to modulate the light and made a wide beam diameter to project the target surface<sup>24</sup>. Both cases used a CCD camera as a detector, but the CCD camera has narrow dynamic range. High DC power of the light makes saturation in CCD pixels; whereas, the small portion of AC signals that carries the tissue cross-sectioned information is contained. Moreover, because a CCD camera does not have any signal processing function, additional demodulation and filtering are necessary. These post processes delay the image acquisition time.

S. Bourquin *et al.* has developed a CMOS smart array detector<sup>8</sup>. CMOS based photocells enable detection of a small AC signal biased on high DC light. The detector array consists of  $58 \times 58$  CMOS photodiode pixels. Each pixel contains a photodiode, a band-pass filter centered at fringe frequency, an amplifier, a rectifier, and a low-pass filter. The circuit diagram of each pixel is shown at Figure 2.1.

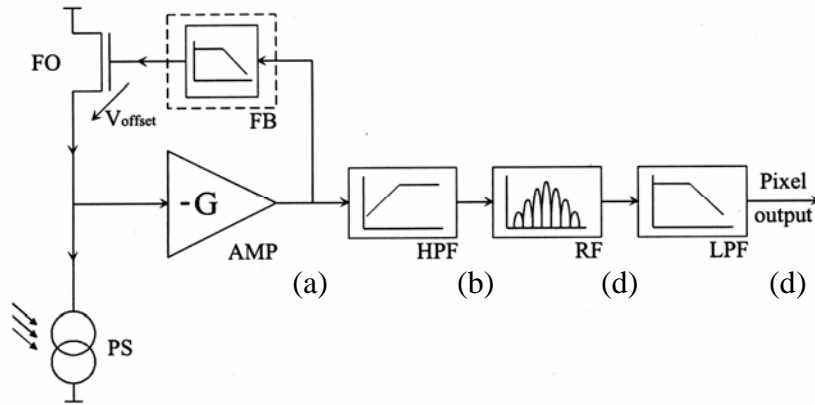


Figure 2.1 Circuit diagram of each pixel of the CMOS smart array detector

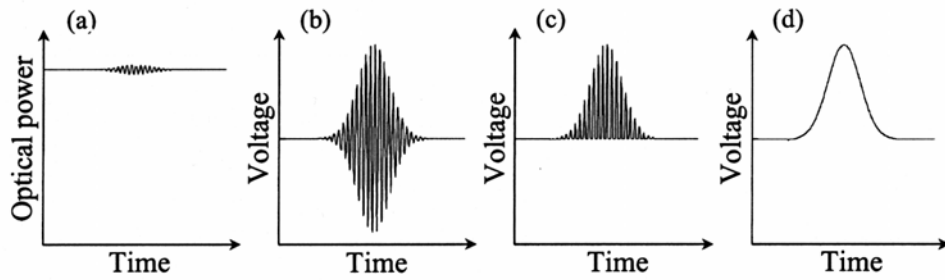


Figure 2.2 Signal processing diagram of the CMOS smart array detector

A photodiode at each pixel converts the incoming light into an electrical signal shown at Figure 2.2(a), a band-pass filter removes low, high frequency noise (Figure 2.2(b)). The output of the band-pass filter contains the information of the target tissue in the form of modulated signal. A rectifier removes negative signed signal and rectifies to

positive values (Figure 2.2 (c)). Finally low pass filtering finds envelop of the interference signal that is modulated by a fringe frequency (Figure 2.2(d)). The electronically generated envelopes are then fed into the column buffers. These buffers were selected sequentially by an address decoder, and then a 12-bit analog-digital converter digitizes the analog output signal that is then transferred to the monitoring computer. The size of this array is  $6.4 \text{ mm} \times 6.4 \text{ mm}$ , and even though a pixel area is  $110 \text{ }\mu\text{m} \times 110 \text{ }\mu\text{m}$ , the sensitive area at each pixel is only  $35 \text{ }\mu\text{m} \times 35 \text{ }\mu\text{m}$ . Consequently, the insensitive area “wastes” 90% of incoming photons.

Voltage Supply	5 V
Power dissipation	300 mW
Optical input frequency range	10 kHz ~ 500 kHz
Maximum dynamic range	60 dB
Voltage output swing	0.8V
Max. pixel data read-out rate	5 Mega pixel/s

**Table 2.1 Electrical specification of the CMOS smart array detector**

## 2.4. Experimental Setup

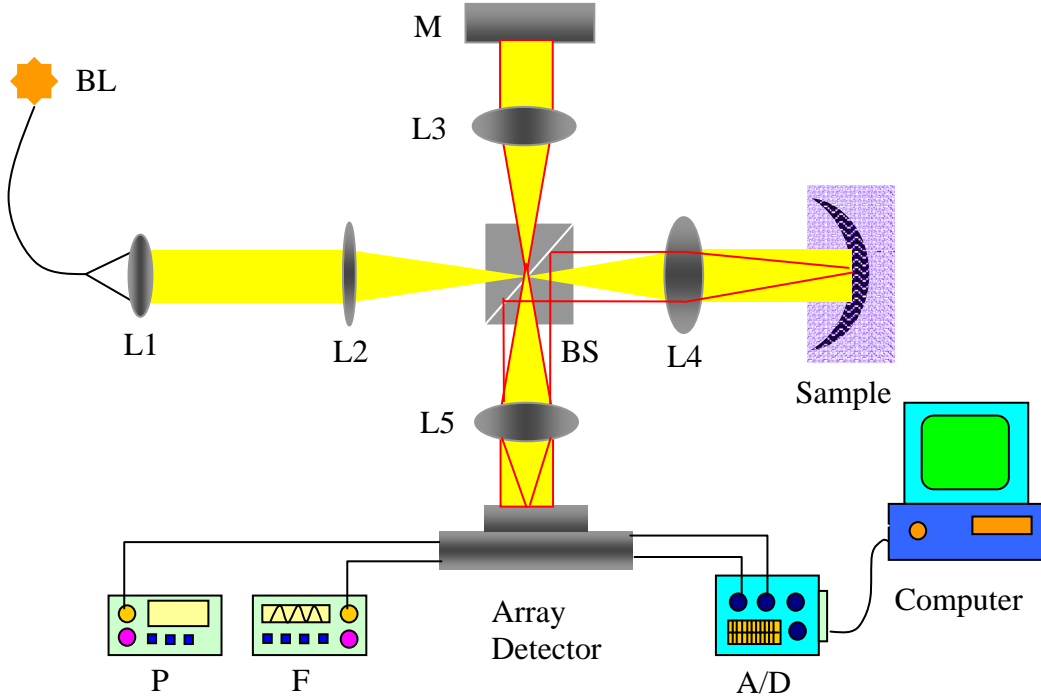


Figure 2.3 Parallel OCT system with CMOS smart array detector. BL: broadband light source, L#: lenses, M: mirror, P: power supplier, F: function generator, A/D: analog to digital converter, BS: beam splitter.

A parallel OCT system is implemented as shown at Figure 2.3 using the CMOS smart array detector. A broadband light source was coupled into a single mode optical fiber to deliver light into the parallel OCT system. The source provided 10mW of output power, a center wavelength  $\lambda_c = 670$  nm. Coherence length of the source was about  $\Delta l = 15$   $\mu$ m. Light launched into the system through a collimating lens [L1]. Through a pair of relay lenses [L2, L4] in the sample path, the beam size at the sample was reduced to 300

$\mu\text{m}$ . The sample surface was placed at the conjugate plane of the CMOS smart array detector plane. Even though actual reflectors at the sample plane are numerous, the resolution of the system is limited by the number array detector pixels. If the illuminated area was  $300\ \mu\text{m} * 300\ \mu\text{m}$ , and number of detector pixels was 58 by 58, then the resolution at the sample was about  $5\ \mu\text{m} * 5\ \mu\text{m}$ . The detector should be placed at a plane such that all the light emitted from a cell sized  $5\ \mu\text{m}$  by  $5\ \mu\text{m}$  at the sample can be integrated at a corresponding pixel of the detector. Otherwise detected image will appear blurred. In order to achieve this imaging setup the sample was placed at the focal plane of the lens [L4], and the separation between L4 and L5 was sum of both focal lengths. Beam spot size at the detector was set to be 3.3 mm. The last condition to maintain imaging the sample plane onto the detector plane was to place the detector at the focal plane of L5. However, the reference mirror was not necessarily to be imaged onto the detector, the reference beam needed to be collimated and the same size as the sample beam on the detector. The detector needed a frame clock input (Figure 2.4(a)) and outputs a read-out clock signal (Figure 2.4(b)) and demodulated analog signal (Figure 2.4(c)). The frame clock was supplied by a function generator to the array detector, and the clock rate was 1.1 KHz. Internal clock rate was set to be 5 MHz. A 12 bits Analog to digital (A/D) converter [National instrument PCI 6110E] acquired the demodulated analog signal synchronized with the falling edge of the read-out clock signal. The A/D converter was set to acquire 250 frames per depth scan, so the acquisition time was 166 ms at a 3Hz of depth scan rate. The depth scanning range was 2 mm and the resultant depth resolution at

this frame rate was 4.7  $\mu\text{m}$  which was much finer than the axial coherence length (15  $\mu\text{m}$ ).

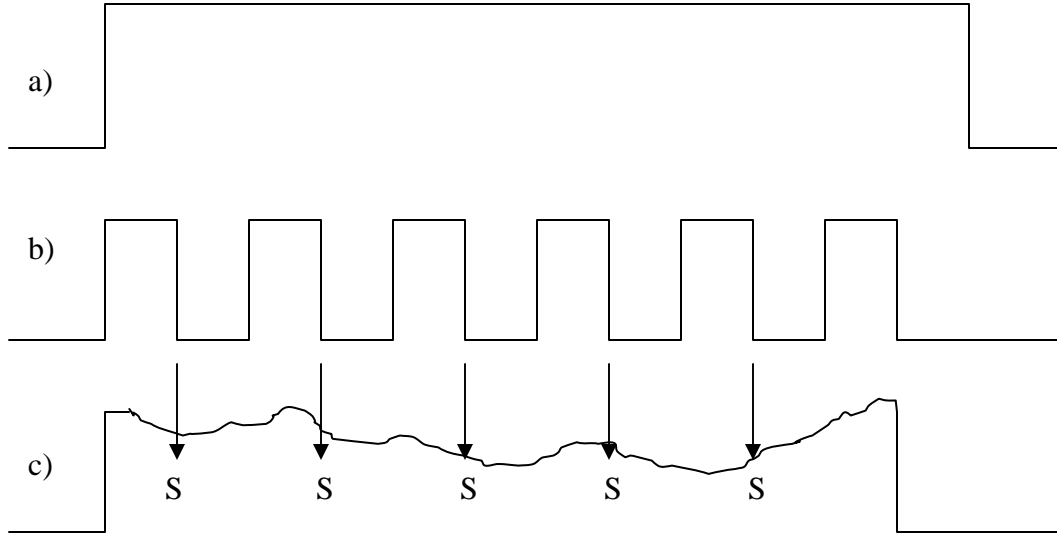


Figure 2.4 Clock diagram of CMOS smart array detector a) frame clock input (11 KHz)  
 b) pixel clock output (5 MHz) c) demodulated analog output, S: sampling point

Labview programs were developed to acquire and display the output images of the CMOS array detector shown at Figure 2.5 and Figure 2.6. A real time parallel OCT acquisition program (Figure 2.5) accepted number of columns, rows, and frames as inputs, and acquire images according to clock rate. The acquisition program displays acquired images of *en face* view and cross-section view through either X or Y directions. A parallel OCT analysis program (Figure 2.6) allows user to browse *en face* views of any frame or cross section in either X or Y directions.

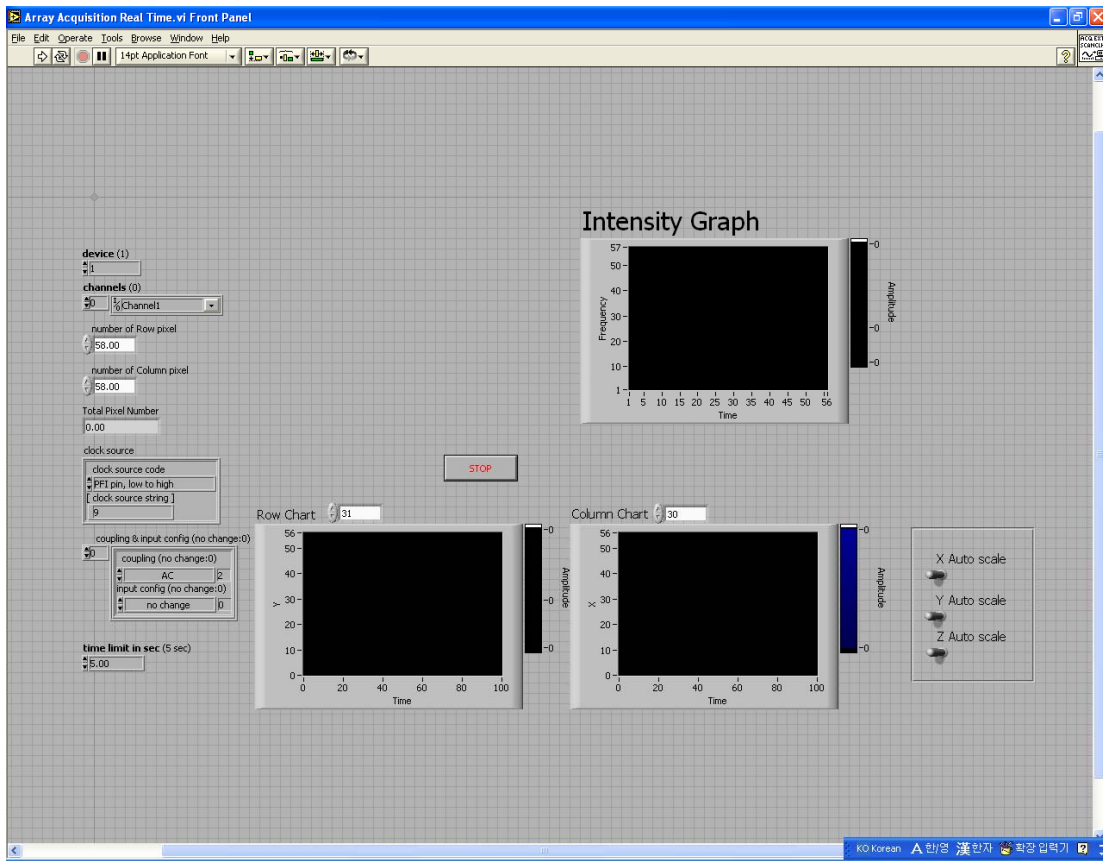


Figure 2.5 Real time parallel OCT acquisition program in Labview software interface.

Detailed description about this program is in Appendix A.



Figure 2.6 Parallel OCT analysis program in Labview. Detailed description about this program is in Appendix A.



## **2.5. Sample preparation for Air Force Target**

Two different samples have been imaged; first is the Air Force target which has reflective surface. Numeral 3 with resolution of 5.04 lines per millimeter has been imaged with 300  $\mu\text{m}$  by 300  $\mu\text{m}$  area illumination. Second target was the Air Force target (numeral 3) covered with a wet tissue that presents a scattering media, so this sample resembles real biological sample.

## **2.6. Sample preparation for *ex vivo* gold fish retina**

Third target was an *ex vivo* gold fish retina. A gold fish purchased at a local pet store, was sacrificed immediately prior to measurement. The crystalline lens and cornea were excised and the retina was immersed in a saline solution. This experiment was performed at Indiana University by the author in corporation with Dr. Donald Miller.

## **2.7. Sample preparation for *in vivo* hamster retina**

A male hamster weighing 53g was anesthetized by administrating urethane (1000 mg/kg, i.p.) and etomidate (25 mg/kg, i.p.). The hamster was placed on a plat form in the sample path, and the eye was exposed to probing light. A CCD camera was used to confirm imaging of the retinal layer onto the CMOS smart array detector plane. After confirming the image formation of the retinal layer on the CCD camera, the detection layer of the CCD camera was marked and the CMOS smart array detector was positioned at the detection layer.

Laser source was replaced with a mode-locked Ti:Sapphire laser allowing 26 mW of optical power in the sample path. Center wavelength of the laser was about 850 nm and axial coherence length was about 7  $\mu\text{m}$ . The calculated beam spot at the retina was about 10  $\mu\text{m}$ . The beam spot at the detector was 3 mm.

## **2.8. Results and Discussion**

A mirror was placed in the sample path to find coherent gated position where path length difference between the sample and reference path was less than the coherence length of the system. After finding the interfering axial position, potentiometers on the array detector required recalibration because the different incident optical power changed the balance of analog circuits in each pixel adjusted with previous light power. 250 frames of demodulated interference fringe images were recorded. Figure 2.7 illustrates different axes definitions. The X cross-section indicates an image looking from the side view whereas a Y cross-cut is a top view.

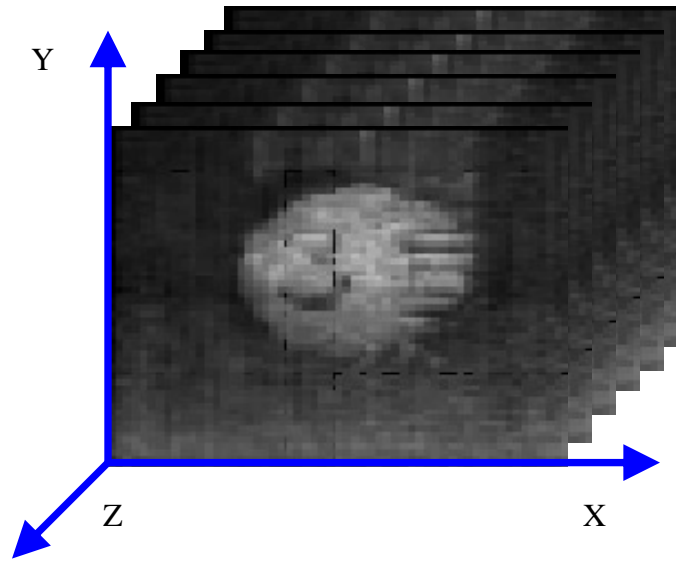
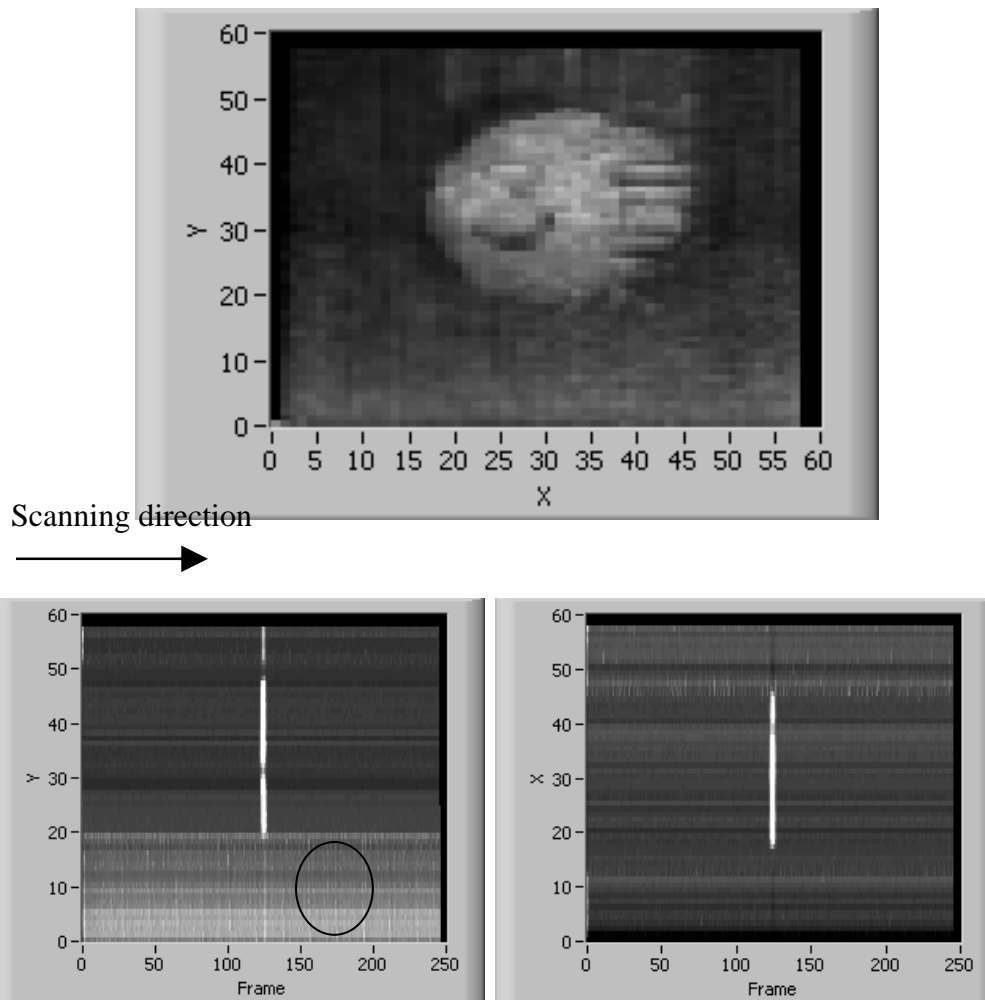


Figure 2.7 Data cube explanation: X cross-sectional image represents side view at fixed X position, and Y cross-sectional image represents top view at fixed Y position.

The second object imaged was a reflective Air Force target. The reason to choose the Air Force target was to confirm that the sample plane was imaged onto the detector plane. Figure 2.8 (a) shows an *en face* view of a demodulated interference fringe image taken by parallel OCT with the CMOS smart array detector. A number three is visible in the image. Figure 2.8 (b) and (c) display X and Y cross-sectional images of the Air force target. A wet tissue was placed on top of the Air force target to simulate scattering media. Figure 2.9 (a) and (b) show X and Y cross-sectional images of the wet tissue with the target and the wet tissue area is visible at right side of bright line. Scanning direction was from left to right. Figure 2.10 (a) and (b) present raw cross-sectional images of retinal structure of a gold fish eye. At about 120th frame, retinal structures become slightly

visible over next 20 frames. The visibility was enhanced after processing the raw image in Matlab. Inside of the white circle at Figure 2.11(a) one or two layers are visible between the front and back surface of the structure and also inside of a circle at Figure 2.11(b) one layer is visible. The enhanced images are shown at Figure 2.11 and Figure 2.12. Again the potentiometers of the detector were recalibrated for the retinal imaging because the light power from the sample is extremely low, which changed the balance of previous analog circuit settings. In order to maintain freshness of the eye, the recalibration should have been done quickly as possible, however the procedure required about two hours.

The CMOS smart array detector needs to be improved to provide a user-friendly interface and more stable electrical operation. The current configuration can provide interference fringe intensity of 58 by 58 pixels resolution, but this resolution needs to be more than 256 by 256 pixels to provide better quality imaging. Additionally, if it can provide not only the intensity but also phase information, it can be used in phase sensitive OCT; therefore, one can build fast phase sensitive parallel OCT systems. Also such a device may also be used in phase sensitive parallel OCT.

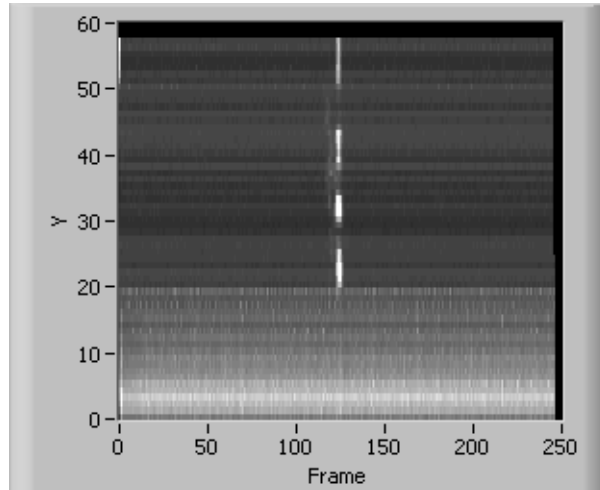
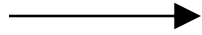


b) Y Cross-Section

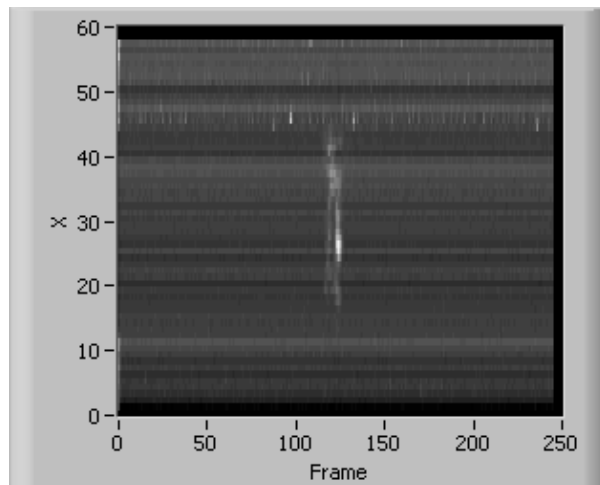
c) X Cross-Section

Figure 2.8 Air force target images of parallel OCT with the CMOS smart array detector  
a) *en face* view of number 3 b) Y cross section at a fixed X position. The circled area is outside of illuminating light and indicates background noise. c) X cross section at a fixed Y position

Scanning direction

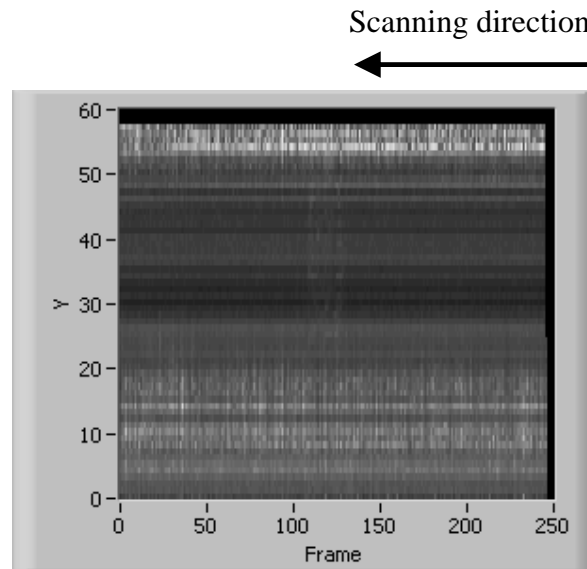


a) X cross-section

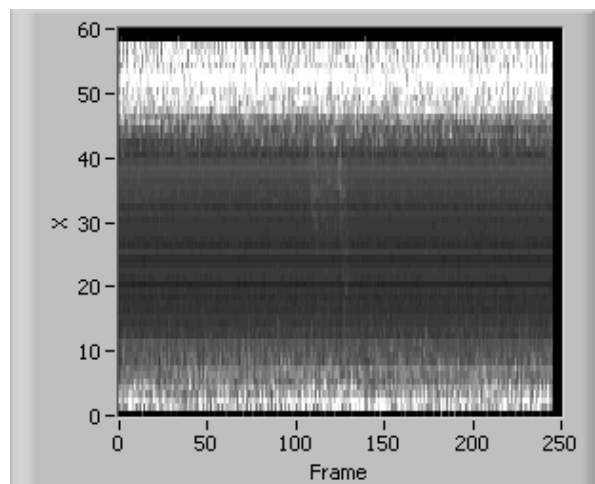


b) Y Cross-section

Figure 2.9 Images of Air force target with a wet tissue taken by parallel OCT with the CMOS smart array detector a) X cross-section view b) Y cross-section view. [Wet tissue is on right side of the target]

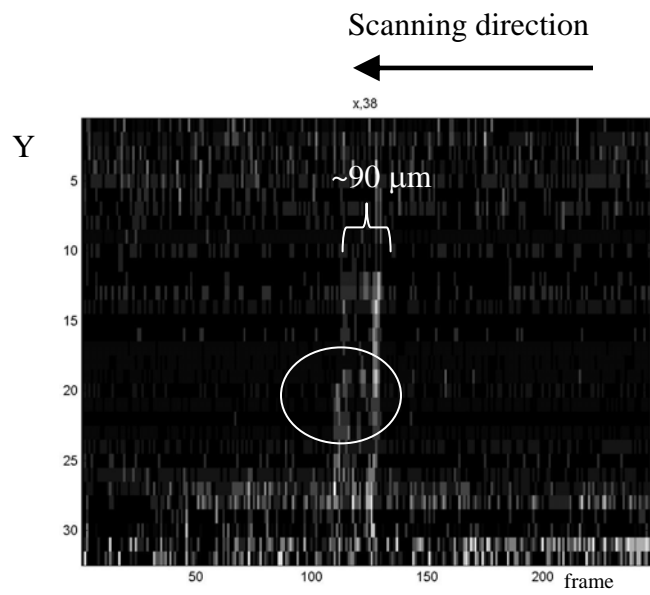


a) X cross section

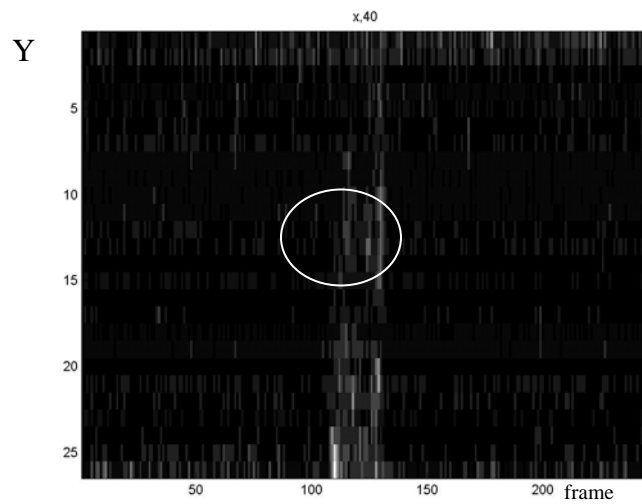


b) Y cross section

Figure 2.10 Gold fish retina images taken by parallel OCT with the CMOS smart array detector, a) X cross-section view, b) Y cross-section view



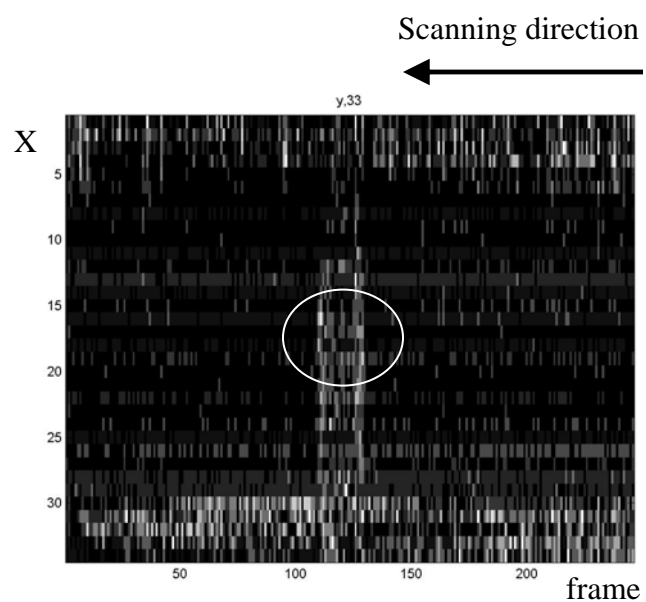
a) X cross-section through a pixel position, 38



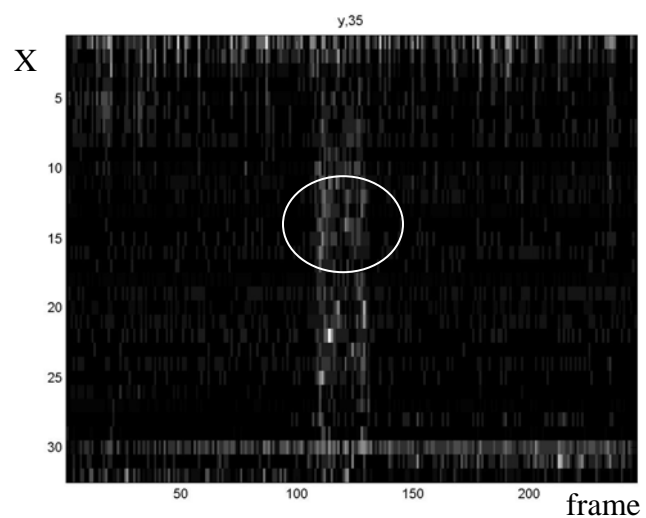
b) X cross-section through a pixel position, 40

Figure 2.11 Gold fish retina image processed images of parallel OCT with the CMOS smart array detector (X cross-section)





a) Y cross-section through a pixel position, 33



b) Y cross-section through a pixel position, 35

Figure 2.12 Gold fish retina processed images of parallel OCT with the CMOS smart array detector (Y cross-section)

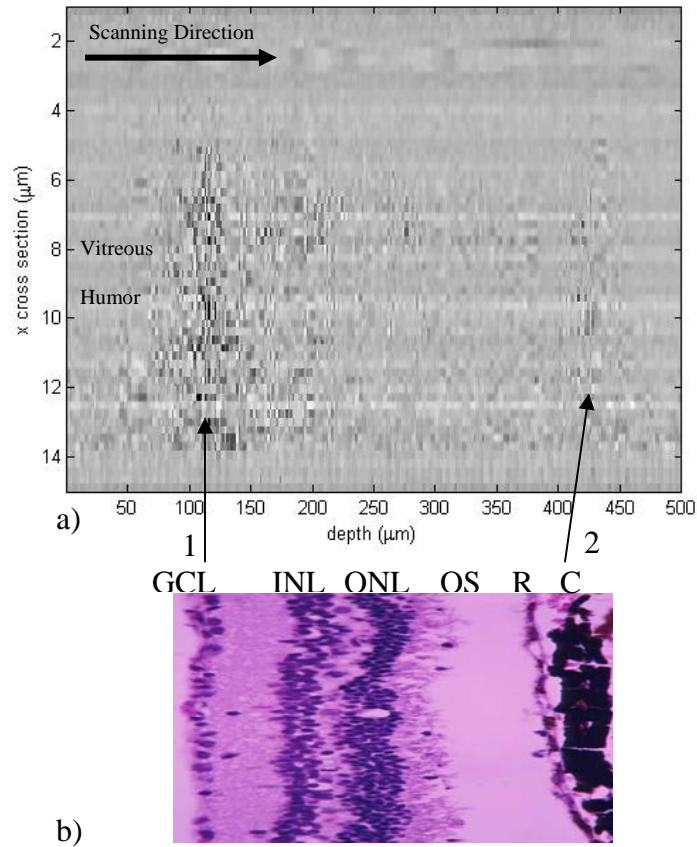


Figure 2.13 a) Cross-sectional *in vivo* hamster retinal image recorded by parallel OCT with the SMART array detector b) H&E stained hamster retinal histology image; GCL: ganglion cell layer, INL: inner nuclear layer, ONL: outer nuclear layer, OS: outer segments, R: retinal epithelium, C: choroid

Figure 2.13(a) presents a cross-sectional *in vivo* hamster retinal image recorded by the parallel OCT with the SMART array detector. The OCT retinal image is compared with a histology section for the hamster retina. The scanning direction is from left to right, and the first boundary indicated by arrow 1 is for the transition from the vitreous humor to the retina. The boundary pointed by arrow 2 is supposed to be the retinal epithelium or the choroid. Thickness between the first and second boundaries is about 300  $\mu\text{m}$  to 350  $\mu\text{m}$ . Several blurred vertical lines can be identified between the two boundaries.

## 2.9. Conclusion

Parallel OCT system was designed and implemented with the CMOS smart array detector. Experimental results of scattering surface targets including a wet tissue on an Air force target, *ex vivo* gold fish retina, and *in vivo* hamster retina are presented. Boundary between the vitreous humor and the ganglion cell layer could be identified in the acquired images. Several other layers between the ganglion cell layer and the choroid layer could be observed even though the contrast between layers was weak.

Controlling of the current version of the CMOS smart array detector requires significant time for maintenance. A more user-friendly interface should be considered in future designs. The 10% fill-factor should also be improved. For *in vivo* hamster retinal imaging, 26 mW light power was illuminated into the eye may have resulted in damages to the retinal layer. Increasing the pixel format should be considered in next design.

Although the current CMOS smart array detector needs improvement, the design is a promising ophthalmologic instrument because it provides fast retinal scanning and prompt display of the acquired images.

## 2.10. References

1. D. Huang, E. A. Swanson, C. P. Lin, J. S. Schuman, W. G. Stinson, W. Chang, M. R. Hee, T. Flotte, K. Gregory, C. A. Puliafito, and J. G. Fujimoto, "Optical Coherence Tomography," *Science* **254**(5035), 1178-1181 (1991).
2. J. G. Fujimoto, "Optical coherence tomography for ultrahigh resolution in vivo imaging," *Nature Biotechnology* **21**(11), 1361-1367 (2003).
3. M. E. Brezinski, G. J. Tearney, S. A. Boppart, B. E. Bouma, E. A. Swanson, J. F. Southern, and J. G. Fujimoto, "High speed catheter based OCT imaging of coronary microstructure," *Circulation* **94**(8), 1494-1494 (1996).
4. W. Drexler, U. Morgner, F. X. Kartner, C. Pitris, S. A. Boppart, X. D. Li, E. P. Ippen, and J. G. Fujimoto, "In vivo ultrahigh-resolution optical coherence tomography," *Optics Letters* **24**(17), 1221-1223 (1999).
5. L. Vabre, A. Dubois, and A. C. Boccara, "Thermal-light full-field optical coherence tomography," *Optics Letters* **27**(7), 530-532 (2002).
6. M. Ducros, M. Laubscher, B. Karamata, S. Bourquin, T. Lasser, and R. P. Salathe, "Parallel optical coherence tomography in scattering samples using a two-dimensional smart-pixel detector array," *Optics Communications* **202**(1-3), 29-35 (2002).
7. S. Bourquin, P. Seitz, and R. P. Salathe, "Two-dimensional smart detector array for interferometric applications," *Electronics Letters* **37**(15), 975-976 (2001).

8. S. Bourquin, V. Monterosso, P. Seitz, and R. P. Salathe, "Video-rate optical low-coherence reflectometry based on a linear smart detector array," *Optics Letters* **25**(2), 102-104 (2000).
9. A. F. Fercher, W. Drexler, C. K. Hitzenberger, and T. Lasser, "Optical coherence tomography - principles and applications," *Reports on Progress in Physics* **66**(2), 239-303 (2003).
10. E. Beaurepaire, A. C. Boccara, M. Lebec, L. Blanchot, and H. Saint-Jalmes, "Full-field optical coherence microscopy," *Optics Letters* **23**(4), 244-246 (1998).
11. M. Laubscher, M. Ducros, B. Karamata, T. Lasser, and R. Salathe, "Video-rate three-dimensional optical coherence tomography," *Optics Express* **10**(9), 429-435 (2002).
12. Z. P. Chen, T. E. Milner, D. Dave, and J. S. Nelson, "Optical Doppler tomographic imaging of fluid flow velocity in highly scattering media," *Optics Letters* **22**(1), 64-66 (1997).
13. D. P. Dave, T. Akkin, and T. E. Milner, "Polarization-maintaining fiber-based optical low-coherence reflectometer for characterization and ranging of birefringence," *Optics Letters* **28**(19), 1775-1777 (2003).
14. J. F. de Boer and T. E. Milner, "Review of polarization sensitive optical coherence tomography and Stokes vector determination," *Journal of Biomedical Optics* **7**(3), 359-371 (2002).
15. D. T. Miller, Qu, J., Jonnal, R.S., Thorn, K., "Coherence gating and Adaptive optics in the Eye," *Proceedings of SPIE* **4956**, 2003 (2003).

16. J. Porter, A. Guirao, I. G. Cox, and D. R. Williams, "Monochromatic aberrations of the human eye in a large population," *Journal of the Optical Society of America a-Optics Image Science and Vision* **18**(8), 1793-1803 (2001).
17. J. W. Hardy, "Active optics:a new technology for the control of light," *Proc. IEEE* **66**, 651-697 (1978).
18. R. K. Tyson, "Principles of Adaptive Optics," Academic press **2nd Edition**(1998).
19. J. Z. Liang and D. R. Williams, "Aberrations and retinal image quality of the normal human eye," *Journal of the Optical Society of America a-Optics Image Science and Vision* **14**(11), 2873-2883 (1997).
20. B. Platt, Shack, R.V., "Lenticular Hartmann-screen," *Opt. Sci. Center Newsl.* **5**(1), 15-16 (1971).
21. J. M. Schmitt, "Optical Coherence Tomography," *IEEE Jounrnal in quantum electronics* **5**(4)(1999).
22. J. G. Fujimoto, M. E. Brezinski, G. J. Tearney, S. A. Boppart, B. Bouma, M. R. Hee, J. F. Southern, and E. A. Swanson, "Optical Biopsy and Imaging Using Optical Coherence Tomography," *Nature Medicine* **1**(9), 970-972 (1995).
23. I. Zeylikovich, Gilerson, A., Alfano, R.R., "Nonmechanical grating-generated scanning coherence microscopy,," *Optics Letter* **23**(23), 1797-1799 (1998).
24. T. Dresel, Hausler, G. , Venzke, H., "Three-dimensional sensing of rough surfaces by coherence radar," *Applied Optics* **31**(7), 919-924 (1992).
25. J. M. Schmitt, S. H. Xiang, and K. M. Yung, "Speckle in optical coherence tomography," *Journal of Biomedical Optics* **4**(1), 95-105 (1999).

26. N. Iftimia, B. E. Bouma, and G. J. Tearney, "Speckle reduction in optical coherence tomography by "path length encoded" angular compounding," *Journal of Biomedical Optics* **8**(2), 260-263 (2003).
27. J. M. Schmitt, "Array detection for speckle reduction in optical coherence microscopy," *Physics in Medicine and Biology* **42**(7), 1427-1439 (1997).
28. M. Bashkansky and J. Reintjes, "Statistics and reduction of speckle in optical coherence tomography," *Optics Letters* **25**(8), 545-547 (2000).
29. A. I. Kholodnykh, I. Y. Petrova, K. V. Larin, M. Motamedi, and R. O. Esenaliev, "Precision of measurement of tissue optical properties with optical coherence tomography," *Applied Optics* **42**(16), 3027-3037 (2003).
30. J. Rogowska and M. E. Brezinski, "Evaluation of the adaptive speckle suppression filter for coronary optical coherence tomography imaging," *Ieee Transactions on Medical Imaging* **19**(12), 1261-1266 (2000).
31. J. Rogowska and M. E. Brezinski, "Image processing techniques for noise removal, enhancement and segmentation of cartilage OCT images," *Physics in Medicine and Biology* **47**(4), 641-655 (2002).
32. J. M. Schmitt, "Restoration of optical coherence images of living tissue using the CLEAN algorithm," *Journal of Biomedical Optics* **3**(1), 66-75 (1998).
33. M. D. Kulkarni, C. W. Thomas, and J. A. Izatt, "Image enhancement in optical coherence tomography using deconvolution," *Electronics Letters* **33**(16), 1365-1367 (1997).



34. K. M. Yung, S. L. Lee, and J. M. Schmitt, "Phase-domain processing of optical coherence tomography images," *Journal of Biomedical Optics* **4**(1), 125-136 (1999).
35. B. Karamata, P. Lambelet, M. Laubscher, R. P. Salathe, and T. Lasser, "Spatially incoherent illumination as a mechanism for cross-talk suppression in wide-field optical coherence tomography," *Optics Letters* **29**(7), 736-738 (2004).
36. L. Buttner and J. Czarske, "Multi-mode fibre laser Doppler anemometer (LDA) with high spatial resolution for the investigation of boundary layers," *Experiments in Fluids* **36**(1), 214-216 (2004).
37. L. Mandel and E. Wolf, "Optical Coherence and Quantum Optics," Cambridge, 664-666 (1995).
38. H. Ambar, Y. Aoki, N. Takai, and T. Asakura, "Fringe Contrast Improvement in Speckle Photography by Means of Speckle Reduction Using Vibrating Optical Fiber," *Optik* **74**(2), 60-64 (1986).
39. H. Ambar, Y. Aoki, N. Takai, and T. Asakura, "Relationship of Speckle Size to the Effectiveness of Speckle Reduction in Laser Microscope Images Using Rotating Optical Fiber," *Optik* **74**(1), 22-26 (1986).
40. N. Takai and T. Asakura, "Statistical Properties of Laser Speckles Produced under Illumination from a Multimode Optical Fiber," *Journal of the Optical Society of America a-Optics Image Science and Vision* **2**(8), 1282-1290 (1985).
41. J. W. Goodman, "Introduction to Fourier Optics," (1996).

42. P. Dufour, G. Rousseau, and N. McCarthy, "Optical noise reduction in a femtosecond Ti:sapphire laser," *Proceedings of the SPIE - The International Society for Optical Engineering* **4833**, 894-899 (2002).
43. I. Hartl, X. D. Li, C. Chudoba, R. K. Hganta, T. H. Ko, J. G. Fujimoto, J. K. Ranka, and R. S. Windeler, "Ultrahigh-resolution optical coherence tomography using continuum generation in an air-silica microstructure optical fiber," *Optics Letters* **26**(2001).
44. G. J. Tearney, B. E. Bouma, and J. G. Fujimoto, "High-speed phase- and group-delay scanning with a grating-based phase control delay line," *Optics Letters* **22**(1997).
45. A. M. Rollins, M. D. Kulkarni, S. Yazdanfar, R. Ung-arunyawee, and J. A. Izatt, "In vivo video rate optical coherence tomography," *Optics Express* **3**(1998).
46. J. F. de Boer, T. E. Milner, M. J. C. van Gemert, and J. S. Nelson, "Two-dimensional birefringence imaging in biological tissue by polarization-sensitive optical coherence tomography," *Optics Letters* **22**(1997).
47. G. J. Tearney, M. E. Brezinski, J. F. Southern, B. E. Bouma, M. R. Hee, and J. G. Fujimoto, "Determination of the refractive index of highly scattering human tissue by optical coherence tomography," *Optics Letters* **20**(1995).
48. A. Knüttel and M. Boehlau-Godau, "Spatially confined and temporally resolved refractive index and scattering evaluation in human skin performed with optical coherence tomography," *J. Biomed. Opt.* **5**(1), 83-92 (2000).

49. D. P. Dave and T. E. Milner, "Optical low-coherence reflectometer for differential phase measurement," *Opt. Lett.* **25**(4), 227 (2000).
50. D. P. Dave and T. E. Milner, "Phase-sensitive frequency-multiplexed optical low-coherence reflectometry," *Opt. Comm.* **193**, 39-43 (2001).
51. W. T. Welford, "Aberrations of Optical Systems," Hilger, Bristol, UK (1986).
52. W. J. Smith, "Modern Optical Engineering: The Design of Optical Systems," McGraw-Hill, New York (1990).
53. H. C. Howland and B. Howland, "Subjective Method for Measurement of Monochromatic Aberrations of Eye," *Journal of the Optical Society of America* **67**(11), 1508-1518 (1977).
54. R. J. Noll, "Zernike Polynomials and Atmospheric-Turbulence," *Journal of the Optical Society of America* **66**(3), 207-211 (1976).
55. J. Schwiegerling and J. E. Greivenkamp, "Using corneal height maps and polynomial decomposition to determine corneal aberrations," *Optometry and Vision Science* **74**(11), 906-916 (1997).
56. M. B. a. E. Wolf, "Principles of Optics," Cambridge **7th edition**(1999).
57. T. H. Ko, D. C. Adler, J. G. Fujimoto, D. Mamedov, V. Prokhorov, V. Shidlovski, and S. Yakubovich, "Ultrahigh resolution optical coherence tomography imaging with a broadband superluminescent diode light source," *Optics Express* **12**(10), 2112-2119 (2004).

## **Chapter 3 OCT Speckle Reduction by a Partially Spatial Coherent Source**

### **3.1. Abstract**

Speckle in OCT images originates in the high spatial coherence of incident light that allows interference of light backscattered from spatially heterogeneous tissue specimens. We report results of a numerical simulation and an experiment to test speckle reduction by using a partially spatial coherent source. A Gaussian-Schell model for a partially spatial coherent source is used in the OCT simulation. For the experiment, such a source was generated by a spatially coherent broadband light source and a multimode fiber. Advantage in using a multimode fiber is that such a source can provide a large number of photons in a small coherence volume. To illustrate speckle reduction with a partially spatial coherent source, we recorded low-coherence interferograms of a scattering surface using single mode and multimode source fibers. Interferograms recorded using a single mode source fiber are indicative of those observed using conventional OCT. Speckle in OCT image recorded using a multimode source fiber is substantially reduced.

### 3.2. Introduction

Optical Coherence Tomography (OCT) uses the short temporal coherence properties of broadband light to extract structural information from heterogeneous samples such as tissue. Two approaches are recognized to generate two- three-dimensional OCT images; single-point raster scanning<sup>1-4</sup> versus parallel/wide field imaging<sup>5-8</sup>. Speckle is a major obstacle in measuring specific structural properties (e.g., birefringence<sup>9-11</sup>) of tissue specimens and observing specific features that approach the diffraction limit<sup>12</sup>. Although speckle in OCT images is still being investigated, a common view is that the effect originates in distorted wavefronts of light returning from tissue that result in random appearing constructive and destructive features in the interferogram.

Speckle reduction methods have been addressed by several investigators and include post-signal processing<sup>17-22</sup>, angular compounding<sup>13-16</sup>, and use of spatially incoherent illumination<sup>23</sup>. Post-signal processing techniques have been reported including a zero-amplitude procedure<sup>22</sup>, deconvolution, and rotating kernel transformation. Zero-amplitude procedure (ZAP), which operates in the complex number domain, shows speckle reduction in OCT images but blurs boundaries between tissue structures. Other complex-number-domain processing methods applied to OCT include iterative point deconvolution, (i.e. CLEAN<sup>20</sup>), and constrained iterative deconvolution<sup>21</sup>. Deconvolution techniques require some prior knowledge of the point-spread function of the imaging optics<sup>24</sup>, as well as optical properties of the imaged sample. Computation time of the rotating kernel transformation (RKT) technique, applied by Rogowsk *et al*<sup>18</sup> increases substantially with kernel size. Angular compounding methods are based on

acquiring/averaging multiple beams each with a different incidence/reflecting angle from the sample but have disadvantages of either time-restricted implementation or high complexity.

Use of spatially incoherent illumination with a thermal light source has neither time constraints nor high complexity, but suffers from reduced signal to noise ratio due to low photon number per spatial mode<sup>23</sup>. Since average number of photons within a coherence volume for thermal light sources is of order unity, these sources are non-degenerate<sup>25</sup>. Use of quasi-homogeneous (partially spatial coherent) illumination has long been recognized to improve lateral resolution by decreasing speckle in recorded images<sup>25-27</sup>. Although partially spatial coherent illumination can be easily implemented using a multimode optical fiber<sup>28</sup>, application in OCT imaging has not been reported possibly due to problems associated with modal dispersion and alignment constraints.

This chapter presents a mathematical analysis and an experimental result showing a simple and fast method to reduce speckle in OCT imaging using a partially spatial coherent light source generated by a multimode fiber. Although coherence length of this source is reduced, photon number per spatial mode is much larger than unity. The chapter is organized as follows: first we derive an interferometric imaging equation for an OCT system utilizing a Gaussian-Schell model light source; a numerical simulation and experimental setup are described in Sec. 2. Experimental results are presented in Sec. 3 and discussion in Sec. 4, summary and conclusions follow in Sec. 5.

### 3.3. Theory and Methods

Figure 3.1 shows a two-beam imaging Michelson interferometer. Broad-band and partially spatial coherent light is emitted from a source and illuminates sample and a reference mirror that are imaged onto a CCD camera by lens L3. Spatial coordinates at the sample, reference, and CCD camera are denoted by  $(\xi, \zeta)$ ,  $(\xi', \zeta')$ , and  $(x, z)$  respectively.  $\xi$ ,  $\xi'$  and  $x$  are in a plane perpendicular to light propagation, while  $\zeta$ ,  $\zeta'$ , and  $z$  are along a line parallel to light propagation. Amplitude of light,  $A_{s,m}$ , at the CCD camera plane produced from the sample reflection can be written as a coherent integral<sup>29</sup> of amplitudes backscattered from the sample modulated by point-spread function  $[h(\cdot)]$  and the local reflectivity  $[r(\xi)]$ ,

$$A_{s,m}(x, \nu) = \int_{-\infty}^{\infty} A_{i,m}(\xi, \nu) r(\xi) \cdot e^{-j2\pi\nu\tau} h(x - \xi, \nu) d\xi \quad (3.1)$$

where subscripts  $s$ ,  $m$  indicate sample and a spatial mode of the incident field, respectively. The factor  $e^{-j2\pi\nu\tau}$  is included to account for the optical path length difference between reference and sample paths and will become important later when sample and reference beams are combined.

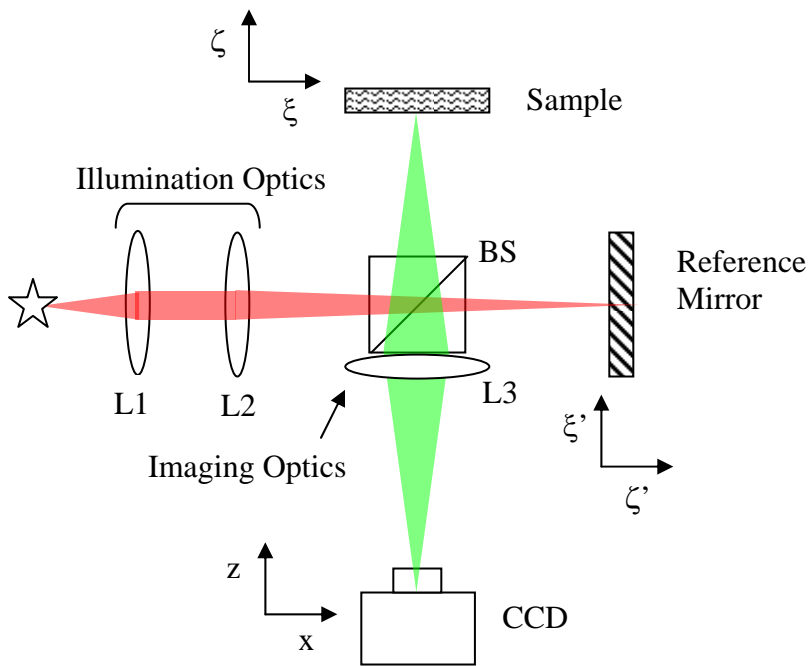


Figure 3.1 Imaging Michelson interferometer with wide-field illumination



In Eq. 3.1 we assume amplitude of light returning from the sample is the simple product of the incident amplitude  $[A_{i,m}(\xi, \nu)]$  and local reflectivity  $[r(\xi)]$ . In thick heterogeneous media such as tissue amplitude of light returning from the sample is an integral of incident amplitude with tissue refractive index  $[n(\xi)]$ . Similarly the amplitude field,  $A_{r,m}$ , at the CCD camera plane imaged from the reference mirror can be written,

$$A_{r,m}(x, \nu) = \int_{-\infty}^{\infty} A_{i,m}(\xi', \nu) r_{mir} h(x - \xi', \nu) d\xi' \quad (3.2)$$

where subscripts  $r, m$  indicate the reference and a spatial mode of the incident field, respectively, and  $r_{mir}$  is a constant reflectivity of the mirror.

When sample and reference fields ( $A_{s,m}$  and  $A_{r,m}$ ) interfere at the image plane, intensity at position  $x$  consists of two DC intensity components and a fringe signal. The fringe signal is a complex correlation between amplitudes returned from sample and reference paths. Detected signal can be written,

$$\begin{aligned} I_{d,m}(x, \nu, \tau) &= \left\langle \left| A_{s,m}(x, \nu, \tau) + A_{r,m}(x, \nu) \right|^2 \right\rangle \\ &= I_{s,m}(x, \nu) + I_{r,m}(x, \nu) + 2 \operatorname{Re} \left\langle A_{s,m}(x, \nu, \tau) A_{r,m}^*(x, \nu) \right\rangle \end{aligned} \quad (3.3)$$

where  $I_{s,m}(x, \nu)$ ,  $I_{r,m}(x, \nu)$  are the DC intensities from sample and reference paths respectively, represented by,

$$I_{s,m}(x, \nu) = \iint \left\langle A_{i,m}^*(\xi'', \nu, \tau) A_{i,m}(\xi, \nu, \tau) \right\rangle r^*(\xi'') r(\xi) h^*(x - \xi'', \nu) h(x - \xi, \nu) d\xi d\xi'' \quad (3.4-a)$$

$$I_{r,m}(x, \nu) = \iint \left\langle A_{i,m}(\xi', \nu) A_{i,m}^*(\xi''', \nu) \right\rangle |r_{mir}|^2 h(x - \xi', \nu) h^*(x - \xi''', \nu) d\xi' d\xi''' \quad (3.4-b)$$

Expressions for  $I_s(x, \nu)$ ,  $I_r(x, \nu)$  are the well-known imaging equations for partially spatial coherent light<sup>25</sup>.

The complex fringe signal for spatial mode  $[m]$  and optical frequency  $[\nu]$  is given by,

$$I_{f,m}(x, \nu, \tau) = \left\langle A_{s,m}(x, \nu, \tau) A_{r,m}^*(x, \nu) \right\rangle \quad (3.5)$$

$$= r_{mir} \int_{-\infty}^{\infty} \int_{-\infty}^{\infty} \left\langle A_{i,m}(\xi, \nu) A_{i,m}^*(\xi', \nu) \right\rangle r^*(\xi) \cdot e^{-j2\pi\nu\tau} h(x - \xi, \nu) h^*(x - \xi', \nu) d\xi d\xi'$$

Inclusion of the complex sample reflectivity  $[r(\xi)]$  distinguishes the interference imaging equation (Eq. 3.5) from reference and sample intensity integrals (Eq. 3.4).

By summing over all spatial modes  $[m]$  and optical frequencies  $[\nu]$ , expression for the complex fringe signal  $I_f(x, \tau)$  becomes,

$$I_f(x, \tau) = \sum_m \int_{-\infty}^{\infty} \left\langle A_{s,m}(x, \nu, \tau) A_{r,m}^*(x, \nu) \right\rangle d\nu \quad (3.6)$$

Superposition of all spatial modes reduces the degree of spatial coherence and can be modeled by a Gaussian-Schell model source.

The Gaussia-Schell model expression of the complex fringe can be written as

$$I_f(x, \tau) = r_{mir} \int_{-\infty}^{\infty} \int_{-\infty}^{\infty} \int_{-\infty}^{\infty} W(\xi, \xi', \nu) r(\xi) \cdot e^{-j2\pi\nu\tau} h(x - \xi) h^*(x - \xi') d\xi d\xi' d\nu \quad (3.7)$$

where we have neglected the optical frequency  $[\nu]$  dependence of the point-spread function  $[h(\cdot)]$  and local reflectivity  $[r(\xi)]$ . The cross-spectral density  $[W(\xi, \xi', \nu)]$  can be modeled as a Gaussian-Schell model source having the form,

$$W(\xi, \xi', \nu) = [S(\xi, \nu)]^{1/2} [S(\xi', \nu)]^{1/2} g(\xi - \xi', \nu) \quad (3.8)$$

with

$$S(\xi, \nu) = A^2(\nu) \exp(-\xi^2 / 2\sigma_s^2(\nu)), \quad (3.9)$$

$$g(\xi - \xi', \nu) = \exp\left[-(\xi - \xi')^2 / 2\sigma_g^2(\nu)\right], \quad (3.10)$$

representing the spectral density and the spectral degree of coherence of light with positive values  $\sigma_s$  and  $\sigma_g$ . The source power spectral density is given by  $A^2(\nu)$ . Values of  $\sigma_s$  and  $\sigma_g$ , which generally depend on optical frequency  $[\nu]$ , determine the effective widths of the beam and spatial coherence, respectively across the beam spot at the sample or the reference mirror. The limit  $\sigma_g \ll \sigma_s$  represents a globally incoherent (the so-called quasi-homogeneous) source, while the opposite limit  $\sigma_g \gg \sigma_s$  corresponds to a completely coherent source. The point-spread function with a square aperture with width  $D$  is,

$$h(x - \xi) = \text{sinc} \left[ \frac{D}{c \cdot z} \nu_0 (x - \xi) \right] \quad (3.11)$$

where  $z$  is the distance between the sample and lens, and  $c$  is speed of light,  $\nu_0$  is center optical frequency of the source power spectral density.

If the power spectral density,  $A^2(\nu)$ , is given as,

$$A^2(\nu) = \exp \left[ -\frac{(\nu - \nu_0)^2}{2\Delta\nu^2} \right] \quad (3.12)$$

where  $\Delta\nu$  is the FWHM spectral width of the source, we can evaluate Eq. 3.7.

Substituting Eqs. 3.8, 3.11, 3.12 into the complex fringe signal (Eq. 3.7) and integrating over  $\nu$ , we find,

$$\begin{aligned} I_f(x, \tau) = & \sqrt{\pi} \exp(-i\pi\tau\nu_0) \exp \left( -\frac{\pi^2\tau^2}{2\Delta\nu^2} \right) \iint \text{sinc} \left[ \frac{D}{c \cdot z} \nu_0 (x - \xi) \right] \text{sinc} \left[ \frac{D}{c \cdot z} \nu_0 (x - \xi') \right] r(\xi) \\ & \times \left( \frac{1}{2\Delta\nu^2} + A(\xi, \xi') \right) \exp(-A(\xi, \xi')\pi^2\tau^2) d\xi d\xi' \end{aligned} \quad (3.13)$$

where  $\sigma_s$  and  $\sigma_g$  are dependent on optical frequency  $[\nu]$  and estimated as  $\sigma_s(\nu_0)\frac{\nu_0}{\nu}$  and

$\sigma_g(\nu_0)\frac{\nu_0}{\nu}$  respectively, and  $A(\xi, \xi')$  is,

$$A(\xi, \xi') = \frac{\sigma_g(\nu_0)^2(\xi^2 + \xi'^2) + 2\sigma_s(\nu_0)^2(\xi - \xi')^2}{4\sigma_s(\nu_0)^2\sigma_g(\nu_0)^2\nu_0^2}$$

We note that the complex fringe signal,  $I_f(x, \tau)$ , in Eq. 3.13 contains the OCT complex fringe signal with carrier frequency  $[\exp(-i\pi\tau\nu_0)]$  with envelope  $[\exp(-\pi^2\tau^2/2\Delta\nu^2)]$ , but also a multiplicative term which is the integral over spatial coordinates  $[\xi, \xi']$ . The integral over  $\xi, \xi'$  accumulates in regions where the point spread functions are non-zero and is proportional to  $r(\xi)$ . Because the phase of  $r(\xi)$  can fluctuate with sample position  $\xi$ , the multiplicative term introduces speckle.

Because the exact form of the complex reflectivity of the sample  $[r(\xi)]$  is not generally known we evaluate the statistics of  $I_f(x, \tau)$ . We assume that the local complex reflectivity  $[r(\xi)]$  in a sample has a fixed amplitude distribution  $[r(\xi)]$  with randomly varying but uniformly distributed phase<sup>13</sup> $[\phi_k]$ . The complex fringe signal at position  $x$  in Eq. 3.13 can be viewed as a sum of all field amplitudes backscattered back within a coherence patch. Each field amplitude backscattered from the sample contributes as a complex-valued phasor at position  $x$  in the observation plane. The complex fringe signal with speckle can be analyzed as a random phasor sum,

$$I_f = a \exp(i\theta) = \frac{1}{N} \sum_{k=1}^N \alpha_k \exp(i\phi_k) \quad (3.14)$$

The amplitude  $[\alpha_k]$  represents the comprehensive amplitude terms in Eq. 3.13 and  $\exp(i\phi_k)$  is the randomly varying phase of the complex reflectivity of the sample. Probability density function of the amplitude of the random phasor sum follows a Rayleigh function and has mean and variance,

$$\bar{a} = \sqrt{\frac{\pi}{2}}\sigma$$

$$\sigma_a^2 = (2 - \frac{\pi}{2})\sigma^2 \quad (3.15)$$

where  $\sigma^2$  is the second moment  $\overline{\alpha^2}$  divided by two. Mean and variance of the amplitude are only dependent on and proportional to the second moment  $\overline{\alpha^2}$ . Although the second moment of the complex fringe signal can be calculated analytically by finding the second derivative of a characteristic function after integrating over  $\xi'$  in Eq. 3.13, but this study includes a numerical evaluation of the second moment of the complex fringe signal, Eq. 3.13, with variable coherent size  $[\sigma_g]$ .

### 3.3.1. Numerical Simulation

Because speckle in OCT arises from coherent interference of backscattered light from the sample, we investigate speckle reduction by considering a Gaussian-Schell model source with different spatial coherence lengths ( $\sigma_g$ ) used in conjunction with a one-dimensional rough surface. The complex fringe signal (Eq. 3.13) is computed along a line using software written by the author. We assume pupil of lens L3 has a diameter of

1 cm and is placed 10 cm away from the sample or reference mirror giving an  $NA = 0.1$ . Width of the point spread function (PSF) is calculated to be  $1.2\lambda_o/NA = 8.5 \mu\text{m}$  assuming  $\lambda_o = 850 \text{ nm}$ . Grid spacing for  $\xi$  and  $\xi'$  is  $0.34 \mu\text{m}$  or 25 times smaller than the PSF width. Beam spot diameter ( $\sigma_s$ ) at the sample and the reference mirror is set at  $\sigma_s = 100 \mu\text{m}$  and several spatial coherent lengths ( $\sigma_g$ ) of the Gaussian-Schell model source are chosen to observe the speckle reduction effect. Sample reflectivity is set at unity between  $40 \mu\text{m}$  to  $60 \mu\text{m}$ , and zero elsewhere. The phases vary from  $-\pi$  to  $\pi$  with uniformly distributed random probability. The image plane is positioned at 10 cm from lens L3 and complex fringe signal  $[I_f(x)]$  space is computed over  $[x = 0, 100 \mu\text{m}]$  at discrete points separated by  $1 \mu\text{m}$ .

### 3.3.2. Experimental Setup

A depth-resolving OCT system based on a two-beam Michelson interferometer was constructed to investigate speckle reduction using a partially spatial coherent source. Partially spatial coherent light was generated from a coherent light source by using a long segment of high NA multimode optical fiber. For coherent illumination, we used a single mode fiber with a cutoff wavelength  $\lambda_c = 800 \text{ nm}$ . Both single- and multi-mode optical fibers are placed in the source path of a Michelson interferometer to investigate effect of source coherence length on speckle reduction. First, we used a 100 m long, 0.48 NA multimode glass optical fiber with a  $200 \mu\text{m}$  core diameter, producing about 63,000 coherent spatial modes<sup>30</sup>. Second, we used a 30 m long single mode optical fiber (Rifocs Corp.) similar to that used in a conventional OCT setup. In both cases, a mode-locked

Ti:Sapphire laser with an output centered at 850 nm and spectral width  $\Delta\lambda \sim 50$  nm is coupled into the fibers and used as source light. When coupled into a single mode fiber, light gives a  $TEM_{00}$  spatial mode. In the first setup (Figure 3.2), light is coupled into a multimode fiber to generate many spatial modes. The 100 m long multimode fiber is mounted on a spool to reduce any variations in mechanical stress that might introduce variable mode coupling. Following the multimode fiber, lens L2 directs light into both sample and reference paths through a broadband beam splitter (BS). In the second setup using a single mode fiber, the multimode fiber is removed from the source path of the interferometer. Backscattered light from both sample and reference paths are imaged onto a CCD camera (FASTCAM Super 10K) using focusing lens (L3).

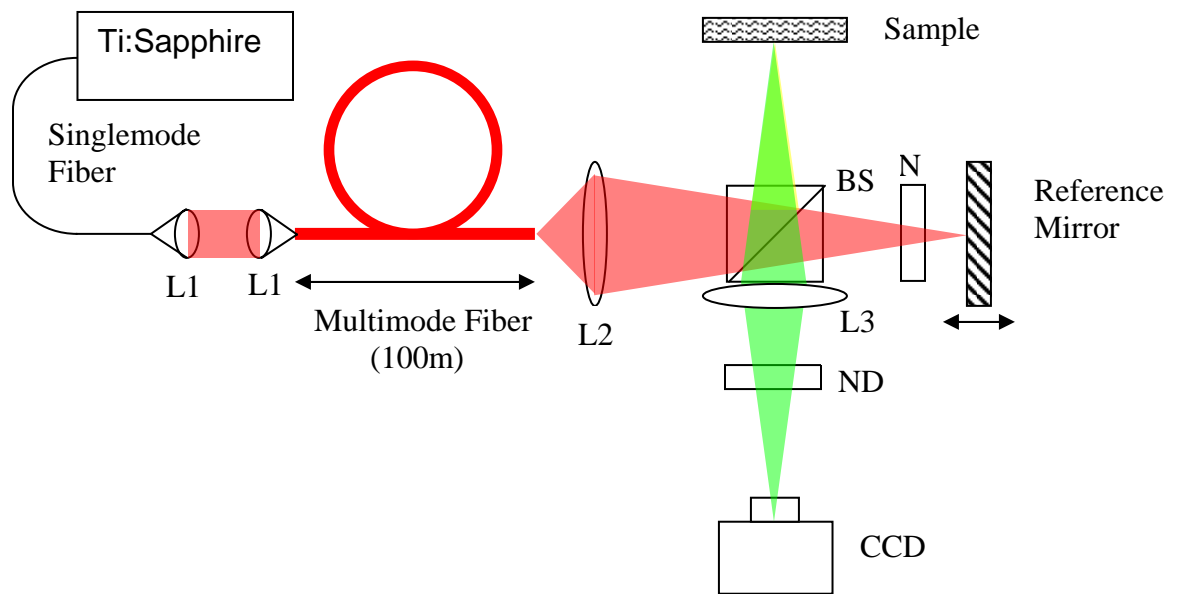


Figure 3.2 Optical setup with multimode fiber in source path of Michelson interferometer.

L1 ( $f = 10 \text{ mm}$ ), L2 ( $f = 150 \text{ mm}$ ), and L3 ( $f = 100 \text{ mm}$ ): lenses, BS: Beam splitter, ND: Neutral density filter



A voice coil with a retro-reflector is used in the reference path to provide variable time delay ( $\tau$ ) between sample and reference paths. The voice coil is driven by a function generator creating a sinusoidal wave at 0.1 Hz and 10 V<sub>p-p</sub>. Scan range is 1.6 mm yielding a fringe carrier frequency  $f_c = 752$  Hz. Frame rate of the CCD camera is set at 3000 frames/sec sampling the fringe at 4 points per cycle or twice the Nyquist limit. Integration time of the camera is 50  $\mu$ s. Output images from the CCD camera are recorded in digital video (DV) format to avoid any loss in spatial resolution. Incoherent demodulation is used to determine the envelope of the complex fringe signal, Eq. 3.13, from recorded three-dimensional data cubes. Fringe amplitude is determined at each pixel in time (Figure 3.3). Other than incoherent demodulation no additional image enhancement is used.

A mill-finished aluminum plate is used as a scattering surface. The rough surface of the aluminum plate produces speckles caused by distorted wavefronts in backscattered light. The aluminum plate was tilted slightly to produce a uniform phase gradient and produce linear fringes in the CCD. For comparison, the same physical location covering a 2 mm beam diameter on the aluminum plate is imaged with both single and multimode fiber systems. To maximize fringe visibility and to avoid saturation of CCD photocells, light intensity incident on the CCD camera was adjusted by using a neutral density filter in the detection path of the interferometer.

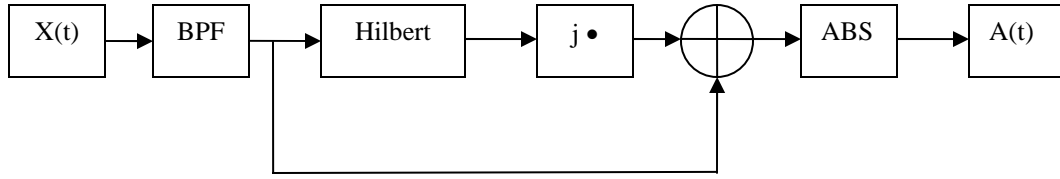


Figure 3.3 Flow diagram for incoherent demodulation.  $X(t)$ : detected signal, BPF: band pass filter, Hilbert: Hilbert transform, ABS: absolute value,  $A(t)$ : envelope of the detected signal

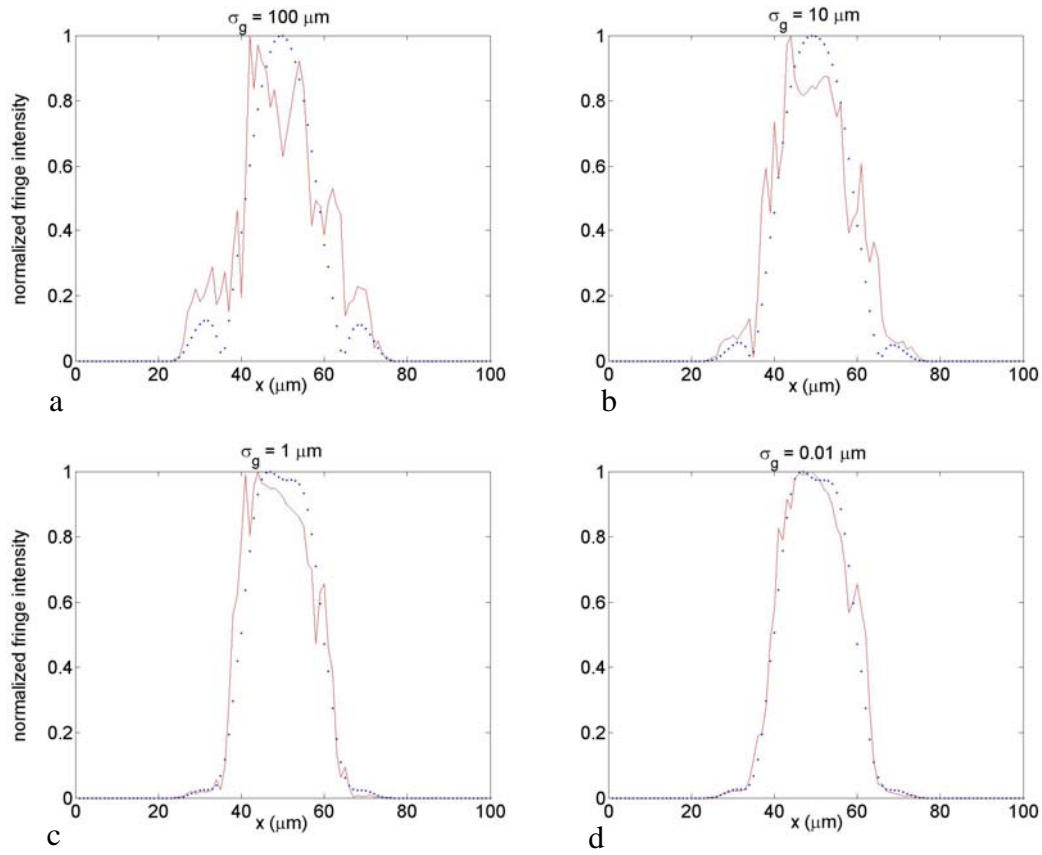


Figure 3.4 Simulated normalized fringe intensity for different spatial coherence lengths of Gaussian-Schell model source.  $\sigma_g$ : coherence length of a Gaussian-Schell model source

given at Eq. 3.10. Solid lines: complex fringe signal with speckle, and dotted lines: envelope of complex fringe signal without speckle. Beam spot size at target ( $\sigma_s$ ) was set at 100  $\mu\text{m}$ .

### 3.4. Results

Effect of speckle reduction in OCT imaging was simulated using a Gaussian-Schell model source and Eq. 3.13 for  $I_f(x, \tau)$ . For this simulation, the illuminating beam spot [ $\sigma_s$ ] was fixed at 100  $\mu\text{m}$ . Simulation results shown in Figure 3.4 and Figure 3.5, Table 3.1 are determined for a depth-resolving OCT system with several different spatial coherent lengths ( $\sigma_g$ ) corresponding to a Gaussian-Schell model source. In Figure 3.4 dotted lines represent the envelope of the complex fringe signal without speckle, while solid lines are with speckle. The speckle-free case was simulated by removing the random phase term in Eq. 3.14. Coherent illumination [ $\sigma_g = \sigma_s = 100 \mu\text{m}$ ] produces the greatest speckle (Figure 3.4 (a)). For incoherent illumination, spatial coherence length was set much smaller ( $\sigma_g = 0.01 \mu\text{m}$ ) than diameter [ $\sigma_s$ ] of the illuminating beam (Figure 3.4 (d)). Two additional spatial coherence lengths ( $\sigma_g = 10, 1 \mu\text{m}$ ) in Figure 3.4 (b) and (c) respectively, were investigated to demonstrate speckle reduction with decreasing coherence length. To assess speckle reduction quantitatively, speckle root-mean-square (r.m.s.) values were calculated by subtracting computed complex fringe signal with speckle from the speckle-free case. Speckle r.m.s. variation with spatial coherence

length ( $\sigma_g$ ) is shown in Table 3.1. Entries in Table 3.1 were computed by averaging 30 simulations for each spatial coherence length ( $\sigma_g$ ).

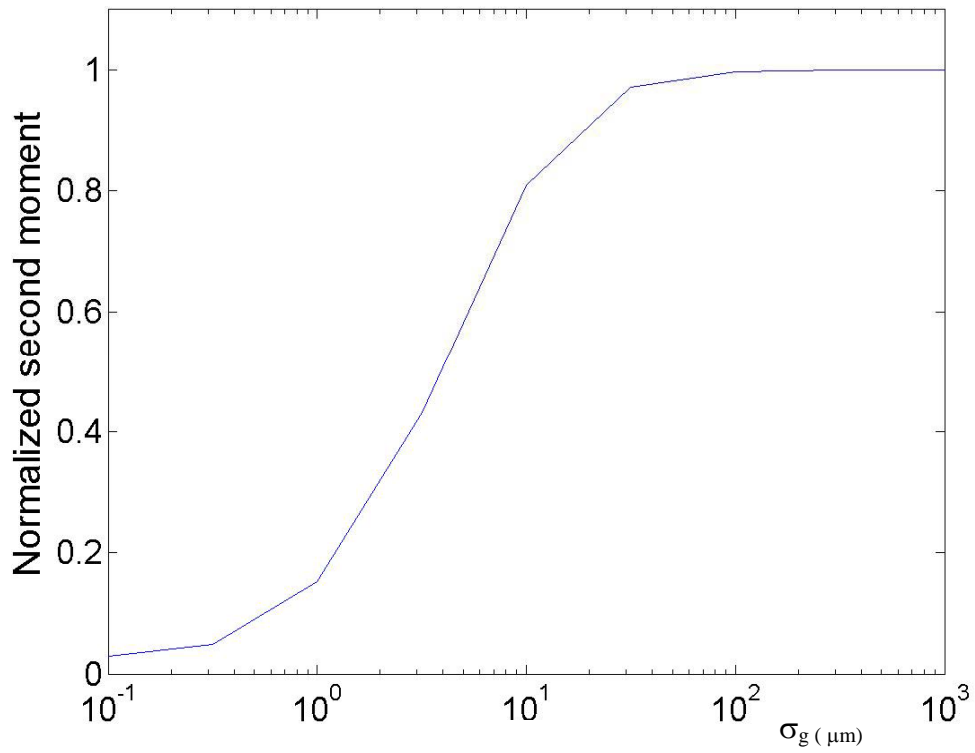


Figure 3.5 Second moment of normalized complex fringe signal vs. spatial coherence length ( $\sigma_g$ )

Table 3.1 Speckle r.m.s. variation according to spatial coherence length ( $\sigma_g$ )

$\sigma_g$ ( $\mu\text{m}$ )	Speckle r.m.s.
100	0.188
10	0.174
1	0.081
0.1	0.031

Note the logarithmic scale to display  $\sigma_g$ .

To observe difference in sample illumination through single or multimode fibers, light from the reference path was blocked and the aluminum plate was placed in the sample path. Figure 3.6 (a) and (b) show intensity images of the sample when illuminated by single mode and multimode fibers respectively. Due to a small mode field diameter (5  $\mu\text{m}$ ) at the single mode fiber tip, Airy rings in the illuminated area are observed in Figure 3.6 (a), whereas relatively flat illumination is evident in the multimode case (Figure 3.6 (b)).

After restoring the reference path, an interference pattern was measured by the CCD camera corresponding to a 1.6 mm pathlength delay between sample and reference paths. During measurement of the interference pattern, no significant motion artifacts in the fringes, caused by environmental changes, were observed. Measured interference patterns were demodulated using an incoherent demodulation algorithm (Figure 3.3).

Figure 3.7 (a) and (b) show OCT cross-sectional images of the sample at a fixed height, with the normalized complex fringe signal represented along the vertical axis, recorded with single-mode and multimode fiber systems, respectively. When using the multimode fiber for illumination, speckle is significantly reduced (Figure 3.7 (b)) compared to that recorded using the single mode fiber (Figure 3.7 (a)).

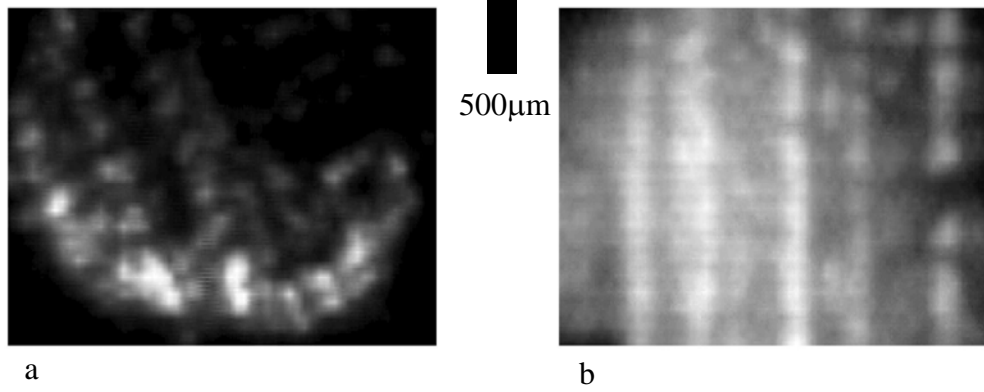


Figure 3.6 CCD camera images of metallic scattering surface through (a) single mode, (b) multimode source fiber. Reference path of interferometer is blocked.

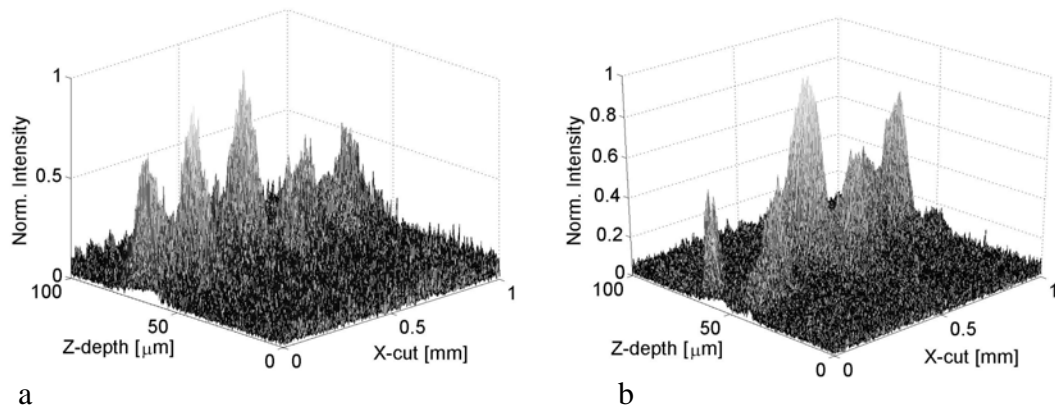


Figure 3.7 Cross-sectioned Parallel OCT image recoded from a scattering surface using: (a) single mode, (b) multimode source fiber. Fringe intensities are normalized and correspond to a single depth scan.

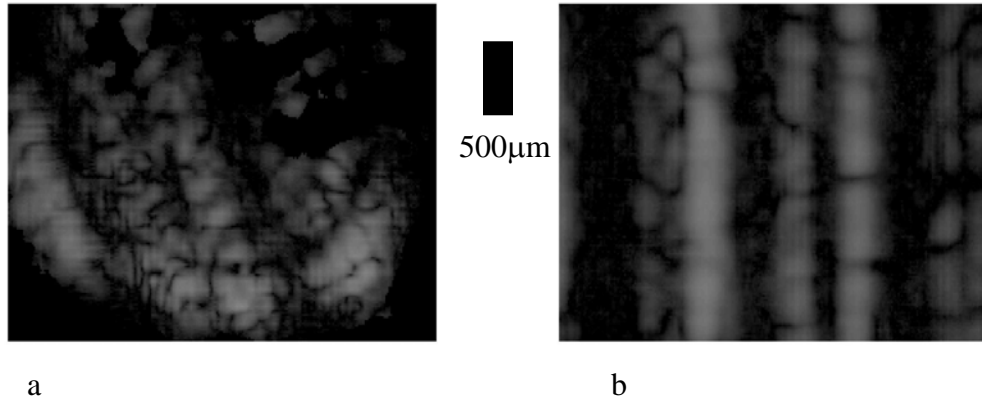


Figure 3.8 Low coherence interferograms recorded from a scattering surface using: (a) single mode, (b) multimode source fiber

Table 3.2 Noise comparison between multimode and single mode source fiber setups

	$\sigma_{re}$	$\sigma_{sh}$ (multimode)	$\sigma_{sh}$ (singlemode)
Calculated Noise	9.25μV	10.12nV	27.2nV
Measured Noise	9.8μ	11.73nV	28nV



Demodulated interference patterns at a fixed depth recorded with single- and multi-mode fiber systems are shown in Figure 3.8 (a) and Figure 3.8 (b) respectively. For comparison, both images were recorded at the same position on the aluminum plate, so micro-irregularities of the surface are identical. The image in Figure 3.8 (a) was recorded after rotating the aluminum plate 20 degrees counterclockwise. The image recorded using the multimode fiber, Figure 3.8 (b), shows continuous linear fringes corresponding to tilt of the aluminum plate, whereas the image recorded using single mode fiber for illumination, Figure 3.8 (a), displays disrupted and fragmented bright grey bands over the surface due to speckle.

### **3.5. Discussion**

Light emitted from a Gaussian-Schell model source considered here has a variable degree of spatial coherence from incoherent to fully coherent. When partially spatial coherent light is launched into the interferometer, the beam may be regarded as an assembly of mutually uncorrelated finite-sized phase cells. In OCT, light input into the interferometer is divided into two beams, which illuminate the sample and the reference mirror. While mirror reflectivity in the reference path is considered constant, the sample has a complex reflectivity function and back-scatters incident light. When light backscattered from sample and reference paths recombine at the detection plane, cells of the beams overlap and interfere partially. Interference can occur only for light originating from the same phase cell in sample and reference paths. The speckled appearance of the images in Figure 3.8 is the effect of interference between light

backscattered from different particles within a coherence area. With a decrease in the coherence area, speckle reduction is expected, as indicated in Table 3.2, but as Figure 3.8 (d) illustrates speckle still exists despite a very small spatial coherence length ( $\sigma_g = 0.01 \mu\text{m}$ ) corresponding to incoherent illumination.

An interesting point when looking at the complex fringe signal, Eq. 3.13, as a random phasor sum is that speckle increases with the second moment of the complex fringe signal which follows the second moment  $[\overline{\alpha^2}]$  of the amplitude  $[\alpha_k]$ , not the random phase distribution  $[\phi_k]$ . The second moment,  $\overline{\alpha^2}$ , of the intensity fluctuation increases as the degree of coherence increases and approaches unity for a spatially coherent beam. The second moment never reaches zero even at the smallest spatial coherence length.

Producing incoherent sources has an inherent trade-off in view of radiation efficiency and the degeneracy parameter<sup>25</sup>. The radiant emittance of a partially spatial coherent source is expressed<sup>31</sup> by,

$$E_\nu(\rho) = C_g(\nu)S(\rho, \nu)$$

where the radiation efficiency  $[C_g]$  is a proportionality factor between radiant emittance  $[E_\nu(\rho)]$  and spectral density  $[S(\rho, \nu)]$ . The radiation efficiency increases monotonically with  $\sigma_g$ , from zero for a completely incoherent source to unity for a completely coherent source<sup>31</sup>. The degeneracy parameter indicates average number of identical photons (same polarization state) that are contained in a coherence volume. For example, use of spatially incoherent illumination with a thermal light source suffers from a low degeneracy

number<sup>23</sup>. Advantage in using a multimode fiber to produce partially spatial coherent light is high number of photons per coherence volume. The source and multimode fiber used in experiments reported here provided  $0.3 \times 10^9$  photons per coherence volume substantially higher than that provided by a thermal source. Spatial coherence length at the tip of the multimode fiber was calculated<sup>32,33</sup> to be 22  $\mu\text{m}$  by

$$\sigma_g = \sqrt{\frac{4\sigma_0^2}{\left(\frac{\pi D \cdot NA}{2\lambda}\right)^2 - 1}}$$

where  $D$  is a core diameter of multimode fiber and NA is numerical aperture.

In Eq. 3.1 we assumed amplitude of light returning from the sample is the product of the incident amplitude  $[A_{s,m}(\xi, \nu)]$  and the local reflectivity  $[r(\xi)]$ , which is reasonable for the scattering object studied. In tissue, however, the amplitude of light returning from the sample will be a complex function of  $A_{s,m}(\xi, \nu)$  due to multiple photon paths in the tissue and spatial variation of the refractive index of the tissue.

Speckle reduction using partially spatial coherent sources can be also understood as an incoherent mode summation. When broadband light is coupled into a multimode fiber, a number of orthogonal spatial modes are generated which are spatially and temporally coherent. Each spatial mode propagates through the multimode fiber at a distinct group velocity producing modal dispersion. After propagating a sufficient length along the fiber, spatial modes become temporally decorrelated due to differences in group velocity. Detected interference is an incoherent sum of interferograms formed between spatial modes. Because each mode forms a statistically independent speckle field, mode

summation has the effect of reducing speckle by averaging. The appearance of unbroken grooves in the multimode fiber case, (Figure 3.8(b)) is consistent with the speckle reduction effect resulting from superposition of many interferograms each representing mutually incoherent spatial modes.

As sample-reference path length delay increases, the delay may compensate the mode separation introduced by the multimode fiber, and the decorrelated modes become correlated again. To avoid this intermodal interference, the multimode fiber should be sufficiently long so that the modal separation is much greater than maximum sample-reference delay time in scanning.

To verify no intermodal interference was present in our system, signal-to-noise ratios for single mode and multimode cases were measured and compared across the full scanning range (1.6 mm) of the voice coil stage. A mirror was placed in the sample path with a photo-receiver and 100  $\mu\text{m}$  pinhole in the detection path replaced the CCD camera. We express noise sources in terms of the photocurrent variance  $\sigma_i^2$ . Primary noise sources include receiver ( $\sigma_{re}^2$ ), and shot noise ( $\sigma_{sh}^2$ ). Intensity noise was omitted because of the small contribution from a mode locked laser<sup>34</sup>. Receiver noise was calculated from the manufacturer's specification. Shot noise is given by,

$$\sigma_{sh}^2 = 2qI_{dc}B$$

where  $I_{dc}$  represents the mean detector photocurrent, and  $B$  is the electronic detection bandwidth, and  $q$  is the charge on an electron.

Total photocurrent variance is given by,

$$\sigma_i^2 = \sigma_{re}^2 + \sigma_{sh}^2$$

Measured and calculated shot noises are compared in Table 3.2. The shot noise is calculated from the mean detector photocurrent,  $I_{dc}$ . Measured shot noise is comparable with calculated values.

We define SNR as peak to peak current of the coherence function divided by the total photocurrent standard variance  $[\sigma_i]$ . SNRs were 80 dB and 79 dB over 1.6 mm of reference and sample path delays for single mode and multimode fiber cases respectively. Small difference in SNR between coherent and partially spatial coherent cases indicates degradation of SNR due to the multimode source fiber was insignificant and supports the hypothesis that mode separation between adjacent modes is longer than the scanning range (1.6 mm) after 100 m of travel through the multimode fiber. Mode cross coupling in the fiber was below the measurement limit over the entire scan (1.6 mm).

### 3.6. Conclusion

We have proposed and demonstrated a speckle reduction method using a partially spatial coherent source in a Michelson interferometer in a parallel detecting OCT system. Speckle in interferograms recorded using a partially spatial coherent source is substantially reduced compared to the fully coherent case. No degradation in SNR is observed, and no measurable mode cross-coupling is observed in the multimode fiber. A partially spatial coherent source is also preferable for *en face* imaging not only for reducing speckle but also for eliminating Airy rings in the image caused by the small field diameter of most single mode fibers. Results of our simulations using a Gaussian-

Schell model source in OCT and experiments indicate that broadband light sources with reduced spatial coherence that provide a large number of photons per coherence volume may be effectively utilized to reduce speckle in OCT interferograms.

### 3.7. References

1. D. Huang, E. A. Swanson, C. P. Lin, J. S. Schuman, W. G. Stinson, W. Chang, M. R. Hee, T. Flotte, K. Gregory, C. A. Puliafito, and J. G. Fujimoto, "Optical Coherence Tomography," *Science* **254**(5035), 1178-1181 (1991).
2. J. G. Fujimoto, "Optical coherence tomography for ultrahigh resolution in vivo imaging," *Nature Biotechnology* **21**(11), 1361-1367 (2003).
3. M. E. Brezinski, G. J. Tearney, S. A. Boppart, B. E. Bouma, E. A. Swanson, J. F. Southern, and J. G. Fujimoto, "High speed catheter based OCT imaging of coronary microstructure," *Circulation* **94**(8), 1494-1494 (1996).
4. W. Drexler, U. Morgner, F. X. Kartner, C. Pitris, S. A. Boppart, X. D. Li, E. P. Ippen, and J. G. Fujimoto, "In vivo ultrahigh-resolution optical coherence tomography," *Optics Letters* **24**(17), 1221-1223 (1999).
5. L. Vabre, A. Dubois, and A. C. Boccara, "Thermal-light full-field optical coherence tomography," *Optics Letters* **27**(7), 530-532 (2002).
6. M. Ducros, M. Laubscher, B. Karamata, S. Bourquin, T. Lasser, and R. P. Salathe, "Parallel optical coherence tomography in scattering samples using a two-dimensional smart-pixel detector array," *Optics Communications* **202**(1-3), 29-35 (2002).
7. S. Bourquin, P. Seitz, and R. P. Salathe, "Two-dimensional smart detector array for interferometric applications," *Electronics Letters* **37**(15), 975-976 (2001).

8. S. Bourquin, V. Monterosso, P. Seitz, and R. P. Salathe, "Video-rate optical low-coherence reflectometry based on a linear smart detector array," *Optics Letters* **25**(2), 102-104 (2000).
9. Z. P. Chen, T. E. Milner, D. Dave, and J. S. Nelson, "Optical Doppler tomographic imaging of fluid flow velocity in highly scattering media," *Optics Letters* **22**(1), 64-66 (1997).
10. D. P. Dave, T. Akkin, and T. E. Milner, "Polarization-maintaining fiber-based optical low-coherence reflectometer for characterization and ranging of birefringence," *Optics Letters* **28**(19), 1775-1777 (2003).
11. J. F. de Boer and T. E. Milner, "Review of polarization sensitive optical coherence tomography and Stokes vector determination," *Journal of Biomedical Optics* **7**(3), 359-371 (2002).
12. D. T. Miller, Qu, J., Jonnal, R.S., Thorn, K., "Coherence gating and Adaptive optics in the Eye," *Proceedings of SPIE* **4956**, 2003 (2003).
13. J. M. Schmitt, S. H. Xiang, and K. M. Yung, "Speckle in optical coherence tomography," *Journal of Biomedical Optics* **4**(1), 95-105 (1999).
14. N. Iftimia, B. E. Bouma, and G. J. Tearney, "Speckle reduction in optical coherence tomography by "path length encoded" angular compounding," *Journal of Biomedical Optics* **8**(2), 260-263 (2003).
15. J. M. Schmitt, "Array detection for speckle reduction in optical coherence microscopy," *Physics in Medicine and Biology* **42**(7), 1427-1439 (1997).



16. M. Bashkansky and J. Reintjes, "Statistics and reduction of speckle in optical coherence tomography," *Optics Letters* **25**(8), 545-547 (2000).
17. A. I. Kholodnykh, I. Y. Petrova, K. V. Larin, M. Motamedi, and R. O. Esenaliev, "Precision of measurement of tissue optical properties with optical coherence tomography," *Applied Optics* **42**(16), 3027-3037 (2003).
18. J. Rogowska and M. E. Brezinski, "Evaluation of the adaptive speckle suppression filter for coronary optical coherence tomography imaging," *Ieee Transactions on Medical Imaging* **19**(12), 1261-1266 (2000).
19. J. Rogowska and M. E. Brezinski, "Image processing techniques for noise removal, enhancement and segmentation of cartilage OCT images," *Physics in Medicine and Biology* **47**(4), 641-655 (2002).
20. J. M. Schmitt, "Restoration of optical coherence images of living tissue using the CLEAN algorithm," *Journal of Biomedical Optics* **3**(1), 66-75 (1998).
21. M. D. Kulkarni, C. W. Thomas, and J. A. Izatt, "Image enhancement in optical coherence tomography using deconvolution," *Electronics Letters* **33**(16), 1365-1367 (1997).
22. K. M. Yung, S. L. Lee, and J. M. Schmitt, "Phase-domain processing of optical coherence tomography images," *Journal of Biomedical Optics* **4**(1), 125-136 (1999).
23. B. Karamata, P. Lambelet, M. Laubscher, R. P. Salathe, and T. Lasser, "Spatially incoherent illumination as a mechanism for cross-talk suppression in wide-field optical coherence tomography," *Optics Letters* **29**(7), 736-738 (2004).

24. L. Buttner and J. Czarske, "Multi-mode fibre laser Doppler anemometer (LDA) with high spatial resolution for the investigation of boundary layers," *Experiments in Fluids* **36**(1), 214-216 (2004).
25. L. Mandel and E. Wolf, "Optical Coherence and Quantum Optics," Cambridge, 664-666 (1995).
26. H. Ambar, Y. Aoki, N. Takai, and T. Asakura, "Fringe Contrast Improvement in Speckle Photography by Means of Speckle Reduction Using Vibrating Optical Fiber," *Optik* **74**(2), 60-64 (1986).
27. H. Ambar, Y. Aoki, N. Takai, and T. Asakura, "Relationship of Speckle Size to the Effectiveness of Speckle Reduction in Laser Microscope Images Using Rotating Optical Fiber," *Optik* **74**(1), 22-26 (1986).
28. N. Takai and T. Asakura, "Statistical Properties of Laser Speckles Produced under Illumination from a Multimode Optical Fiber," *Journal of the Optical Society of America a-Optics Image Science and Vision* **2**(8), 1282-1290 (1985).
29. J. W. Goodman, "Introduction to Fourier Optics," (1996).
30. M. Young, "Optics and Lasers Including Fibers and Optical Waveguides," Springer **5th Edition**(2000).
31. L. Mandel, Wolf, E., "Optical coherence and quantum optics," Cambridge, 298~300 (1995).
32. M. Santarsiero, F. Gori, R. Borghi, G. Cincotti, and P. Vahimaa, "Spreading properties of beams radiated by partially coherent Schell-model sources," *Journal*

- of the Optical Society of America a-Optics Image Science and Vision **16**(1), 106-112 (1999).
33. L. Buettner and J. Czarske, "A multimode-fibre laser-Doppler anemometer for highly spatially resolved velocity measurements using low-coherence light," *Measurement Science & Technology* **12**(11), 1891-1903 (2001).
34. P. Dufour, G. Rousseau, and N. McCarthy, "Optical noise reduction in a femtosecond Ti:sapphire laser," *Proceedings of the SPIE - The International Society for Optical Engineering* **4833**, 894-899 (2002).

## **Chapter 4 Spatial Refractive Index Measurement of Porcine Artery Using Differential Phase OCT (DP OCT)**

### **4.1. Abstract**

We describe a methodology to record spatial variation of refractive index of porcine renal artery using differential phase optical coherence tomography (DP-OCT). DP-OCT provides a quantitative measure of thin specimen phase retardation and refractive index with phase resolution of 5 nm and lateral resolution of 3  $\mu\text{m}$ . DP-OCT instrumentation is an all-fiber, dual channel Michelson interferometer constructed using polarization maintaining fiber. Two orthogonal polarization modes of light are spatially separated using a Wollaston prism and directed into separate photo-receivers. Because phase noise in the environment is equally present in both channels, computation of phase difference between the two signal channels is attributed exclusively to variation in the specimen's composite refractive index. Porcine renal artery is freshly harvested from a local slaughter house. The lumen is cut open and sectioned in 5  $\mu\text{m}$  thickness. A microscopic slide for the tissue section is processed by standard histology method with mounting media. Two-dimensional en face dual-channel phase images are recorded over a 150  $\mu\text{m} \times 200 \mu\text{m}$  region on the microscopic slide and the images are reconstructed by plotting relative phase variation as the OCT beam is moved across the artery cross section.

Keywords: phase sensitive OCT, refractive index, relative phase retardation

## 4.2. Introduction

Optical coherence tomography (OCT) has emerged as an important optical imaging modality in noninvasive medical diagnostics. OCT generates high resolution images by utilizing the cross correlation between broadband light backscattered from a test specimen and reference reflector. Various technical approaches have been developed to improve OCT spatial resolution<sup>1, 2</sup>, imaging acquisition rate<sup>3, 4</sup>, and image quality<sup>5, 6</sup>. Most of these techniques use the fringe amplitude or a combination of fringe amplitude and polarization information in backscattered light<sup>7</sup>. Magnitude of backscattered light is dependent on the local refractive index gradients of the structural components comprising the test specimen. Polarization information basically reveals different phase retardation, caused by a tissue, between two orthogonal polarization states of light.

Knowledge of local refractive index variations in biological tissue is not only one of basic importance in tissue optics but also a major factor that determines fringe signal variation in conventional OCT. Average refractive index over relatively homogeneous tissue medium has been measured by Tearney et al<sup>8</sup>, Wang et al, and Knüttel et al<sup>9</sup>. The basic approach presented by Tearney et al<sup>8</sup> was to adjust the reference mirror for maximum signal at a particular focus position within a tissue; whereas Knüttel et al<sup>9</sup>

adapted moving fiber tip/collimating lens in sample path in order to trace maximum signal variation.

This paper presents a method to image refractive index distribution over a tissue specimen placed on a microscope slide that is processed by standard histology. The paper is organized as follows: In Sec. 2, DP-OCT instrumentation and signal processing for imaging the refractive index distribution is outlined. Sample preparation and sample path optics are described in Sec. 3. Results of the experiment (Sec. 4) and a summary and conclusion follow in Sec 5.

### **4.3. DP-OCT Instrumentation and Signal Processing**

Details of the DP-OCT used for refractive index profiling can be found in <sup>10, 11</sup>. A simplified schematic diagram is shown at Figure 4.1.

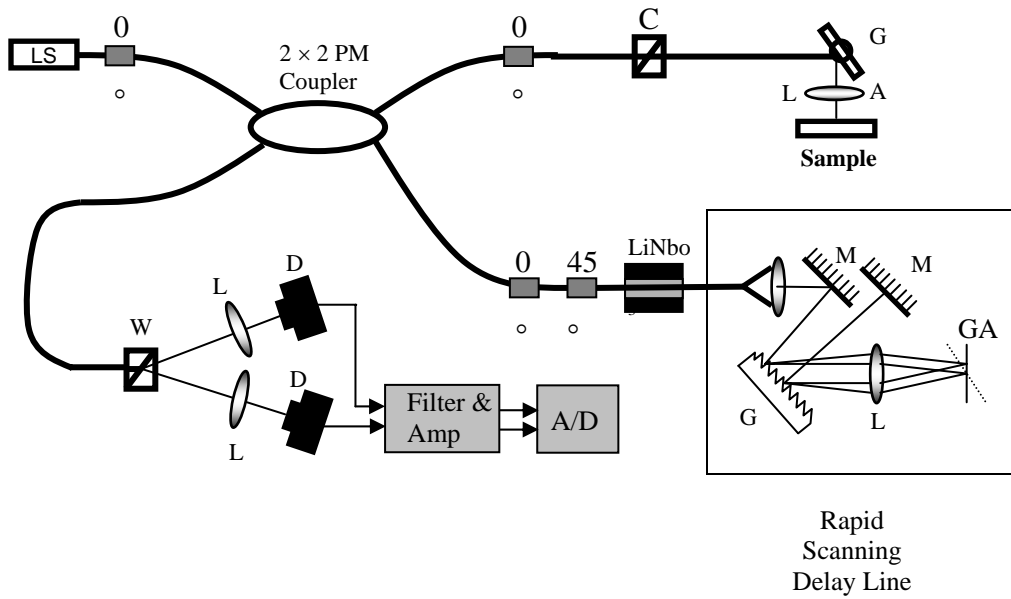


Figure 4.1 Schematic diagram of the DP-OCT system. LS: Broadband light source, L: lens, G: diffraction grating, M: mirror, D: photo-receiver, W: Calcite Wollaston prism, GA: galvanometer, C: Calcite prism. A splice is depicted by a rectangle between fibers and the value indicates the angle in degrees between the slow or fast axes of the two spliced PM fiber segments.

The DP-OCT system is essentially a dual-channel Michelson interferometer with two independent channels corresponding to orthogonal polarization modes of polarization maintaining (PM) optical fiber. At the interferometer input, light emitted from a broadband source ( $\lambda_0 = 1.31 \mu\text{m}$  and  $\Delta\lambda_{\text{FWHM}} \sim 60 \text{ nm}$ ) is coupled into a PM optical fiber based Michelson interferometer. In the reference path, an electro-optic phase modulator varies the optical path length giving a stable 50 kHz carrier frequency. A rapid scanning

delay line<sup>3</sup> is used to compensate dispersion introduced by the phase modulator. To record two-dimensional images lateral scanning is done by a galvanometer and a motorized micro-positioning stage. Coherence functions are longitudinally displaced so that recorded fringes correspond to reflection from the tissue-glass interfaces so that no depth scan is necessary for this measurement. In the detection path, the two orthogonal polarization channels are separated by a Wollaston prism and focused onto respective photo-receivers. The detected interference signal in each channel is bandpass filtered, digitized by a 12-bit analog-to-digital converter, and stored in computer memory.

The phase of the interference signal in each channel is calculated by computing the analytic signal using the Hilbert transform. When the phase difference,  $\Delta\phi = \phi_f - \phi_s$ , between the two channels is evaluated, the common-mode phase noise present in both channels is removed.

The relative optical pathlength difference ( $\Delta pathlength$ ) across the sample is proportional to the phase difference between the two channels by a factor given by the central wavelength ( $\lambda_0$ ) divided by  $4\pi$ . The equation containing the double-pass proportionality constant is shown below.

$$\Delta pathlength = \frac{\Delta\phi \cdot \lambda_0}{4\pi}$$

Measurement of relative optical pathlength difference on the order of 2 nm is possible.



#### 4.4. Sample Preparation and Sample Arm Optics Setup

A schematic diagram of the sample path optics is shown in Figure 4.2. Two orthogonal polarization modes propagate from the tip of the sample arm PM fiber after being collimated by a lens. This light group is then decorrelated by a birefringent prism pair. The prism pair introduces a relative pathlength delay between the two orthogonal polarization modes. The amount of delay is set to produce interference fringes from light backscattered from the coverglass-tissue and tissue-coverglass interfaces. Only one channel experiences phase retardation due to propagation through tissue that is determined by computing the phase difference ( $\phi$ ) in post-processing.

The two co-propagating channels are backscattered off a scanning mirror and directed through an objective lens (40X, NA = 1.4), producing a 3  $\mu\text{m}$  FWHM beam diameter in the focal plane. To create a two-dimensional image, the beam is scanned laterally across the sample using the scanning mirror and a motorized micro-positioning stage. The scanning mirror and motorized stage are driven respectively at 625Hz and 10 Hz.

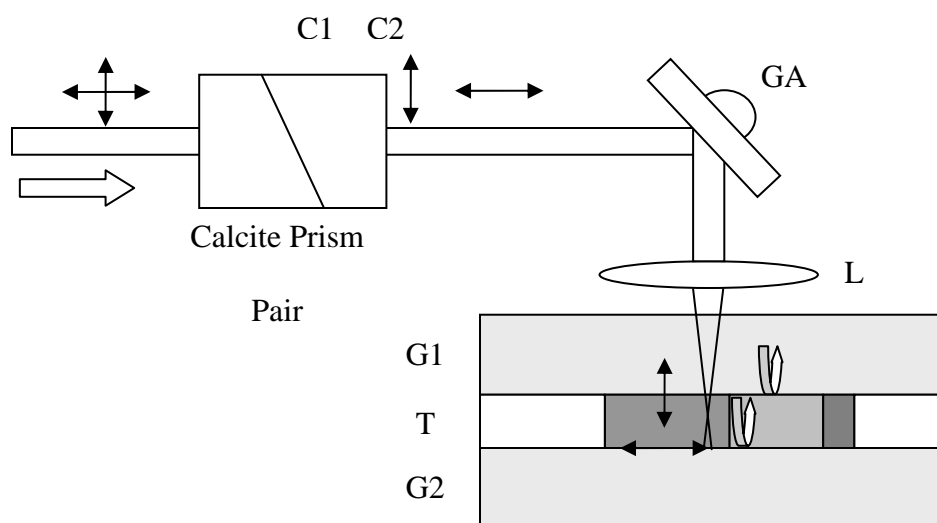


Figure 4.2 Sample path optics. C:channel, GA:Galvonometer, L:lens, G:coverglass, T:tissue section. Channels become decorrelated after propagation through the calcite prism pair. The phase lag between channels are determined by tissue thickness ( $\sim 5 \mu\text{m}$ )

A freshly harvested porcine renal artery is obtained at a local abattoir. The lumen of the artery is cut axially to open flat against a mounting surface. Using standard histology slide preparation procedures, the marked region is cut from the intima to adventitia in  $5 \mu\text{m}$  thick sections. The tissue section is placed on a microscopic slide with mounting media (PermaFluor<sup>TM</sup>) with a coverglass ( $150 \mu\text{m}$  thickness). Another tissue section is processed in the same manner but with elastin-staining. The elastin-stained slide shows elastin fibers as dark in color to allow easy comparison with the refractive

index distribution image recorded using DP-OCT. The flipped unstained slide is placed at the focal point of the objective lens in the sample path.

## 4.5. Results and Discussion

Two-dimensional *en face* scanning is performed over a  $150\text{ }\mu\text{m} \times 200\text{ }\mu\text{m}$  region and the images are reconstructed by plotting relative phase variation as the OCT beam is moved across the artery cross section. Two adjacent images are recorded to cover the entire artery. Figure 4.3 (a) shows *en face* relative phase retardation image of the intima and media area of the porcine renal artery. The retardation between channels is solely produced by the  $5\text{ }\mu\text{m}$  thickness of tissue section. The color bar positioned at the left side of the image is phase retardation in radians. Figure 4.3 (b) shows digitized elastin-stained histology of the artery. In this picture, the intima is located at the bottom surface of the tissue, and internal elastic lamina (IEL) shows as thick dark line on top of the intima surface. The microscope picture (Figure 4.3(b)) is recorded at slightly different orientation with the OCT image (Figure 4.3(a)).

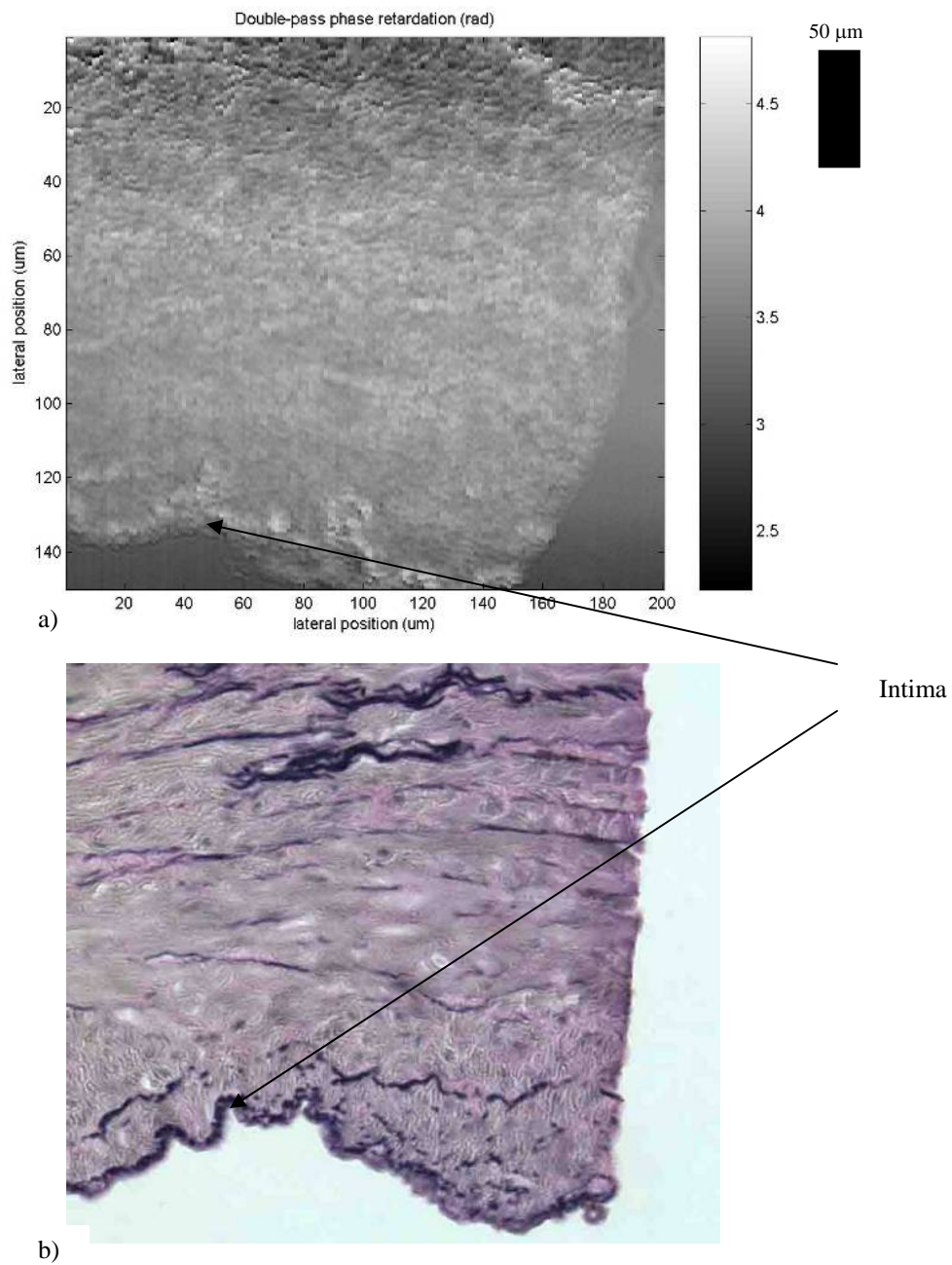


Figure 4.3 Porcine renal artery (intima and media). a) phase retardation map. The color bar represents phase retardation in radians. b) elastin stained histology section.

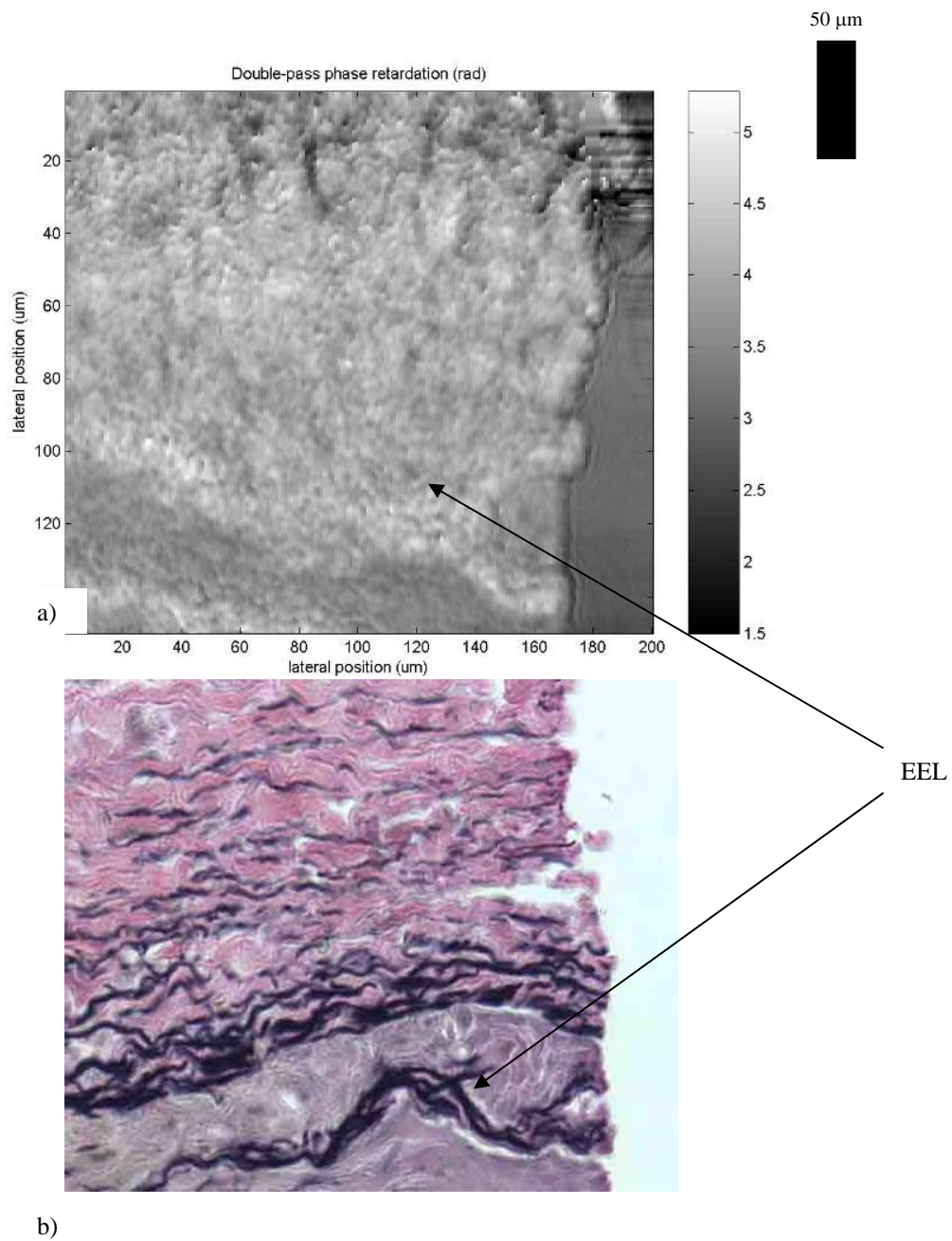


Figure 4.4 Porcine renal artery (media and adventitia). a) phase retardation map. The color bar represents phase retardation in radians. b) Elastin stained histology section.

The IEL consists of thick elastin fibers that are thought to have higher refractive index than collagen or surrounding cells. In the phase retardation image (Figure 4.3(a) and Figure 4.4(b)) this IEL refractive index is quantified as higher phase retardation than surrounding. From the upper area of the IEL, the media region contains collagen or smooth muscle cells but sometimes elastin fibers appear that are also visible in the phase retardation image.

Figure 4.4(a) shows an *en face* phase retardation image of the media and adventitia areas, and Figure 4.4(b) is similarly located elastin-stained histology. The arrows represent external elastic lamina that forms the boundary between the media and adventitia. Upper area of EEL is adventitia that has plenty of relatively thick elastin fibers. This area appears darker on the phase image implying refractive indices in this region are higher than those in the media.

Relative refractive index can be calculated from the relative phase difference by,

$$\Delta n = \frac{\Delta\Phi \cdot \lambda_0}{2\pi \cdot 2S}$$

where  $\lambda_0$  is the center wavelength of the light source (1.3  $\mu\text{m}$ ), and  $S$  is the tissue thickness (5  $\mu\text{m}$ ).  $\Delta\Phi$  is phase retardation displayed in Fig 4.3(a) and Figure 4.4(b). Absolute refractive index can be calculated by adding the refractive index of the mounting media.

$$n_{ab} = n_{ref} + \Delta n$$

Knowledge of the precise thickness and refractive index of the mounting media are essential for accurate refractive index of tissue. Precise refractive index value of the

mounting media was not measured, so the true refractive index of the tissue was not computed.

#### **4.6. Conclusion**

DP-OCT has the capability of imaging quantitative optical phase retardation of tissue sections. The relative phase retardation image of porcine renal artery is taken after the cross section of the lumen is processed for histology. The retardation image can be directly related to refractive index of the tissue with knowledge of the refractive index of the mounting media and tissue thickness.

## 4.7. References

1. Drexler, W., et al., *In vivo ultrahigh-resolution optical coherence tomography*. Optics Letters, 1999. **24**(17): p. 1221-1223.
2. Hartl, I., et al., *Ultrahigh-resolution optical coherence tomography using continuum generation in an air-silica microstructure optical fiber*. Optics Letters, 2001. **26**.
3. Tearney, G.J., B.E. Bouma, and J.G. Fujimoto, *High-speed phase- and group-delay scanning with a grating-based phase control delay line*. Optics Letters, 1997. **22**.
4. Rollins, A.M., et al., *In vivo video rate optical coherence tomography*. Optics Express, 1998. **3**.
5. Shmitt, J.M., *Restoration of optical coherence images of living tissues using the CLEAN algorithm*. J. Biomed. Opt., 1998. **3**(1): p. 66-75.
6. Baskansky, M. and J. Reintjes, *Statistics and reduction of speckle in optical coherence tomography*. Optics Letter, 2000. **25**(8): p. 545-547.
7. de Boer, J.F., et al., *Two-dimensional birefringence imaging in biological tissue by polarization-sensitive optical coherence tomography*. Optics Letters, 1997. **22**.
8. Tearney, G.J., et al., *Determination of the refractive index of highly scattering human tissue by optical coherence tomography*. Optics Letters, 1995. **20**.



9. Knüttel, A. and M. Boehlau-Godau, *Spatially confined and temporally resolved refractive index and scattering evaluation in human skin performed with optical coherence tomography*. J. Biomed. Opt., 2000. **5**(1): p. 83-92.
10. Dave, D.P. and T.E. Milner, Optical low-coherence reflectometer for differential phase measurement. Opt. Lett., 2000. **25**(4): p. 227.
11. Dave, D.P. and T.E. Milner, Phase-sensitive frequency-multiplexed optical low-coherence reflectometry. Opt. Comm., 2001. **193**: p. 39-43.

# **Chapter 5 Optical Coherence Tomography with Adaptive Optics**

## **5.1. Introduction to Adaptive Optics for Human Vision**

The objective of this research is to show feasibility of lateral resolution improvement in OCT imaging by using adaptive optics. Results of this research can directly contribute toward diffraction limited retinal OCT imaging. Higher-resolution retinal imaging potentially offers a powerful adjunct for early diagnosis of various retina-related diseases, better treatment of such diseases, and for human vision research. The conventional retinal imaging technologies, such as direct and indirect biomicroscopy, ultrasonic biomicroscopy, fundus photography, and fluoresce angiography, are unable to achieve this high resolution (e.g. micron-scale). Scanning Laser Ophthalmoscopy (SLO), Scanning Laser Tomography (SLT) and Optical Coherence Tomography (OCT) are new technologies that can possibly achieve high resolution for retinal imaging. However, when these imaging techniques are applied to retinal imaging, the human eye works as an objective lens in the imaging system, and the resolution is limited by the optics of the anterior segment of the eye. Important optical components of the eye include the cornea, the iris and the crystalline lens. The imperfections in these optical components introduce aberrations to the optic of the eye. These aberrations<sup>2</sup>, in combination with the diffraction effect from the iris, limit both the finest image patterns that can be projected on the retina

and the resolution of retinal images that can be obtained with optical imaging instrument. Use of eye-glasses and contact lenses can successfully correct low order aberrations of defocus and astigmatism, but they can not correct high order aberrations, which is necessary to obtain high-resolution retinal imaging or provide high quality vision for patients suffering significant higher order aberrations. The most familiar approach to quantify optical aberrations is the Seidel representation, defined for rotationally symmetric systems<sup>3, 4</sup>. Unfortunately, the Seidel expansion is infrequently used when describing ocular aberrations, since the human eye is not a rotationally symmetric. Taylor polynomials of the Seidel expansion have also been used to describe the eye's aberrations<sup>5</sup>. More recently, Zernike polynomials<sup>6</sup> have been used to represent ocular aberrations due to their desirable mathematical properties for circular pupils<sup>7</sup>. They consist of an orthogonal set of circle polynomials that represent balanced aberrations in the pupil of the optical system. In addition, the Zernike representation can be related to classical Seidel aberrations<sup>8</sup>.

Theoretically, diffraction-limited resolution improves with a larger pupil size, but it has been shown that higher-order aberrations have a significant impact at a larger pupil diameter<sup>2</sup>. For example, in the human eye imaging with a 6 mm diameter pupil typically has worse resolution than imaging with 3 mm pupil. But when the pupil is small, diffraction limits resolution, making it impossible to image retinal structure smaller than about an arcminute onto the retina.

In recent years many have noted a trend in the field of vision sciences to apply adaptive optics and related techniques to compensate for aberrations of the eye. Adaptive

optics was originally developed to compensate for the atmospheric turbulence in astronomical imaging. The technology has been successfully implemented in astronomy for decades to improve the resolution of the astronomical imaging<sup>9, 10</sup>. Dreher et al. first used a deformable mirror in conjunction with the human eye and successfully corrected the astigmatism in one subject's eye. Lian and Williams<sup>11</sup> showed that aberrations up to 8<sup>th</sup> order radial modes negatively impact optical quality when the eye's pupil is large. Liang, Williams and Miller<sup>11</sup> demonstrated that the optical quality of the human eye could be improved in practice by correcting most of the eye's higher order aberrations with an adaptive optics system, consisting of a wavefront sensor coupled via a feedback loop with a 37-channel deformable mirror. Figure 5.1(a) and Figure 5.1(b) illustrate the benefit in resolution and retinal image quality afforded by adaptive optics.

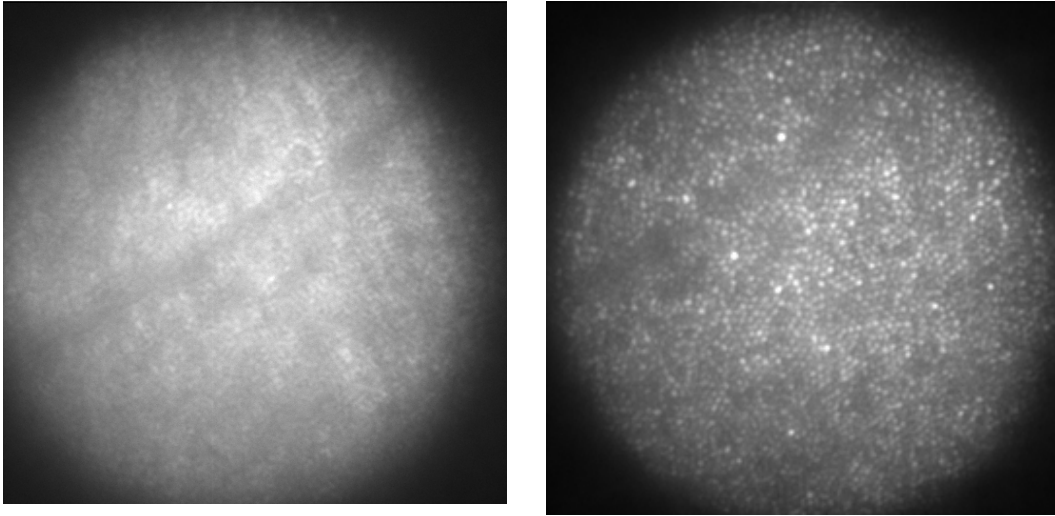


Figure 5.1 Fundus images in the fovea recorded without (a) and with (b) wavefront correction by adaptive optics. Images were recorded by Don Miller, Ph.D. at Indiana University.

## **5.2. Ophthalmic Application of Time-Domain OCT:**

Optical Coherence Tomography was adapted for ophthalmic imaging in the 1990's and is becoming the standard of care for the diagnosis and treatment of macular holes, macular edema, central serous chorioretinopathy, choroidal neovascularization, diabetic retinopathy, and vitreomacular interface abnormalities. The most popular clinical instrument is sold by Humphrey/Zeiss ("OCT 3"). The OCT 3 model scans an 820 nm superluminescent diode laser beam across the retina to generate cross-sectional images (B-scans). At discrete retinal positions within the B-scans (individual A-scan) light backscattered from the retina at a precise location in depth interferes with light from a variable length reference path in a fiber-optic Michelson interferometer. Image processing software produces high-resolution cross-sectional images of the optic nerve and retina. The depth resolution is limited by the bandwidth of the superluminescent diode to approximately 10 microns and the lateral resolution is limited by aberrations in the cornea and crystalline lens to 10 microns.

### **5.3. Description of the Wavefront Correction Device**

The device used to correct the wave-front aberrations in the OCT system, the author utilized a Hamamatsu high-resolution, nonpixelized, optically addressed parallel-aligned nematic liquid crystal spatial light modulator (PAL-SLM), PPM X7550 series.

PPM X7550 is an electrically addressed phase and intensity modulation type spatial light modulator. A PAL-SLM coupled with an electrically addressed LCD through a set of imaging lenses, forms a PAL-SLM module making a PAL-SLM addressable with an electrical signal. PPM X7550 contains a PAL-SLM, LCD, and other imaging optics. The PPM is designed for performing more than  $2\pi$  radians of optical phase modulation when a proper addressing RGB analog signal is applied to the LCD. An addressing image is displayed on the LCD and is transferred to the photoconductive layer a-Si:H of the PAL-SLM by an imaging lenses. The PPM is equipped with a phase/intensity mode selector for selecting phase or intensity modulation mode by rotating the PAL-SLM to an appropriate angle for a desired mode of operation.

#### **5.3.1. Structure of PAL-SLM**

As Figure 5.2 shows, the PAL-SLM device has a sandwich structure consisting of a dielectric mirror, an amorphous silicon (a-Si:H) photoconductive layer and a liquid crystal layer placed between a pair of glass plates on which a transparent electrode is

coated. Write light imaged from the LCD enters the amorphous silicon side and read light, broad band OCT source, is irradiated onto the liquid crystal side.

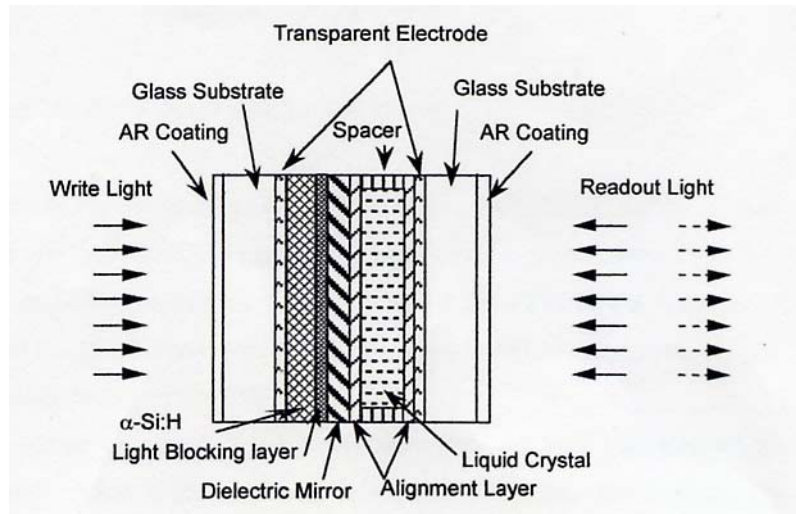


Figure 5.2 Structure of the PAL-SLM. PAL-SLM: parallel-aligned nematic liquid crystal spatial light modulator. The liquid crystal layer at the left side of the dielectric mirror can introduce wave aberration according to the amount of light detected from the  $\alpha$ -Si:H layer.



### 5.3.2. Principle of Phase Modulation of PAL-SLM

As shown in Figure 5.3 (a), a widely used nematic liquid crystal device has the molecules arranged in a twisted state from one side of the liquid crystal layer towards the other side.

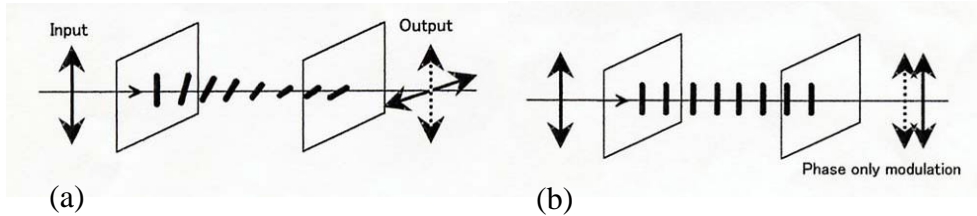


Figure 5.3 Modulation principle (a) twisted nematic (b) parallel aligned nematic

This is known as a twisted type of nematic liquid crystal modulator. This device rotates the plane of polarization of the read light by application of a voltage. This allows the device to be operated as a light intensity modulator through a pair of cross polarizers. This device can also be used to modulate the optical phase. However, this is often accompanied by undesirable variation of the intensity level. As Figure 5.3 (b) shows, the liquid crystal molecules in the PAL-SLM are aligned in such a way that the molecule directions are parallel to each other. When a voltage is applied across the liquid crystal layer, their molecules reach a state in which they are oriented down along the optical axis, applying a phase shift to the read light that is polarized in the direction of the moleculars. On the other hand, light polarized perpendicular to the molecular direction is, in principle, not influenced at all.

### 5.3.3. Write Light Optics Setup

As described earlier, the PAL-SLM needs write light with uniform intensity in order to phase-modulate read-out light according to a phase map image produced and supplied by a computer. Figure 5.4 shows write light optics setup for the PAL-SLM.

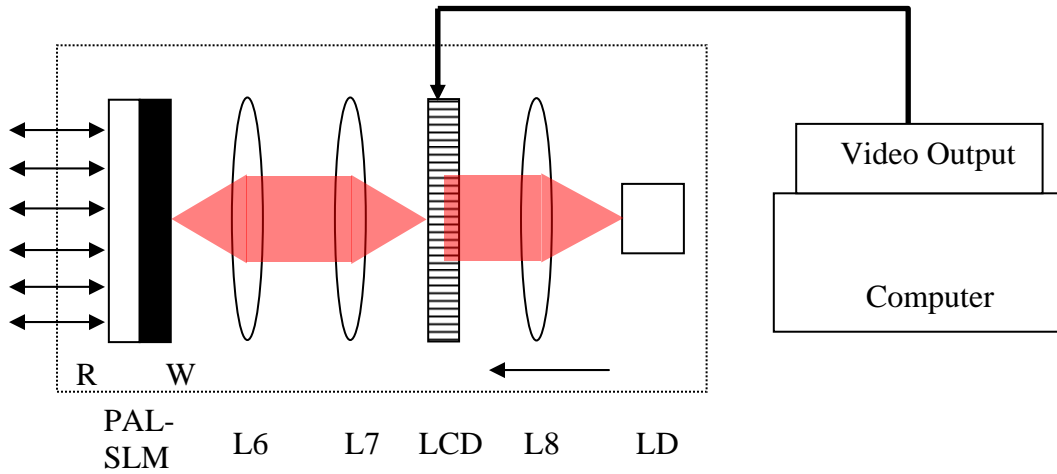


Figure 5.4 Write light optics setup. PAL-SLM: parallel-aligned nematic liquid crystal spatial light modulator. R: reading surface of the PAL-SLM consisted of the array of liquid crystal cell. W: writing surface of the PAL-SLM consisted of the array of  $\alpha$ -Si:H detecting cell. L6 and L7 is a pair of lenses imaging the LCD surface onto the writing surface [W]. LCD: liquid crystal display projecting the image produced by the computer. L8: collimating lens. LD: red laser diode.

The LCD is connected to the video output of a computer, and displays the same screen as the monitor does. PAL-SLM, LCD, and relay lenses (L6 and L7) are assembled in a module. Although Hamamatsu sells a laser module containing a collimating lens

(L8), laser diode come at additional cost of \$7,950, but a custom-made unit was constructed at less than \$100. The specification of this module is that the laser should be red light at a power of 50mW, and collimated beam should be incident on the LCD at a diameter of 20 mm. Uniformity of the beam is a crucial design constraint for error-free phase modulation of read light. Polarization state of light emitted from the laser diode must be parallel to the molecule direction of LCD in order to avoid any unwanted phase modulation. Write light is intensity modulated by the LCD with the projected phase map image and produces an electric potential. When write light is incident on the device, the impedance of the amorphous silicon decreases approximately in proportion to the logarithm of the write light intensity, and the voltage applied across the liquid crystal layer increases according to the intensity of the write light. Consequently, the liquid crystal that modulated read light experiences voltage-dependent birefringence change due to electro-optic modulation.

#### **5.3.4. Calibration of the Wavefront Correction Device (PPM)**

It is important to calibrate the PPM because not only a PAL-SLM has a unique response to write light intensity but also the phase retardation experienced at each pixel of PAL-SLM varies as local write light intensity. When the write light field is not uniform, this calibration is more important. As an input, the PPM takes gray scale video signal and produces phase delay at the read light as output. By calibrating between gray scale input and phase delay output, transfer characteristic for the PPM is necessary to precisely modify the wave-front of read light, which is shown in Figure 5.5. The

horizontal axis shows the input signal level to the PPM and the vertical axis shows the amount of phase modulation. Write light was collimated, centered at 680 nm, and polarized in the vertical direction. Write light power is adjusted to provide a maximum  $2\pi$  radians phase delay.

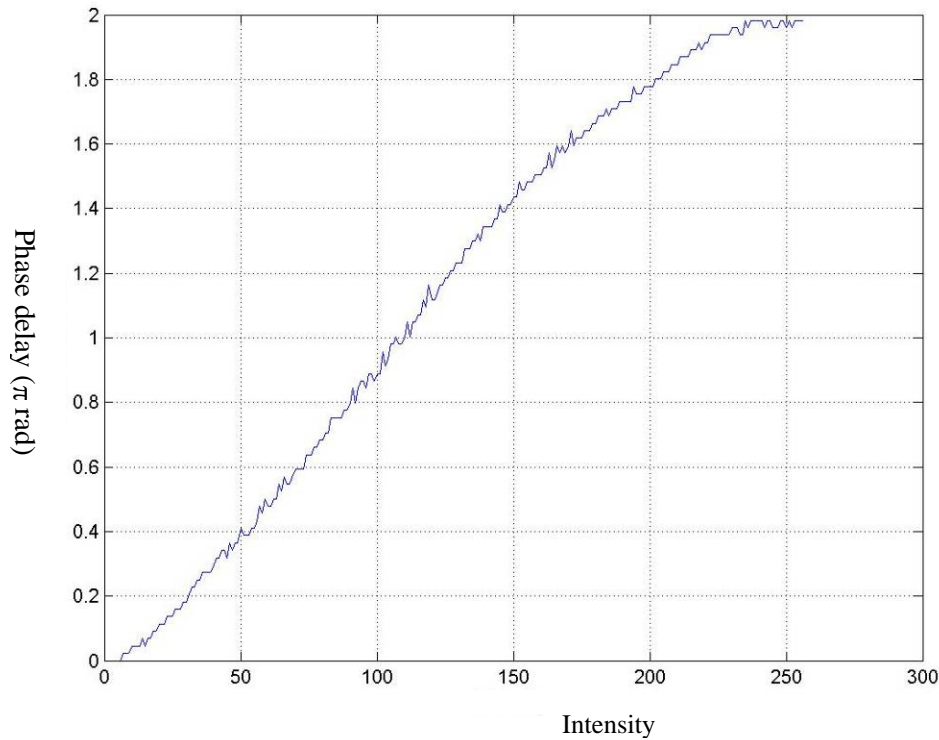


Figure 5.5 Transfer function for the PPM indicating phase delay vs. incident light intensity

## 5.4. Interferometer with Adaptive Optics

In this chapter a simple Michelson interferometer not constructed is adopted to explain the role of parallel OCT in AO-OCT. As shown in Figure 5.7, collimated low

coherence light enters the interferometer. One light group enters sample path where a mirror is placed at the end of the path whereas the other group goes to reference path containing the PPM. When surfaces of both the mirror and the PPM are perfectly perpendicular to the beam direction, flat wavefronts of incident light will be reflected back from the surfaces without modification on the wavefronts. As they recombine at the beam splitter and are detected by the CCD camera, their interference pattern is a single intensity. If the mirror is tilted in  $x$  direction as shown at Figure 5.7, a linear fringe pattern is observed in the interferogram (Figure 5.8). The fringe pattern can be expressed mathematically by,

$$g(x, y) = a(x, y) + b(x, y) \cos(\Phi(x, y))$$

where  $a(x, y)$  and  $b(x, y)$  are the background and contrast functions, and  $\Phi(x, y)$  is the phase function that contains the linear-tilt aberration. In case of linear tilt aberration,  $\Phi(x, y)$  can be found by frequency domain processing (Fourier Transform Method<sup>12</sup>).

The function  $g(x, y)$  can be written again by

$$g(x, y) = a(x, y) + 1/2(\exp(i\Phi(x, y)) + \exp(-i\Phi(x, y)))$$

The fringe pattern is Fourier-transformed with respect to  $x$  which gives

$$I(f_x, y) = A(f_x, y) + C(f_x, y) + C^*(f_x, y)$$

where the upper case letters denote the Fourier spectra and  $f_x$  is the spatial frequency in the  $x$  direction.  $I(f_x, y)$  is shown at Figure 5.6. The vertical axis indicates the intensity of a Fourier-transformed linear fringe pattern,  $I(f_x, y)$ . The horizontal axis is the spatial frequency in the  $x$  direction.  $A(f_x, y)$  is DC and low frequency components of  $I(f_x, y)$ , and

$C(f_x, y)$  and  $C^*(f_x, y)$  are side bands of  $I(f_x, y)$ .  $H(f_x, y)$  is a transfer function of a bandpass filter.

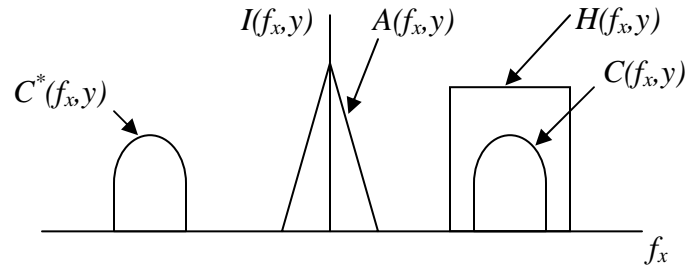


Figure 5.6 Separated Fourier spectra of a linear fringe pattern. Vertical axis indicates the intensity of a Fourier-transformed linear fringe pattern,  $I(f_x, y)$ . Horizontal axis is the spatial frequency in the  $x$  direction.  $A(f_x, y)$  is DC and low frequency components of  $I(f_x, y)$ , and  $C(f_x, y)$  and  $C^*(f_x, y)$  are side bands of  $I(f_x, y)$ .  $H(f_x, y)$  is a transfer function of a bandpass filter.

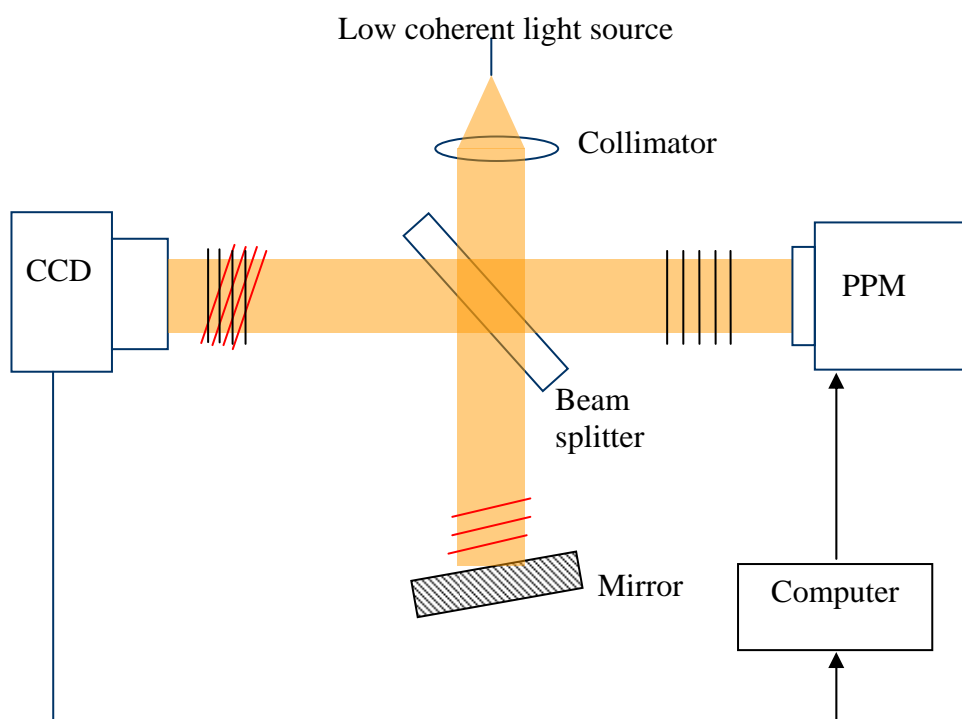


Figure 5.7 Michelson interferometer with PPM adaptive optic

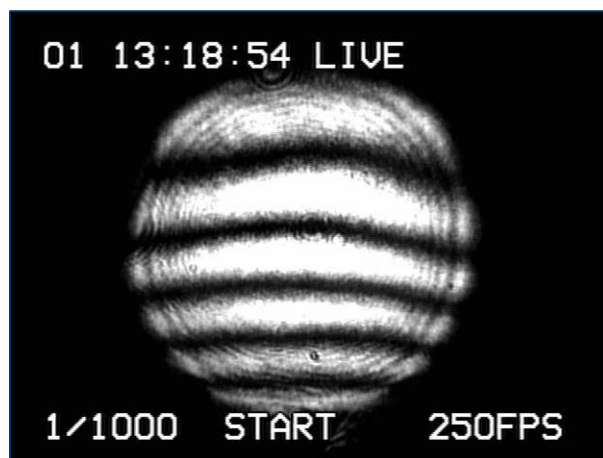


Figure 5.8 Interferogram with linear aberration

By use of a bandpass filter  $[H(f_x, y)]$  in the frequency plane, the unwanted transformed fringe patterns,  $[A(f_x, y), C^*(f_x, y)]$  can be removed and the function  $C(f_x, y)$  can be obtained. Next the inverse Fourier transform of  $C(f_x, y)$  is determined and as a result the complex function,  $1/2 \exp(i\Phi(x, y))$  containing the phase is obtained. The phase function  $[\Phi(x, y)]$  may be then obtained by two equivalent operations. In the first one a complex logarithm of the complex function is calculated;

$$\log(1/2 \exp(i\Phi(x, y))) = \log(1/2) + i\Phi(x, y)$$

In the second method the phase is obtained from finding the arc-tangent;

$$\Phi(x, y) = \tan^{-1} \frac{\text{Im}[1/2 \exp(i\Phi(x, y))]}{\text{Re}[1/2 \exp(i\Phi(x, y))]}$$

where  $Re$  and  $Im$  represent the real and imaginary part of the complex function, respectively. The phase so obtained is unwrapped into the range from  $-\pi$  to  $\pi$ .

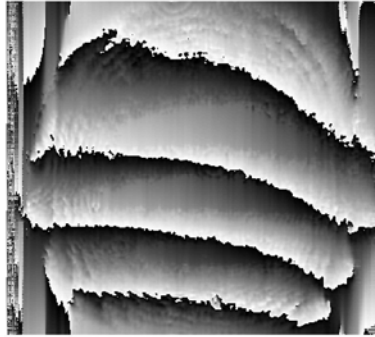


Figure 5.9 Gray-scale phase map of a recorded interferogram of linear-tilted fringe

Figure 5.9 shows a gray-scale phase map of linearly tilted fringes calculated by the Fourier Transform Method, and a brightest level indicates  $2\pi$  radian of phase. Using the



PPM transfer function (Figure 5.5) the phase values ( $0$  to  $2\pi$ ) can be converted to gray intensity levels ( $0$  to  $255$ ), and then inverting of the gray scaled intensified phase map is the compensating phase map (Figure 5.10) to be provided to the PPM.

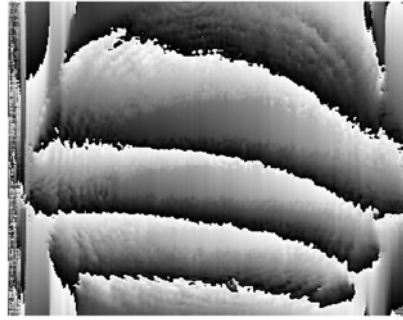


Figure 5.10 Phase map to compensate for Figure 5.9

The PPM produces a phase delay in each pixel according to the compensating phase map's intensity level of the pixel. As a result the reflected wavefront from the PPM acquires a compensating linear tilt. When both wavefronts, one from the mirror and the other compensated by the PPM, combine and produce interference fringe, CCD camera displays only one intensity level over the field.

To illustrate, Figure 5.11 (a) shows a background-subtracted interferogram of a linearly tilted fringe. The gray-scale compensating phase map was applied to the left half of the LCD of the PPM; therefore, one side of the reflected wavefront from the PPM is linearly tilted while the other side remains perpendicular to the propagation direction. When they combine and interfere, only half of the field produces a line-patterned fringe but the left side display has one intensity level as shown at Figure 5.11 (b).

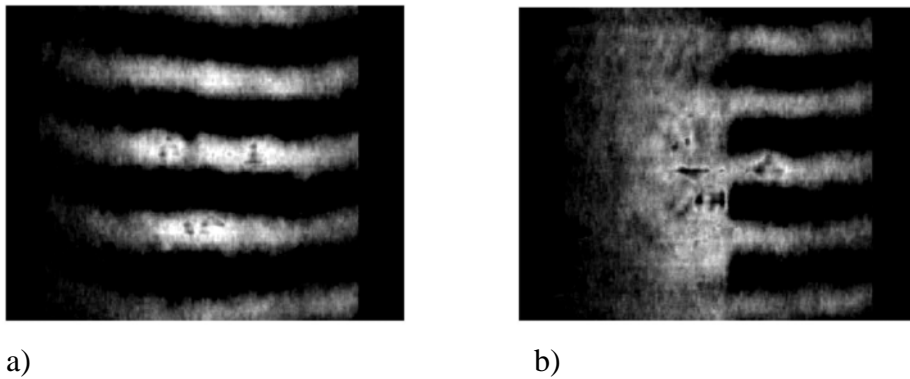


Figure 5.11 Correction of linear tilt aberration using Fourier Transform Method. (a) Interferogram of linearly tilted aberration (b) compensated interferogram- the compensating phase map is applied to the left half of the field.

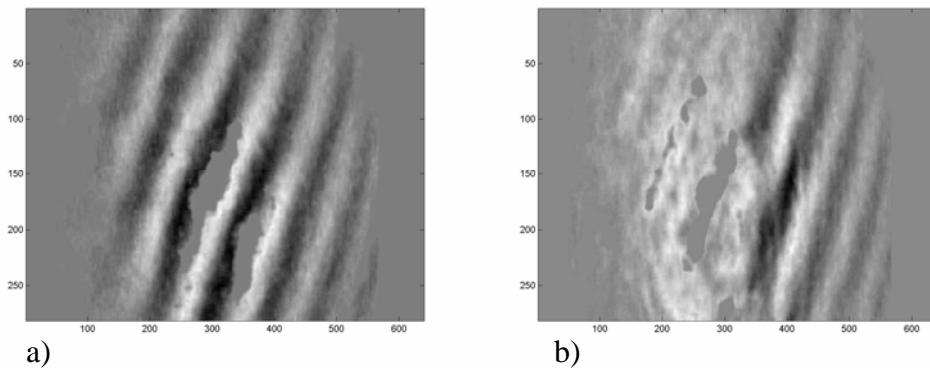


Figure 5.12 Correction of diagonal tilt aberration using Fourier Transform Method (a) interferogram of the diagonal tilt aberration (b) compensated interferogram- the compensating phase map is applied to the left half of the field.

Next tested aberration pattern is diagonally tilted producing both  $x$ - and  $y$ - spatial frequencies. After following the same procedure to calculate phase maps with the linear-

tilt correction, the filter,  $H(f_x f_y)$ , is redesigned to cover all  $C(f_x f_y)$  components. Figure 5.12(a) shows the diagonally tilted interferogram, and Figure 5.12(b) is the aberration compensated interferogram. Again only the compensation is performed on the left half of the screen.

This Fourier transform method has been tried to circular or higher order aberration, but the two-dimensional Hilbert transform leads undesirable sudden phase inversions (Figure 5.14). An alternative approach to compute the compensating phase map will be addressed in Chapter 5.6. in detail.

## 5.5. OCT with Adaptive Optics Setup

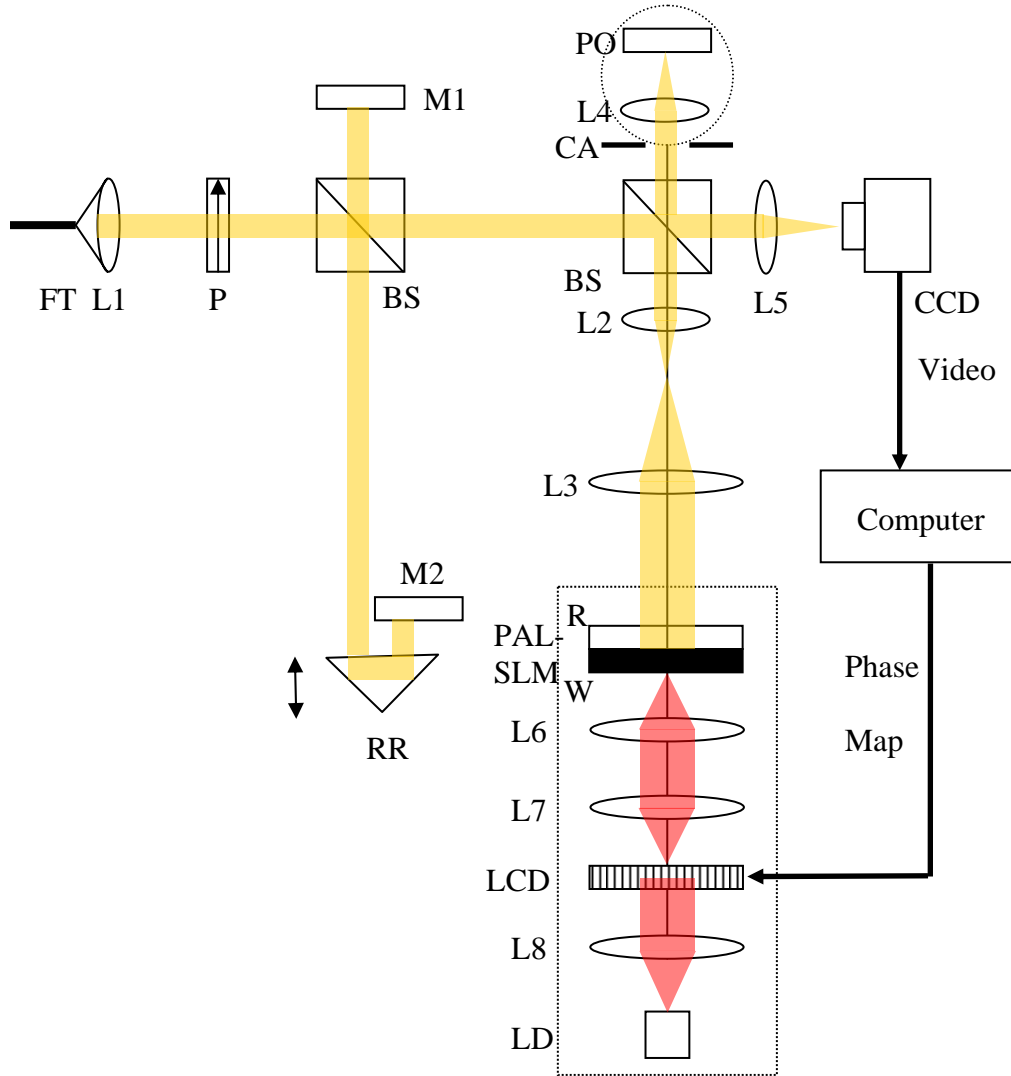


Figure 5.13 Diagram of Parallel OCT system with adaptive optics. FT: optical fiber tip, L#: lenses, M#: mirrors BS: beam splitter, P: polarizer, RR: retroreflector, CA: circular aperture, PO: planar object, CCD: digital CCD camera, LD: laser diode, LCD: liquid crystal device

A broadband light source is delivered through a single-mode optical fiber and launched into the system by a collimating lens (L1). Beam diameter is set to be 1 mm. Because the parallel aligned spatial light modulator (PAL-SLM) has strong polarization dependence such that only the component of polarization of incident light along the liquid crystal molecule directors is phase modulated when reflected, a polarizer (P) removes all other polarization states of light except the vertical state that is aligned parallel to the PAL-SLM. A beam splitter (BS1) divides light into the sample and reference paths. Light transmitting through penetrating BS1 is defined as sample path light. When light enters the reference path, it is path-length modulated by a retroreflector (RR) mounted on a voice coil. The voice coil is driven by a function generator which provides a sinusoidal wave with 10 V peak to peak. The voltage can be modified to vary depth of scan. After passing the RR, reference path light reflects back from a mirror (M2) and returns back to BS1. Now by penetrating the BS1 the reference path light loses half of its optical power and reflects back from mirror (M1) and recombines with sample path light. No interference is observed at this position because path length difference between reference and sample paths is longer than the coherence length of the source. Note that a quarter of the reference path light can recombine with sample path light, which can be minimized by using a polarization-sensitive beam splitter instead of using BS1. The recombined light paths are separated by the second beam splitter (BS2). Half of light transmitting through BS2 enters, so called, the detection path, and is detected by a charge-coupled device (CCD) camera. Only one-eighth of the reference and sample path light can be detected by the CCD camera.

Sample path light reflected by BS2 is expanded by 10 times using lenses (L2 and L3) providing a 10 mm beam diameter incident on the adaptive optics (PAL-SLM) becomes 10 mm. Because the size of the liquid crystal cell of the adaptive optics is fixed, magnifying the beam size can provide finer control over the optical field. Sample path light illuminates the reflective liquid crystal layer of the PAL-SLM placed at the focal plane of the lens L3 and experiences wave-front modification. Detailed process of the wave-front modification will be explained in chapter 5.6. The modified sample path light returns back to BS2 and illuminates sample. The liquid crystal layer is placed at a conjugate plane of a pupil plane (CA) by the relay lens pair (L2 and L3), so the adaptive optics compensates the wavefront reflected back from the sample at this plane. A circular aperture (CA), a lens (L4), and a plain object (PO) make a model eye. Incoming light is focused by L4 at the PO which can be a scattering or specular reflector. PO located at the back focal plane of L4 is uniformly illuminated by incoming light. The reflected light from PO is imaged onto the CCD camera by a lens pair (L4, L5). Interference fringe forms at the detection plane of the CCD camera when the path length difference between the sample and reference paths is matched. The image of PO captured by the CCD camera is generally blurred by the effect of wavefront aberration of L4. However, the blurred image may be corrected when the phase distribution across the PAL-SLM cancels the wavefront aberration due to L4, so that the PAL-SLM behaves as a wavefront corrector.

## 5.6. Phase-map Measurement using Parallel OCT

Estimation of the local phase is an important step in applying Adaptive Optics to correct image aberrations. To perform aberration compensation, most existing systems utilize Shack-Hartmann wavefront sensors to measure wavefront deformations caused by optics in the eye. Main components of Shack-Hartmann wavefront sensors are a micro-lenslet array and CCD camera. Each micro-lens is associated with a group of CCD pixels. If a plane wave is incident on the sensor, each focal spot is formed on the optical axis of the pixel group for the micro-lens. Wavefront aberrations can be estimated by the shift of focal spot in both the  $x$ - and  $y$ - directions. In order to reduce speckle noise and temporal fluctuations of the eye, raster scanning methods have been adopted to the wavefront sensor<sup>13, 14</sup>.

I present an alternative method, wavefront measurement using an interferometer. For almost two decades one of the most successful methods of demodulating fringe patterns was based on the Fourier transform method using the one-dimensional Hilbert transform<sup>12</sup>, which also provides phase information. In practical problems either the analytic signal itself is evaluated, or the analytic signal of a band-pass filtered version of the input signal is considered. In the previous section 5.4. , use of a band-pass filtered version was explained. Analysis of two-dimensional fringe patterns requires more sophisticated filters, called 2-D Gabor filters which are now widely used in image processing. These filters are orientation selective and allow the estimation of the local phase provided that the local orientation is known or has been estimated in a previous processing step. However, phase calculation using this method produces unwanted

sudden phase inversions in a two-dimensional interferogram as shown Figure 5.14. At the positions where the local orientation flips from  $-\pi/2$  to  $\pi/2$  the phase is inverted:  $\phi(x) \rightarrow -\phi(x)$ . This effect is called sudden phase inversion- not to be confused with a  $2\pi$  wrap around, which is typical for phase images.

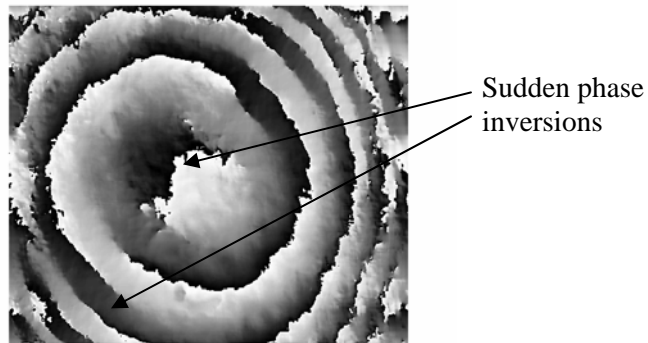


Figure 5.14 Phase map of cylindrical aberration showing sudden phase inversions



Recently a method of fringe analysis based on an isotropic two-dimensional Hilbert transform has been proposed<sup>15</sup>. This method uses Moire interferograms with the Riesz transform to obtain smooth phase maps without sudden phase inversions.

Another method to measure two-dimensional phase map is to use phase-shifting interferometry<sup>16</sup> (PSI). In this so-called phase-stepping technique, the phase is stepped by a known amount between each intensity measurement. Usually this stepping is done by attaching a mirror on a piezoelectric transducer (PZT) in the reference path.

Although these three methods (Shack-Hartmann wavefront sensor, isotropic two-dimensional Hilbert transform, and PSI) have shown promising result in measuring phase map of wavefront, I have developed an easy and simple method to construct a phase map using parallel OCT.

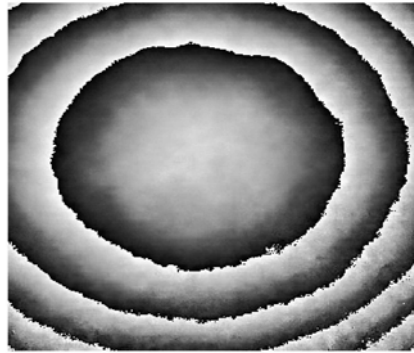


Figure 5.15 Intensity image of phase map of cylindrical aberration

By using the AO-OCT system (Figure 5.16), a depth-resolved interferogram can be recorded by the CCD camera, which produces a three-dimensional data cube. Instead of finding the analytic signal in the spatial domain (the Fourier transform method), our

method picks a pixel and takes all data points along the time axis which can be expressed by

$$I_{x,y}(t) = I_r + I_s + |S(t)| \cos(2\pi\nu_0 t + \phi(x, y, t))$$

where  $I_{x,y}(t)$  is fringe intensity along time axis at given position  $(x, y)$ ,  $I_r$  and  $I_s$  are DC intensities from reference and sample paths, respectively, and  $S(t)$  is the complex temporal-coherence function modulated by the carrier frequency  $\nu_0$ .

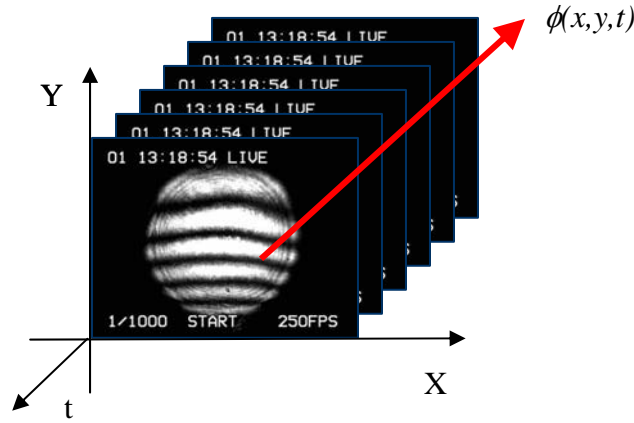


Figure 5.16 Three-dimensional fringe data cube

After suppressing DC and low frequency components by a high pass filter, only the complex temporal-coherence function remains. Hilbert transform of the function provides imaginary part of the function, and arc-tangent between real and imaginary parts of the function finally give phase information of the function. A three-dimensional phase map can be constructed by applying this method over all  $x$  and  $y$  coordinates. The phase values distributed from  $-\pi$  to  $\pi$  need to be converted to intensity values ranged from 0 to

255 by using the PPM transfer function (Figure 5.5). After converting the three-dimensional phase map into an intensity map, one frame at any given  $t$  is selected from the three-dimensional intensity map and inverted; therefore, intensity level 0 becomes 255 and vice versa. This inverted intensity image (Figure 5.15) becomes a compensating phase map when the image is applied back to the CCD of the PPM.

### 5.7. Wavefront Correction

After the compensating phase map is generated, the image is displayed on the operating computer's screen that is mapped on the LCD of the PPM. In order to avoid erroneous mappings, the size of the computer screen needs to be matched with that of the LCD of the PPM (640\*480), otherwise an additional mapping sequence is necessary.

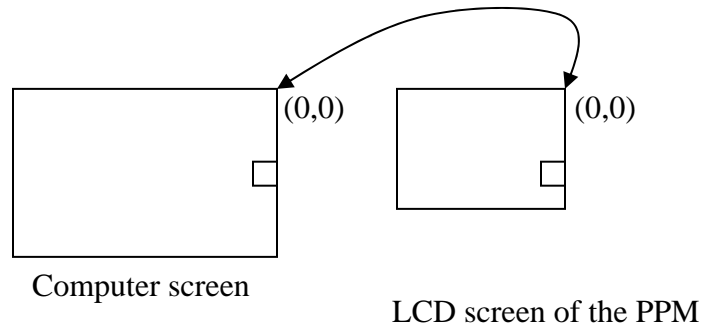


Figure 5.17 Mapping between computer screen and the LCD of the PPM

Phase map of an interferogram containing cylindrical aberration due to the sample optics, Figure 5.18 a), shows a few circular rings indicating  $2\pi$  phase wrapping. The sample is a reflective surface that can produce interferograms with high contrast and is

convenient to confirm validity of the phase measurement and correction method. When imaging biological tissues, the surface is conventionally considered a scattering media that contains a significant amount of speckle. Because speckle reduces the contrast in interferograms reduction is necessary. Figure 5.18 b) displays a single cross-sectional phase profile of the arrowed line in Figure 5.18 a). No average over frames or over field is performed. Phase fluctuations at left corner in the profile is because intensity of the interference signal is smaller than that of the detector noise. Parabolic phase variation in the profile indicates the cylindrical aberration in the sample light. The phase profile is unwrapped by  $2\pi$  radians using the “unwrap()” Matlab function. Maximum phase difference in the profile is approximately 18 radians and r.m.s of the phase variation is about 4.1 radians. When a compensating phase map processed by the method described earlier is projected on the CCD of the PPM, the amount of light penetrating each pixel is modulated according to the intensity of the pixel. The wavefront of reading light is reflected from the reading surface [R] of the PAL-SLM and experiences a compensatory aberration or correction including sample optics. An aberration-compensated phase map recorded by the parallel OCT with adaptive optics is shown at Figure 5.19 a) and contains no rings, which indicates phase variation is below  $2\pi$  radians. A single cross-sectional phase profile at the arrowed line is shown at Figure 5.19 b) confirms low phase fluctuation. No average over frames or over field is performed. Phase values at positions less than 50 and greater than 250 of  $x$  scale are meaningless because they are phase noise. The causes of phase noise are either low interference signal or out side the illuminating

area. The amount of phase fluctuation over the illuminating area is 0.8 r.m.s. radians which is much smaller than that of the uncompensated phase map.

To verify the phase measurement and correction method in a scattering media, a collagen film is used as a sample and cylindrical aberration is introduced with a low quality lens that resembles the crystalline lens in the eye. Following the procedure with reflective surface imaging, the collagen film and a reference mirror are placed at the end of the sample path and the reference path respectively. Depth scanning is performed by driving the voice coil with a sinusoidal signal, and interferograms are recorded using a CCD camera in the detection path. Phase map is calculated from the interferograms using the method described in Chapter 5.6. Figure 5.20 a) displays a phase map of a frame of the interferograms containing mainly cylindrical aberration. Because the backscattered light from the sample is weak and contains large amount of speckle, contrast in the interferograms is low. The phase map displays discontinuous phase wraps indicating surface flatness of the sample is not uniform and a potential source of speckle. Regions of phase wrapping are circularly distributed in the phase map, which may indicate overall phase variation in the field and may follow the cylindrical aberration. A cross-sectional phase profile, Figure 5.20 b), is calculated by averaging 20 lines near the arrowed line in Figure 5.20 a) in order to reduce the effect of the speckle. This averaged profile, Figure 5.20 b), shows less variation over position compared to the single phase profile of a reflective sample, Figure 5.18 b), but has huge bumps at  $x = 100$  and  $x = 150$ , which may indicate a morphological feature of the sample surface. This surface variation can be one factors in measuring wavefront of the light returning from a sample because the phase

variation can be produced not only by aberrations in the optics, but also the morphological shape of the sample surface. Horizontal lines in Figure 5.20 a) may be considered as instrumental error because the CCD used in this experiment uses progressive scan method. During depth scanning in parallel OCT, each pixel records an interferogram that is offset in time. This artifact can be removed by using a flash scanning type CCD camera that reads all the pixels at the same time.

A compensating phase map of Figure 5.20 a) is projected onto the LCD screen of the PPM and interferograms between the sample and the reference mirror are recorded again. Phase map of this aberration corrected interferograms is shown at Figure 5.21 a). It can be observed that the number of phase wrapping patches is reduced in the phase map and phase variation over the field is relatively low in comparison to uncorrected phase map in Figure 5.20 a). However the phase map shows a couple of phase wrapping at the center of the field, and also diagonal dark lines indicated by dotted arrows. These lines might be due to the spatial distribution of collagen in the film. The r.m.s value of the phase variation is reduced to 2.44 whereas it is 3.46 before aberration compensation.

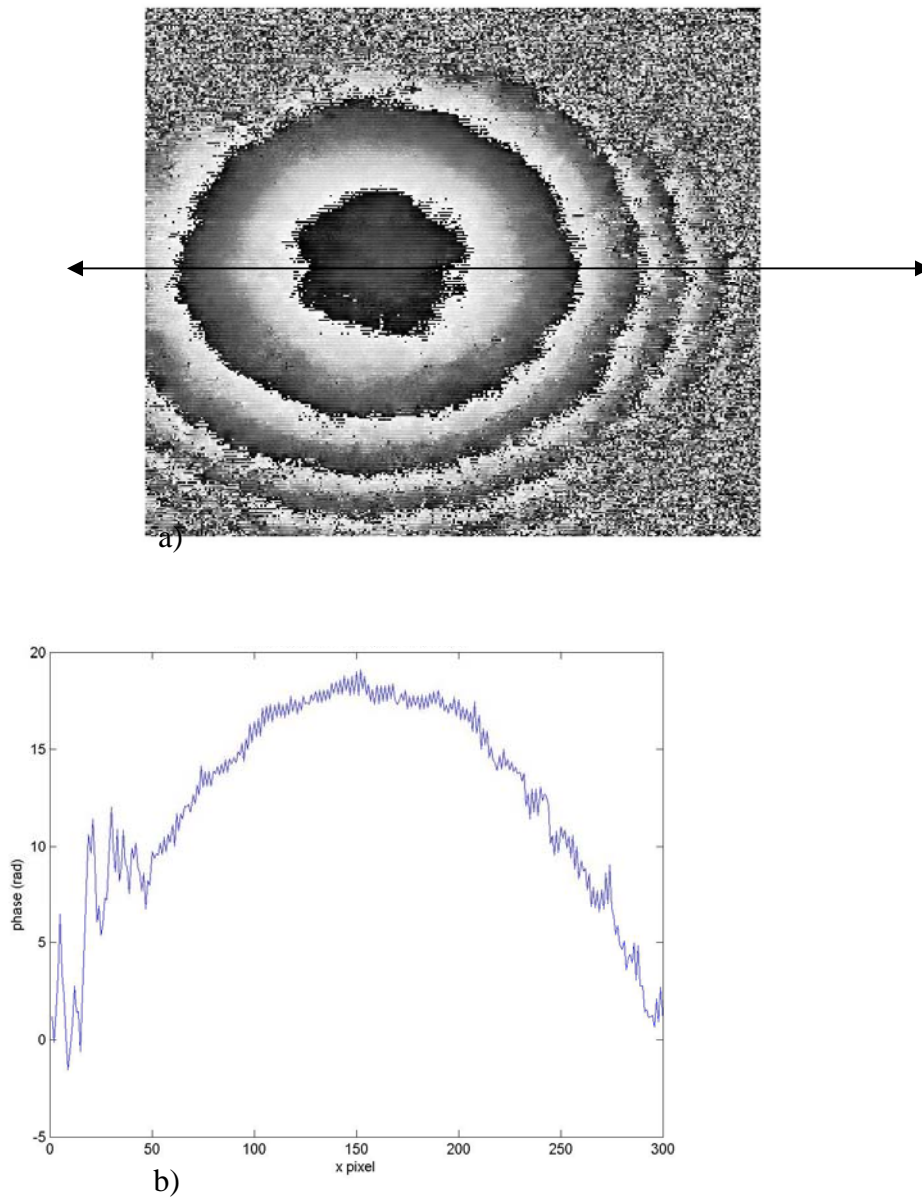
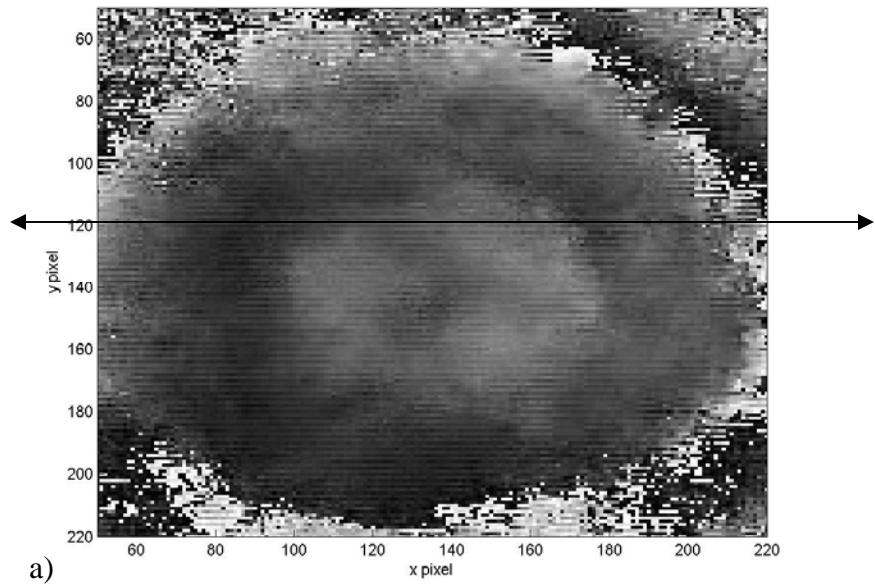
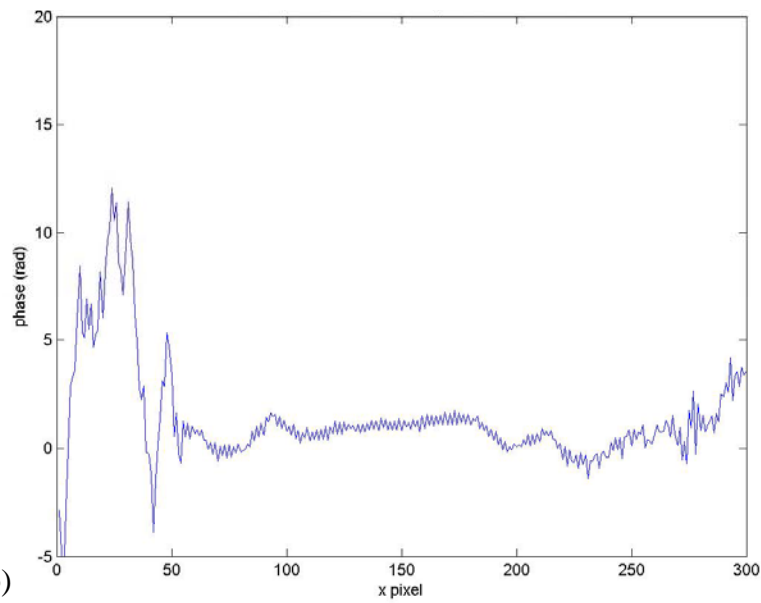


Figure 5.18 a) Phase map of an interferogram of a reflective surface containing cylindrical aberration due to the sample optics. b) cross-sectional phase profile of the cylindrical aberration.



a)



b)

Figure 5.19 a) Phase map of the aberration-corrected interferogram of a reflective surface by Parallel OCT with adaptive optics. b) cross-sectional phase profile of cylindrical aberration.



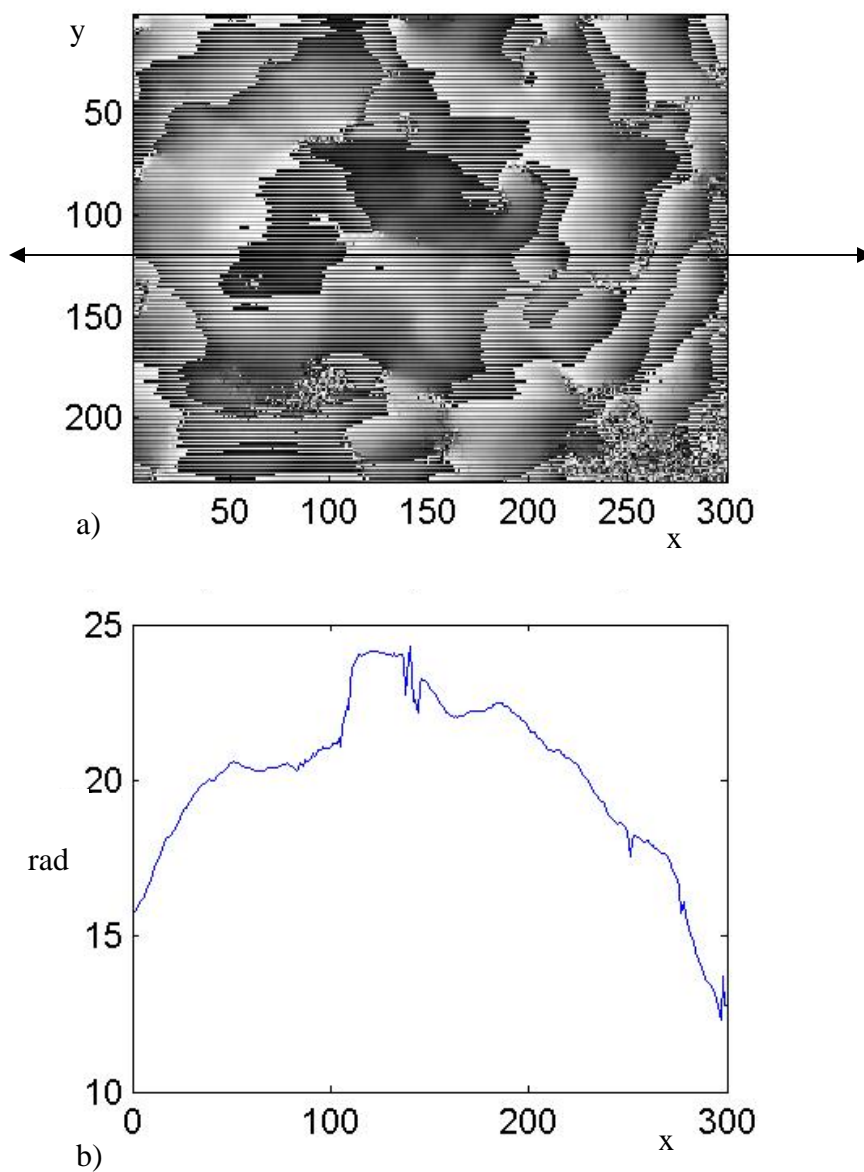


Figure 5.20 a) Phase map of an interferogram of a scattering surface with cylindrical aberration. b) Cross-sectional phase profile averaged over 20 lines near the arrowed line in a).

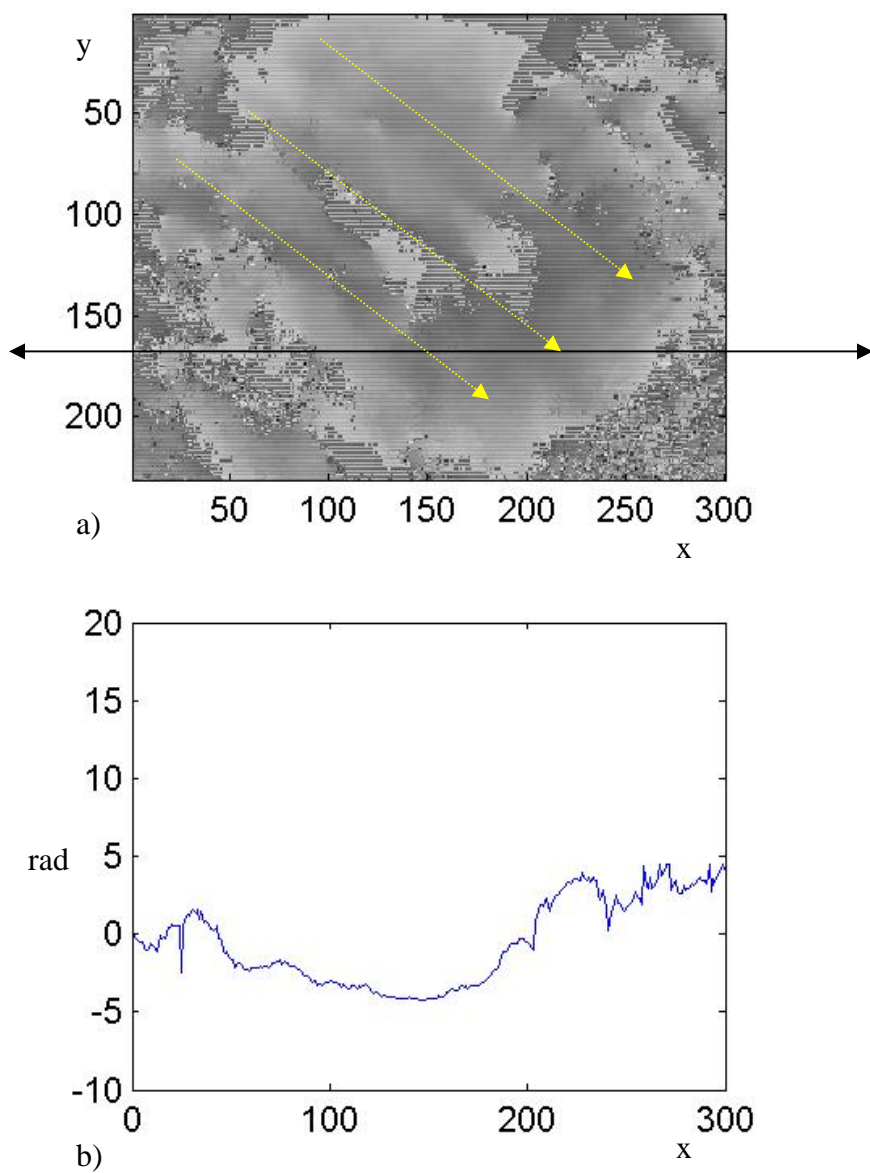


Figure 5.21 a) Aberration corrected phase map of an interferogram of scattering surface  
b) cross-sectional phase profile averaged over 20 lines near the arrowed line in a)

The beam profile at the sample plane is observed with a CCD camera to confirm lateral resolution improvement after correcting aberrations with adaptive optics. Figure 5.22 a) and b) display the profile without and with adaptive optics, respectively. In Figure 5.22 a) the beam profile is blurred due to cylindrical aberration, but after the aberration corrected by the AO, the profile becomes smaller and more focused, Figure 5.22 b). However the intensity distribution at the beam waist, Figure 5.22 b) does not follow Gaussian shape owing to imperfection of the correction suggesting the beam is not diffraction limited.

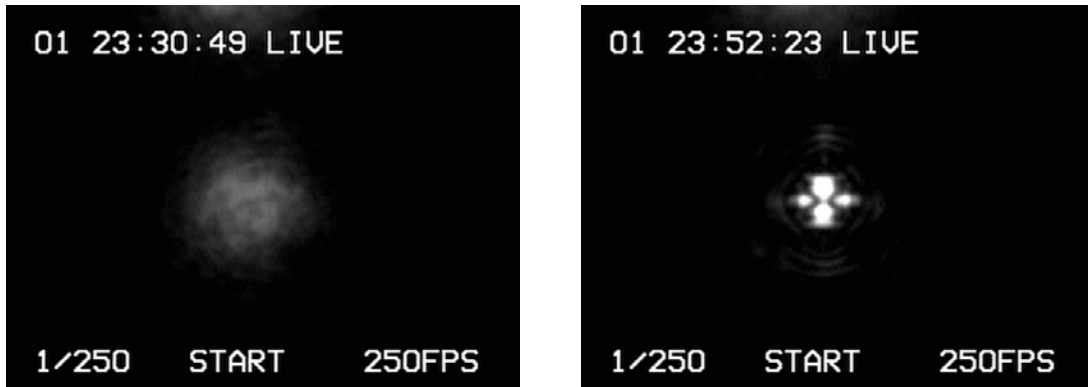


Figure 5.22 Images of sample beams (a) without adaptive optics and (b) with adaptive optics

## **5.8. Lateral Resolution Improvement in Raster Scanning OCT with Adaptive Optics**

### **5.8.1. Experimental Setup**

Raster scanning OCT imaging with adaptive optics was performed on two different sample types to confirm improvement in lateral resolution. One sample consisted of a metal grid that had several different metal lines on a glass substrate. Lines separated by 50  $\mu\text{m}$  were imaged. The other samples were scattering and included fresh onion tissue and a metal grid covered with turbid milt solution.

Figure 5.23 shows configuration of the sample stage. The metal grid was placed on a motorized stage that provided lateral scanning. The densities of the imaged metal lines were 15 lines per millimeter and 20 lines per millimeter. The 20 lines/mm grid had 25  $\mu\text{m}$  features that totally backscattered light and adjacent area was glass. Separation between the metal lines was 50  $\mu\text{m}$ . Features in 15 lines/mm were separated by 66  $\mu\text{m}$ .

The optical setup of the raster scanning OCT with adaptive optics is shown at Figure 5.13. For OCT imaging, the raster scanning method was used to increase signal to noise ratio by using a photo-receiver at the detection path. The path included a flip mirror and an 8 mm diameter Si large-area photo-receiver (Newfocus<sup>TM</sup>, model 2031). When the flip mirror is folded down, the light passing through L5 was focused on the CCD camera. Once the CCD camera acquires the phase map containing aberration information of the sample optics, the flip mirror was folded up to divert the light into the large area photo-receiver, and a lateral scan was performed.

A low quality lens was used as an objective [L4] to introduce aberration. Focal length of the lens was about 18 mm and the beam diameter entering the lens was about 2 mm, which yielded a 9.7  $\mu\text{m}$  of calculated diffraction limited beam spot size at the sample surface.

A mode-locked Ti:Sapphire laser was coupled into a single mode optical fiber and launched into the system through L1 with power of 300 mW. Light with 37mW power entered the sample path including CA, L4, and PO. A variable neutral density filter was inserted between M1 and M2, and was adjusted to have comparable sample and reference powers at the detection plane.

To image the grid through scattering media, a cuvette with 300  $\mu\text{m}$  depth was covered with the metal grid, and filled with solution of 1  $\mu\text{m}$  size micro-beads. Accurate density of the solution was not traced, but solutions with two different arbitrary densities were used. Because light enters the bottom of the cuvette to the metal grid, scattering occurs before reaching the metal grid. Figure 5.24 shows the side view of the sample configuration containing scattering media.

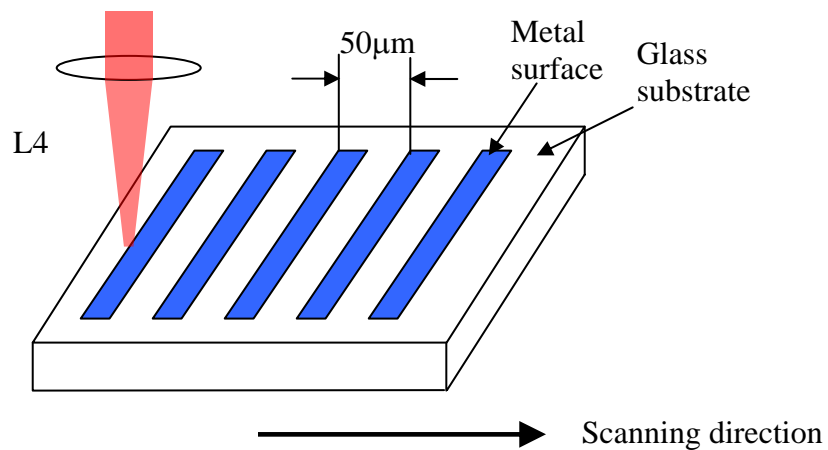


Figure 5.23 Configuration of sample stage with a metal grid

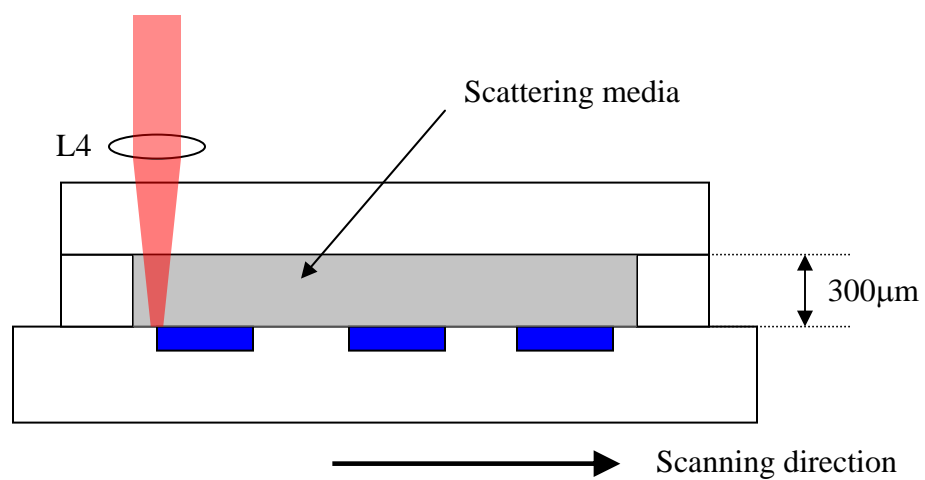


Figure 5.24 Side view of the sample stage with a metal grid covered with scattering media. Micro beads ( $1\text{ }\mu\text{m}$  diameter) and milk are used as the scattering media.

A motorized stage holding the metal grid was synchronized with the image acquisition software. The stage was moved by 5  $\mu\text{m}$  and 30 A-scans were recorded. The retro-reflector [RR] mounted on a voice coil was continuously driven by a function generator with sinusoidal wave. Scan depth was adjusted at each sample to observe the sample clearly by controlling the peak-to-peak voltage of the sinusoidal wave. Actual scan depth is marked on each presented image. The sinusoidal signal was also connected to an input port of the acquisition board. A acquisition software written by the author used the input port as an analog trigger signal. The trigger level was set to record an A-scan during the linear region of the sinusoidal signal. Once the program acknowledges a trigger event, a fixed number of data points are acquired from the detector output. After incoherent demodulation the program displayed the recorded image on the computer screen. The acquisition program can allow the user to enter the number of data point to acquire, sampling rate, low/high pass filter's cut-off frequencies, and lateral scanning step size in micrometers. The acquisition program allows storing the acquired data into a text-formatted file.

### **5.8.2. Results**

Figure 5.25 and Figure 5.26 show the OCT images of metal lines considered as reflective samples. The line resolution is 20 lines per millimeter, so the line separation is 50  $\mu\text{m}$ . The motorized stage was moved by step size of 5  $\mu\text{m}$ , and 30 A-scans were recorded. All the images presented here have linearly scaled intensities.

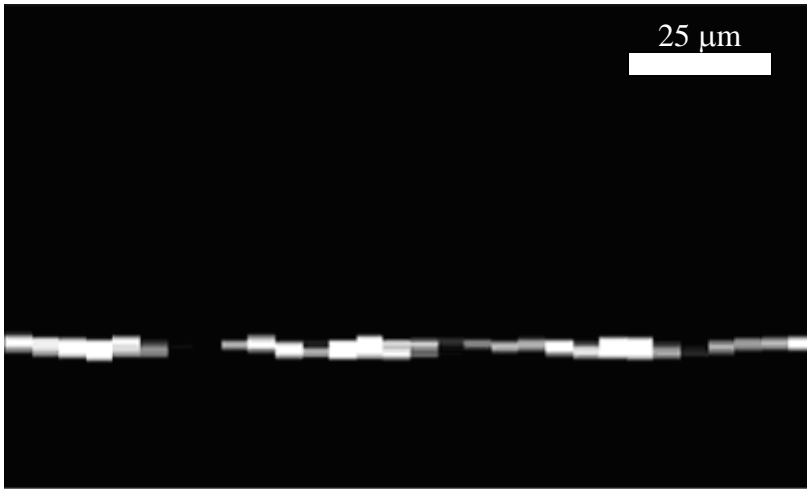


Figure 5.25 OCT image of metal lines separated by 50 μm without aberration correction.

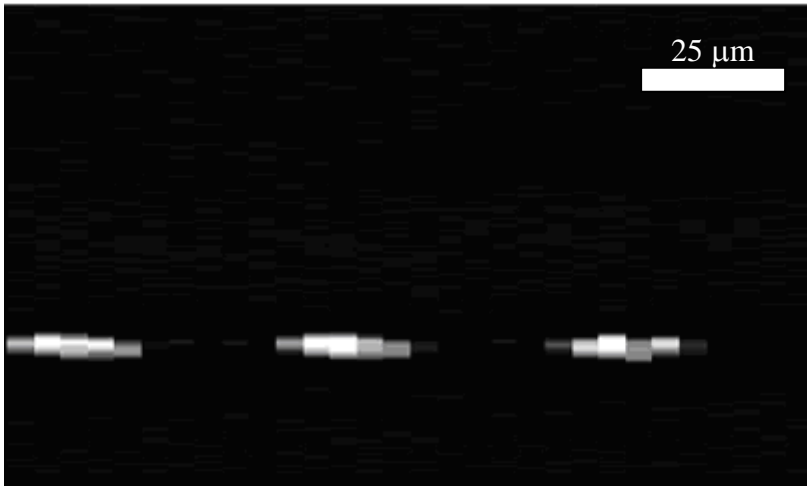


Figure 5.26 OCT image on metal lines separated by 50 μm with aberration correction

Lateral scan range was 150 μm. The sampling rate was 2M samples per second, and each A-scan recorded 200,000 samples. The cut-off frequencies of the high pass filter and low



pass filter were 27 KHz and 24 KHz respectively. Depth scanning range was about 200  $\mu\text{m}$ . First, the metal lines were imaged without applying the adaptive optics (Figure 5.25). The flip mirror was then folded down to direct light on to the CCD camera to image the interferograms. After calculating the compensating phase map from the interferograms, the computer projected the compensating map onto the LCD of the PPM. The same area of the metal lines was imaged again with operating the adaptive optics (AO) correction. The image shown at Figure 5.26 displays three clear metal surfaces whereas the image without AO (Figure 5.25) has blurred lines because the aberration of light increased the beam diameter at the sample surface as shown at Figure 5.22. The fact that clear boundary is observed between metal lines indicates (Figure 5.26) the beam size of the aberration corrected light is smaller than the resolution between lines [50  $\mu\text{m}$ ]. The longitude bars in Figure 5.25 and Figure 5.26 indicate length of 25  $\mu\text{m}$  in lateral direction in the images.

Next a scattering media was placed above the metal lines. Figure 5.27 shows the OCT image of metal lines covered by solution of micro-beads without correction using adaptive optics. The solution consisted of 1  $\mu\text{m}$  polystyrene microspheres diluted in deionized water. The thickness of the solution chamber was 300  $\mu\text{m}$ . The first bright line from the top of the image is the boundary between the cover glass and the solution chamber. Resolution of the metal lines was the same as that of the previous target. The bright line at the bottom of the image represents blurred metal lines that ideally should show as three distinct segments.

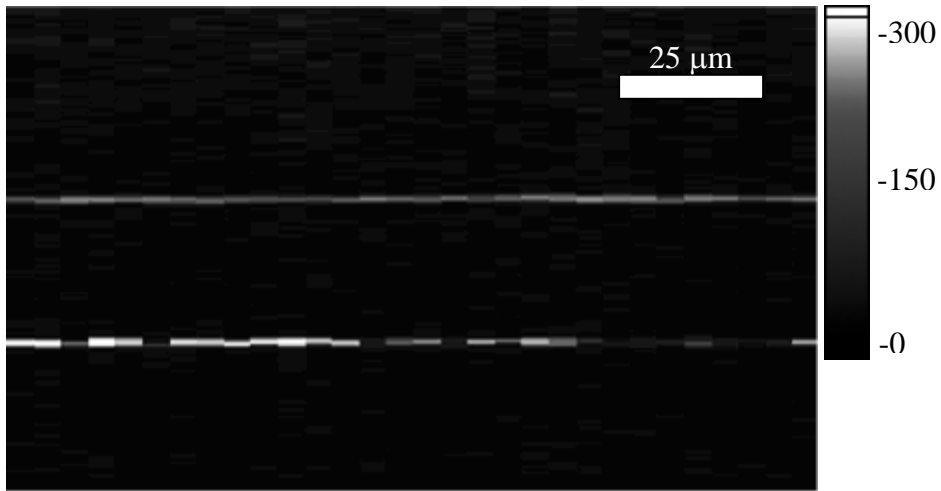


Figure 5.27 OCT image of metal lines through micro-bead solution without aberration correction

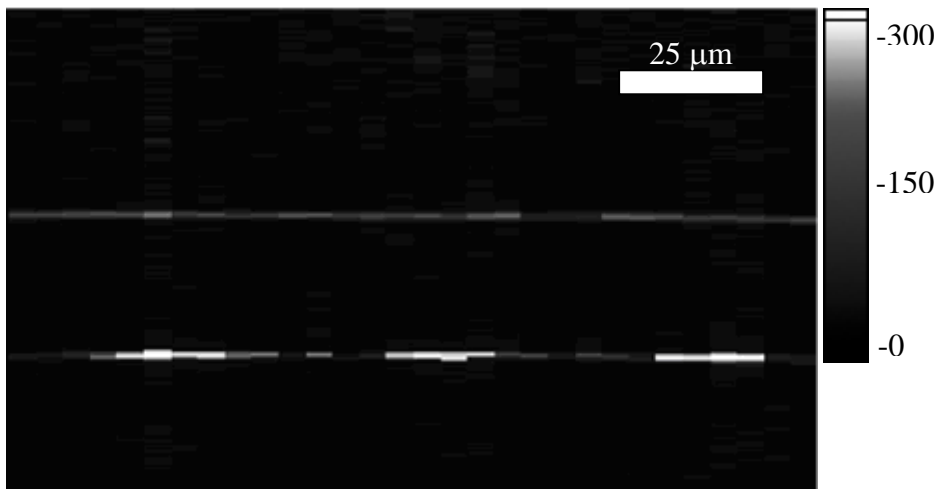


Figure 5.28 OCT image of metal lines through micro-bead solution with aberration correction

Figure 5.28 shows an OCT image of the metal lines through the solution of micro-beads after correction with adaptive optics. The image displays three large segments

meaning that the beam diameter of the light is much smaller than the resolution of the lines.

The density of the micro-beads in the solution was increased to make a stronger scattering media. Figure 5.29 displays an OCT image of the metal lines through a denser solution of micro-beads. The upper bright line represents the boundary between the cover glass and the solution. As micro-bead density increased, the brightness and thickness of the boundary was increased possibly due to the increased difference of refractive index between two media or because microspheres attached on the glass surface that could be observed by the author.

Figure 5.30 displays the OCT image of the metal lines with adaptive optics control on, and shows distinct three segments in the bottom line indicating the aberration was successfully corrected.

A sample was then prepared by filling the solution chamber with diluted milk, and Figure 5.31 shows the OCT image of the metal lines without controlling the adaptive optics. The first boundary between the cover glass and the solution chamber was not able to be observed in the image possibly because either the refractive index of the milk solution was too high, so the optical boundary was out of depth scanning range or the reflectance at the surface was too small to observe in linear scaled intensity image. Figure 5.32 shows the OCT image of the metal lines with adaptive optics on, and displays three better resolved segments of the line but is not as clear as the case of the micro-beads solution.

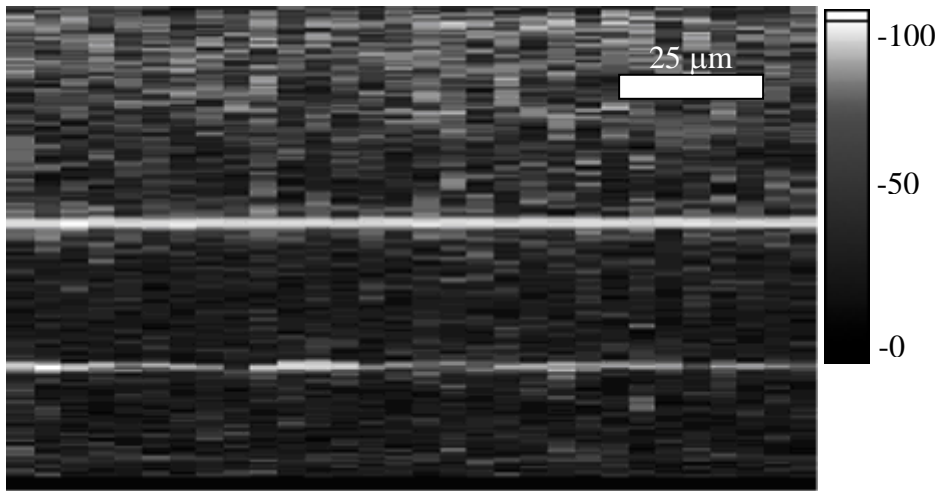


Figure 5.29 OCT image of metal grid through denser solution of micro-beads without aberration correction

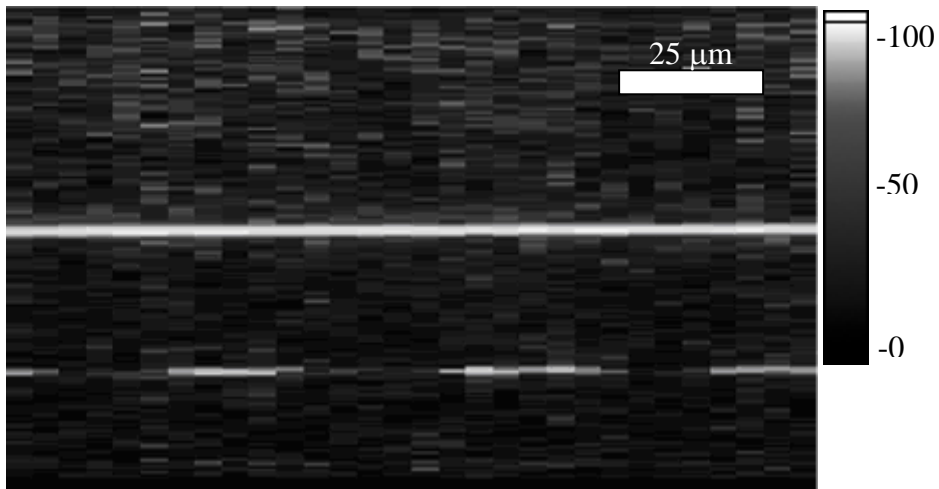


Figure 5.30 OCT image of metal lines through denser solution of micro-beads with aberration correction

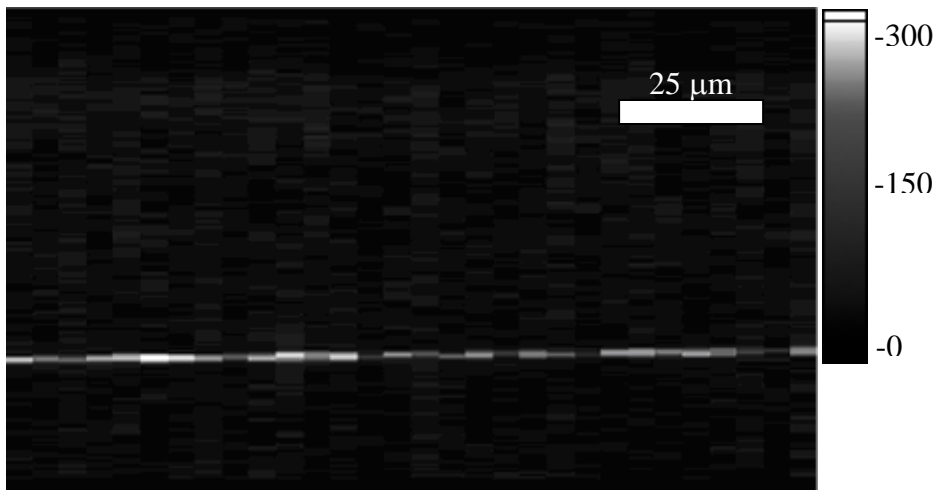


Figure 5.31 OCT image of metal lines through milk solution without AO

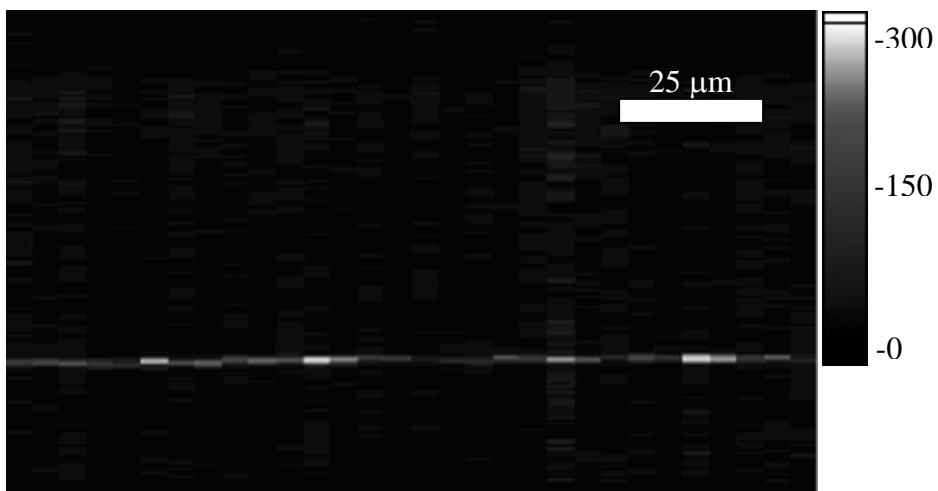


Figure 5.32 OCT image of metal lines through milk solution with AO

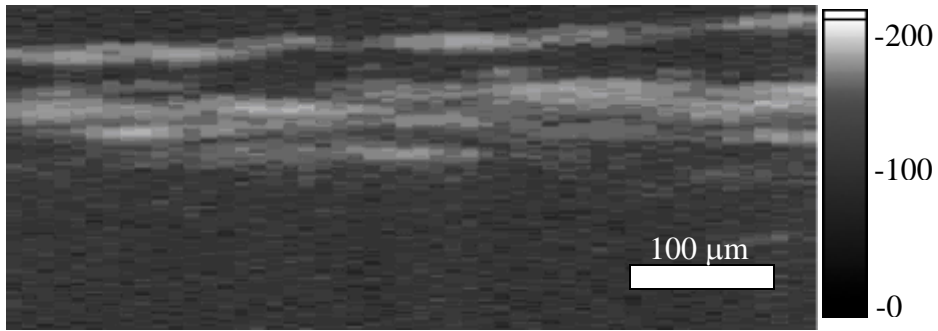


Figure 5.33 OCT image of an onion without adaptive optics

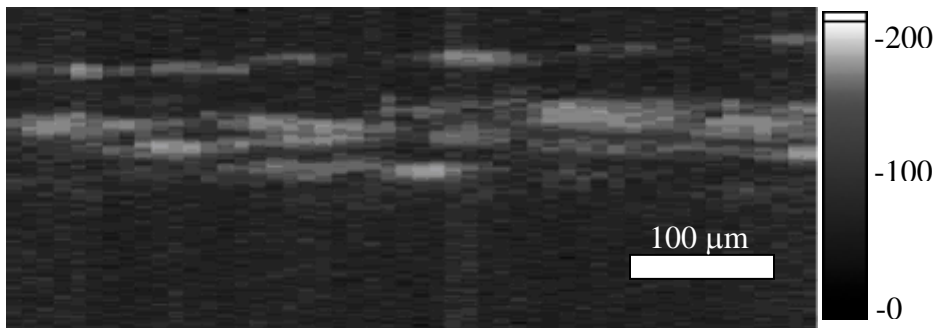


Figure 5.34 OCT image of an onion with aberration correction

The final target imaged was a piece of fresh onion. The aberration was corrected by applying the same compensating phase map used in previous experiment. Figure 5.33 presents the OCT image of onion without controlling of the adaptive optics whereas Figure 5.34 shows the OCT image of the same area with aberration correction. Differences between the two images is not as dramatic as Figure 5.29 and 5.30, but Figure 5.34 displays more detailed structural information of the onion in the second layer from the top of the image. Possible reasons for small differences in lateral resolution improvement may include 1) amount of scattering in real biological samples is different from the micro-bead solution case 2) that onion is not an excellent candidate to distinguish lateral structural information.

## 5.9. Conclusion

As an attempt to improve lateral resolution in OCT, adaptive optics has been integrated into an OCT system. The adaptive optics consists of a wavefront sensing device and corrector. Arbitrary aberration could be corrected by using Hamamatsu high-resolution, nonpixelized, optically addressed parallel-aligned nematic liquid crystal spatial light modulator (PAL-SLM), PPM X7550 series. Wavefront of the light entering entrance pupil of sample path was measured by using parallel OCT. This approach has a few advantages over conventional wavefront sensors including aberrometers and Shack-Hartmann wavefront sensors. A major benefit of using this method is simplicity and reduced cost. Because OCT is based on an interferometer, phase information can easily be obtained by analyzing recorded interferograms and does not require having additional optics or instruments. Another advantage is that the optical paths to detect phase maps are common with actual OCT imaging path. Therefore, no additional error due to different optics will be introduced.

In this study I have used a CCD camera to detect the phase information, which allowed rapid recording of two-dimensional phase maps. The CCD camera can be replaced with a single element photo-receiver to overcome the CCD camera's low signal to noise ratio. To achieve acquisition of phase maps using a single element photo-receiver, fast transverse and longitudinal scanners are required to construct a two-dimensional phase map. In this study the author used a longitudinal scanner based on a motorized



stage that permits relatively slow scanning speed compared to a galvanometer. More detailed discussion in this regard will be covered in Chapter 6.

Improvement of the beam diameter at the sample could be confirmed by imaging the beam profile with a CCD camera even though the profile couldn't indicate if the focus of the light was diffraction-limited. Careful calibration of the optics needs to be performed to approach the limit.

The dynamic range of the CCD camera used in this study was limited by the 8 bit A/D range, and also the CCD had poor signal to noise ratio, ~50 dB. For more accurate measurement of OCT image, a rastering scanning scheme was adapted by using a single element photo-receiver instead of the CCD camera, but still the CCD camera was used only to measure the phase map of the light. Purely refractive and scattering samples were tested to present the performance of the OCT with adaptive optics. 25  $\mu\text{m}$  separation of metal lines exposed to air could be become distinguishable after correcting aberration by the adaptive optics otherwise OCT image showed blurred line separation. A scattering sample was prepared with the metal lines obscured with a micro-bead solution or milk. In these cases the aberration could be successfully corrected by the adaptive optics, so the OCT image displayed clearer line separation than that without the adaptive optics. Finally onion tissue was imaged with the raster scanning OCT integrated with the adaptive optics, and the improvement of the lateral resolution could be observed in images with operation of the adaptive optics.

## 5.10. References

1. J. M. Schmitt, "Optical Coherence Tomography," IEEE Journal in quantum electronics **5**(4)(1999).
2. J. Porter, A. Guirao, I. G. Cox, and D. R. Williams, "Monochromatic aberrations of the human eye in a large population," Journal of the Optical Society of America a-Optics Image Science and Vision **18**(8), 1793-1803 (2001).
3. W. T. Welford, "Aberrations of Optical Systems," Hilger, Bristol, UK (1986).
4. W. J. Smith, "Modern Optical Engineering: The Design of Optical Systems," McGraw-Hill, New York (1990).
5. H. C. Howland and B. Howland, "Subjective Method for Measurement of Monochromatic Aberrations of Eye," Journal of the Optical Society of America **67**(11), 1508-1518 (1977).
6. R. J. Noll, "Zernike Polynomials and Atmospheric-Turbulence," Journal of the Optical Society of America **66**(3), 207-211 (1976).
7. J. Schwiegerling and J. E. Greivenkamp, "Using corneal height maps and polynomial decomposition to determine corneal aberrations," Optometry and Vision Science **74**(11), 906-916 (1997).
8. M. B. a. E. Wolf, "Principles of Optics," Cambridge **7th edition**(1999).
9. J. W. Hardy, "Active optics:a new technology for the control of light," Proc. IEEE **66**, 651-697 (1978).

10. R. K. Tyson, "Principles of Adaptive Optics," Academic press **2nd Edition**(1998).
11. J. Z. Liang and D. R. Williams, "Aberrations and retinal image quality of the normal human eye," Journal of the Optical Society of America a-Optics Image Science and Vision **14**(11), 2873-2883 (1997).
12. G. Robins, Reid, G.T., "Interferogram Anaysis Digital Fringe Pattern Measurement Techniques," 167-173 (1993).
13. H. Hofer, P. Artal, B. Singer, J. L. Aragon, and D. R. Williams, "Dynamics of the eye's wave aberration," Journal of the Optical Society of America a-Optics Image Science and Vision **18**(3), 497-506 (2001).
14. A. Roorda, F. Romero-Borja, W. J. Donnelly, H. Queener, T. J. Hebert, and M. C. W. Campbell, "Adaptive optics scanning laser ophthalmoscopy," Optics Express **10**(9), 405-412 (2002).
15. K. G. Larkin, D. J. Bone, and M. A. Oldfield, "Natural demodulation of two-dimensional fringe patterns. I. General background of the spiral phase quadrature transform," Journal of the Optical Society of America a-Optics Image Science and Vision **18**(8), 1862-1870 (2001).
16. K. Creath, "Phase-measurements interferometry techniques," Progress in Optics **26**, 349-393 (1988).

## Chapter 6 Future Directions and Conclusion

### 6.1. Summary

A detailed description of the parallel OCT with the CMOS smart array detector is given in Chapter 2. The CMOS smart array detector was calibrated and electrically optimized to be used in the parallel OCT. *Ex vivo* gold fish retina was imaged with the parallel OCT system at a frame rate of 1100 frames per second. *In vivo* hamster retina imaging was also performed approximately over 10  $\mu\text{m}$  of a beam spot.

A speckle reduction method using a partially coherent source in a Michelson interferometer in a parallel detecting OCT system was proposed and demonstrated in Chapter 3. A Gaussian-Schell model source was used to simulate the effect of speckle reduction using a partially coherent source. A multimode optical fiber was used to convert a spatially coherent source to partially coherent light. Results of simulations and experiments indicate that broadband light sources with reduced spatial coherence that provide a large number of photons per coherence volume may be utilized to reduce speckle in OCT interferograms.

A methodology to record spatial variation of refractive index of porcine renal artery using differential phase optical coherence tomography (DP-OCT) was described in Chapter 4. Two-dimensional *en face* dual-channel phase images were recorded over 150  $\mu\text{m} \times 200 \mu\text{m}$  region on a microscope slide and the images are reconstructed by plotting relative phase variation as the OCT beam is moved across the artery cross section.

Chapter 5 describes the implementation of OCT with adaptive optics. Importance of aberration correction in eyes in ophthalmic application is discussed. The correction requires measurement and modification of the wavefront of incident light. An straight forward approach was proposed and demonstrated to measure a two-dimensional phase map of the wavefront using parallel OCT. An arbitrary wave aberration was corrected using a HAMAMATSU high-resolution, non-pixelized, optically addressed parallel-aligned nematic liquid crystal spatial light modulator (PAL-SLM), PPM X7550 series. Improvement of the lateral resolution was demonstrated in reflective and scattering samples. Combination of OCT with adaptive optics may provide diffraction limited lateral and submicron axial resolutions in ophthalmic imaging.

## **6.2. Future Directions**

### **6.2.1. Parallel OCT with the CMOS Smart Array Detector**

Although implementing an analog circuit to process the OCT signal into a pixel, the current CMOS smart detector array has several disadvantages including a small number of pixels, small fill factor, low dynamic range, and electrical instability. The small fill factor is caused by the fact that the photo-diode at each pixel of the array detector covers only 10 % of whole pixel area and 90 % of fringe signal can not be detected. A method to improve the fill factor was proposed in the author's Ph.D. research proposal by using a micro-lens array that focuses incoming light to the photo diode at each pixel, but was not pursued further mainly due to high cost of custom-made micro-lens array. A standard micro-lens array that can be purchased from manufacturers at a cost of about \$1000 has

different dimension with the pixel. An additional telecentric lens was used to de-magnify the pixelized focal plane of the micro-lens array. Implementing a micro-lens array from the design stage may improve the next generation CMOS smart array detector.

Figure 6.1 suggests a parallel OCT system with fill-factor improved CMOS smart array detector. In this system by using a fiber-based phase modulator, no moving scanner is required. As Figure 6.1 shows a light source is connected to a Y-type waveguide phase modulator that has one input and two output channels. Both channels can be modulated by separate voltage drivers, but here the purpose is to separate two channels, but modulate only one channel. However the other channel that is not modulated has the same material with the modulated channel. Therefore, any chromatic dispersion will be exactly compensated by this un-modulated channel because both channels contain the same material and length.

Another feature of the Y-type phase modulator is that the waveguide only propagates only one polarization state and will work as a polarizer and both output channels have the same polarization state. This polarization state will be maintained by a polarization maintaining optical fiber (PM fiber). Each PM fiber will be connected to a beam collimator, and both collimators will launch linearly polarized light groups toward polarization sensitive beam splitter (PBS). One collimator will be mechanically rotated  $90^\circ$  so one input light to PBS will be vertically linearly polarized whereas the other input light will be horizontally linearly polarized. The PBS will transmit vertically linearly polarized light but reflect horizontally linearly polarized light. Therefore, both incoming

light groups will enter a read-out interferometer without losing any significant light by the beam splitter.

The separation ( $L_1$ ) between beam collimator 1 to PBS and beam collimator 2 to PBS is outside the coherence length of the system. Therefore, there will be no interference at PBS where both light groups join.

When two light groups separated by  $L_1$  enter the read-out interferometer they will enter another PBS by which the two light groups will be separate. In this case the PBS will transmit one polarization state light going to a sample but the other will be reflected to a mirror M3. The separation between the PBS to M3 and the PBS to the sample will be  $-L_1$ .

In each arm of the interferometer a quarter wave plate is placed, so after double passage the polarization state will be rotated by  $90^\circ$ . If horizontally polarized light is incident in then vertically polarized light will come out. When both light groups enter the PBS, both will be directed to the detection arm where the array detector is located. No interference will be observed between two light groups because both have orthogonal polarizations. Finally a polarizer in front of the array detector forms fringe signal. This will be done by rotating the polarizer  $45^\circ$  so each light component in both groups that can transmit through the polarizer and interfere. In front of the array detector a micro-lens array will be located to focus the incoming beam into each photo diode.

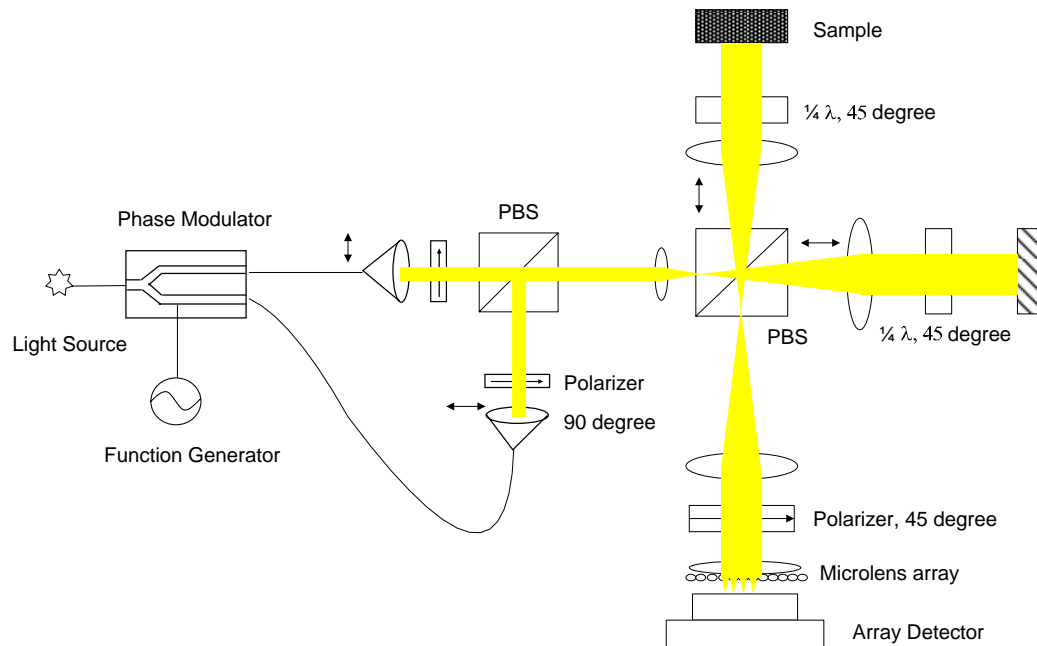


Figure 6.1 Fiber based parallel detecting OCT with CMOS smart array detector

As demonstrated in Chapter 3, speckle can be reduced in this proposed system by using a partially spatial light source that can be easily implemented with a multimode optical fiber.

### 6.2.2. OCT with Adaptive Optics

In Chapter 5 a parallel OCT system with adaptive optics was developed and demonstrated to improve lateral resolution in a model eye; however the system was not applied on real biological eye because of the limitation in dynamic range of the CCD camera (8 bit). To acquire reasonable image quality at least 10 bit resolution is required. A high speed and high resolution CCD camera is still extremely expensive (over \$40000 for 10 bit resolution and 10000 frames per second).



One way to increase the dynamic range is to use a raster scanning approach with a single photo-receiver. It requires two additional scanners to acquire three dimensional images. The system demonstrated in this dissertation has only one lateral scanner mounted on a motorized stage, which provides a slow scanning speed. To achieve a real time OCT type retinal scanner, galvanometers should be used as scanners. Figure 6.2 illustrates the schematic diagram of the sample optics of OCT with adaptive optics and two galvanometer scanners. Light launches into the sample optics through optical fiber tip [FT] that is conjugate with a mirror [M1] and also with retinal layer of the eye [ $r$ ]. The pupil plane (noted as  $p$ ) has a conjugate plane at the vertical scanner [VS] and horizontal scanner [HS]. Moreover the plane should be conjugate with the plane of the adaptive optics [AO] that modifies the wavefront of light going into the pupil. The CCD camera and lenslet array consist a Shack-Hartmann wavefront sensor, and should be conjugate with the retinal and pupil planes respectively. There is a need to investigate which method has better performance and accuracy in measuring wavefronts between the Shack-Hartmann wavefront sensor and the phase extraction method using interferograms which was proposed in this dissertation.

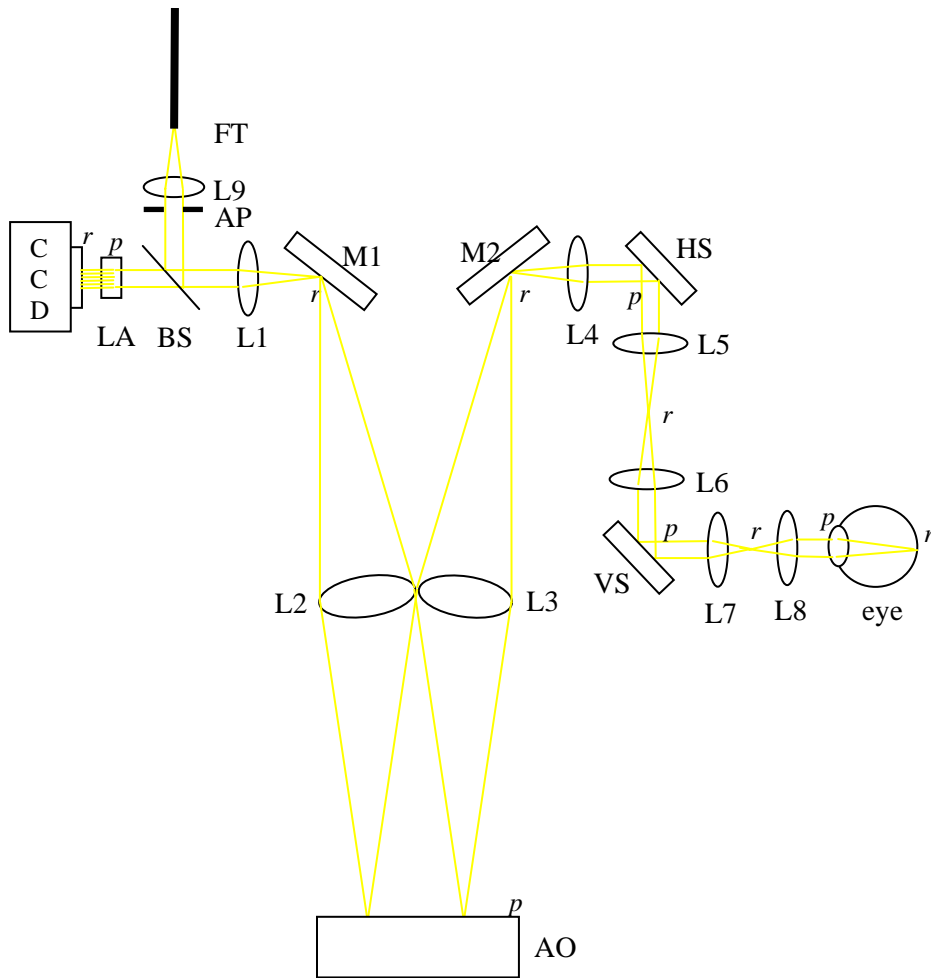


Figure 6.2 Schematic diagram of the sample arm adaptive optics with two galvanometer scanners. Lenses are labeled L# and mirrors M#. Retinal and pupil conjugate planes are labeled r and p. FT: optical fiber tip of the sample arm. AP: Aperture, BS: beam splitter, LA: lenslet array, CCD: digital charge coupled device camera

### 6.3. Conclusion of the Dissertation

Various topics are investigated in this dissertation to improve parallel OCT. First, as an attempt to enhance acquisition speed, the CMOS smart array detector is adapted in parallel OCT instead of a CCD camera. 1100 frames per second of frame rate is achieved on *ex vivo* imaging a gold fish retina and on *in vivo* imaging a hamster retina. Axial structural boundaries in the hamster retinal image can be identified, but lateral structural information may not be clarified mainly due to small number of pixels of the detector.

A speckle reduction method using a partially coherent source in a Michelson interferometer in a parallel detecting OCT system is proposed and demonstrated. Speckle noise in interferograms recorded using a partially coherent source is substantially reduced compared to the fully coherent case. No degradation in SNR is observed, and no measurable mode cross-coupling is observed in the multimode fiber. A partially coherent source is also preferable for *en face* imaging not only for reducing speckle but also for eliminating Airy rings in the image caused by the small field diameter of most single mode fibers. Results of the simulations and experiments indicate that broadband light sources with reduced spatial coherence that provide a large number of photons per coherence volume may be utilized to reduce speckle in OCT interferograms.

In order to investigate the origin of the speckle, DP-OCT is used to image spatial refractive index variation in porcine arteries. DP-OCT has the capability of imaging quantitative optical phase retardation of tissue sections. The relative phase retardation image of porcine renal artery is taken after the cross section of the lumen is processed for

histology. The retardation image can be directly related to the refractive index of the tissue with knowledge of the refractive index of the mounting media and tissue thickness.

To improve lateral resolution in OCT, adaptive optics is integrated into an OCT system. The adaptive optics consists of wavefront sensor and wavefront corrector. Arbitrary aberration can be corrected by using Hamamatsu high-resolution, nonpixelized, optically addressed parallel-aligned nematic liquid crystal spatial light modulator (PAL-SLM), PPM X7550 series. Wavefront of the light entering entrance pupil of sample path is measured by using parallel OCT. This approach has a few advantages over conventional wavefront sensors including aberrometers and Shack-Hartmann wavefront sensors. Major benefit of using this method is low cost. Because OCT is based on an interferometer, phase information can be easily obtainable by analyzing the interferograms. It doesn't require having additional optics or instruments. Another advantage is that the optical path to detect phase maps shares the same path with actual OCT imaging path. Therefore, no additional error due to different optics will be introduced.

Improvement of the beam diameter at the sample is confirmed by imaging the beam profile with a CCD camera even though the profile can not indicate if the focus of the light is diffraction-limited. For more accurate measurement of an OCT image, a raster scanning scheme is adapted by using a single element photo-receiver instead of the CCD camera, but still the CCD camera is used only to measure the phase map of the light. Purely reflective and scattering samples are tested to present the performance of the OCT with adaptive optics. 25  $\mu\text{m}$  separation of metal lines exposed to air becomes

distinguishable after correcting aberration by the adaptive optics otherwise OCT image shows blurred line separation. A scattering sample is prepared with the sample metal lines covered with diluted microbead solution or milk. In these cases the aberration is successfully corrected by adaptive optics, so the OCT image displays clearer line separation than that without the adaptive optics. Finally onion sample are imaged with the raster scanning OCT integrated with the adaptive optics, and the improvement of the lateral resolution is observed in images corrected with adaptive optics.

## Bibliography

1. J. M. Schmitt, "Optical Coherence Tomography," IEEE Journal in quantum electronics **5**(4)(1999).
2. J. Porter, A. Guirao, I. G. Cox, and D. R. Williams, "Monochromatic aberrations of the human eye in a large population," Journal of the Optical Society of America a-Optics Image Science and Vision **18**(8), 1793-1803 (2001).
3. W. T. Welford, "Aberrations of Optical Systems," Hilger, Bristol, UK (1986).
4. W. J. Smith, "Modern Optical Engineering: The Design of Optical Systems," McGraw-Hill, New York (1990).
5. H. C. Howland and B. Howland, "Subjective Method for Measurement of Monochromatic Aberrations of Eye," Journal of the Optical Society of America **67**(11), 1508-1518 (1977).
6. R. J. Noll, "Zernike Polynomials and Atmospheric-Turbulence," Journal of the Optical Society of America **66**(3), 207-211 (1976).
7. J. Schwiegerling and J. E. Greivenkamp, "Using corneal height maps and polynomial decomposition to determine corneal aberrations," Optometry and Vision Science **74**(11), 906-916 (1997).
8. M. B. a. E. Wolf, "Principles of Optics," Cambridge **7th edition**(1999).
9. J. W. Hardy, "Active optics:a new technology for the control of light," Proc. IEEE **66**, 651-697 (1978).

10. R. K. Tyson, "Principles of Adaptive Optics," Academic press **2nd Edition**(1998).
11. J. Z. Liang and D. R. Williams, "Aberrations and retinal image quality of the normal human eye," Journal of the Optical Society of America a-Optics Image Science and Vision **14**(11), 2873-2883 (1997).
12. G. Robins, Reid, G.T., "Interferogram Analysis Digital Fringe Pattern Measurement Techniques," 167-173 (1993).
13. H. Hofer, P. Artal, B. Singer, J. L. Aragon, and D. R. Williams, "Dynamics of the eye's wave aberration," Journal of the Optical Society of America a-Optics Image Science and Vision **18**(3), 497-506 (2001).
14. A. Roorda, F. Romero-Borja, W. J. Donnelly, H. Queener, T. J. Hebert, and M. C. W. Campbell, "Adaptive optics scanning laser ophthalmoscopy," Optics Express **10**(9), 405-412 (2002).
15. K. G. Larkin, D. J. Bone, and M. A. Oldfield, "Natural demodulation of two-dimensional fringe patterns. I. General background of the spiral phase quadrature transform," Journal of the Optical Society of America a-Optics Image Science and Vision **18**(8), 1862-1870 (2001).
16. K. Creath, "Phase-measurements interferometry techniques," Progress in Optics **26**, 349-393 (1988).

## VITA

JeeHyun Kim was born in TaeJean, South Korea on July 10, 1972, the son of KiWan Kim, PhD and YongBook Yoon. After completing his work at Sim-In High School, Taegu,, South Korea in 1991, he entered KyungPook National University in Taegu, South Korea. He received the Bachelor of Science degree from KyungPook National University in February, 1995. During the following 3 years he worked at Daewoo Precision Industries Ltd. as a research engineer. In September 1998, he entered the Graduate School at The University of Texas at Austin and received the Master degree under Dr. Jonathan Valvano's supervision. The master thesis topic was the measurement of the thermal properties of heart atrium using the computerized acquisition system. He was advised by Dr. Thomas Milner and Dr. Grady Rylander III for Ph.D. research, and specialized in various optical coherence tomography techniques.

Permanent Address : 25 Via Lucca #J232

Irvine, CA 92612

This thesis was typed by the author.